NASA/TM–20250001494

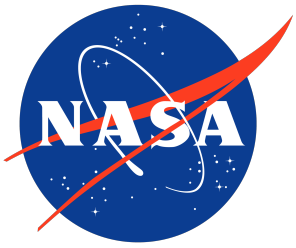

Computational Analysis of the X-57 Maxwell Airplane, the Cruise Configuration with Various Cruise Power Settings (Preliminary Fuselage)

Karen A. Deere and Jeffrey K. Viken
NASA Langley Research Center, Hampton, Virginia

Michael R. Wiese and Norma L. Farr
Craig Technologies, Hampton, Virginia

February 2025

NASA STI Program Report Series

Since its founding, NASA has been dedicated to the advancement of aeronautics and space science. The NASA scientific and technical information (STI) program plays a key part in helping NASA maintain this important role.

The NASA STI Program operates under the auspices of the Agency Chief Information Officer. It collects, organizes, provides for archiving, and disseminates NASA's STI. The NASA STI Program provides access to the NTRS Registered and its public interface, the NASA Technical Report Server, thus providing one of the largest collections of aeronautical and space science STI in the world. Results are published in both non-NASA channels and by NASA in the NASA STI Report Series, which includes the following report types:

- TECHNICAL PUBLICATION. Reports of completed research or a major significant phase of research that present the results of NASA programs and include extensive data or theoretical analysis. Includes compilations of significant scientific and technical data and information deemed to be of continuing reference value. NASA counterpart of peer-reviewed formal professional papers, but having less stringent limitations on manuscript length and extent of graphic presentations.
- TECHNICAL MEMORANDUM. Scientific and technical findings that are preliminary or of specialized interest, e.g., quick release reports, working papers, and bibliographies that contain minimal annotation. Does not contain extensive analysis.
- CONTRACTOR REPORT. Scientific and technical findings by NASA-sponsored contractors and grantees.
- CONFERENCE PUBLICATION. Collected papers from scientific and technical conferences, symposia, seminars, or other meetings sponsored or co-sponsored by NASA.
- SPECIAL PUBLICATION. Scientific, technical, or historical information from NASA programs, projects, and missions, often concerned with subjects having substantial public interest.
- TECHNICAL TRANSLATION. English-language translations of foreign scientific and technical material pertinent to NASA's mission.

Specialized services also include organizing and publishing research results, distributing specialized research announcements and feeds, providing information desk and personal search support, and enabling data exchange services.

For more information about the NASA STI Program, see the following:

- Access the NASA STI program home page at `http://www.sti.nasa.gov`
- Help desk contact information: `https://www.sti.nasa.gov/sti-contact-form/` and select the "General" help request type.

NASA/TM–20250001494

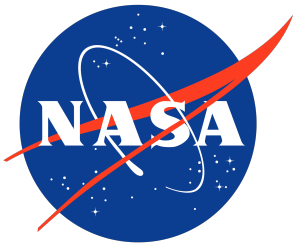

Computational Analysis of the X-57 Maxwell Airplane, the Cruise Configuration with Various Cruise Power Settings (Preliminary Fuselage)

Karen A. Deere and Jeffrey K. Viken
NASA Langley Research Center, Hampton, Virginia

Michael R. Wiese and Norma L. Farr
Craig Technologies, Hampton, Virginia

National Aeronautics and
Space Administration

Langley Research Center
Hampton, Virginia 23681-2199

February 2025

Acknowledgments

This work was done for the X-57 aerodynamic database development in support of the Flight Demonstrations and Capabilities Project in the Integrated Aviation Systems Program. The computations were conducted on the supercomputers supplied by the NASA High-End Computing (HEC) Program through the NASA Advanced Supercomputing (NAS) Division at the NASA Ames Research Center (ARC). This work would not have been possible without these critical HEC resources and NAS support staff.

The authors would like to formally thank Mohagna J. Pandya and Thomas J. Wignall for their support in establishing the propulsion boundary condition for Goldstein thrust and torque distributions that were necessary to appropriately model the thrust from the X-57 cruise propellers, and for making necessary code updates to support the authors during the X-57 project.

The authors appreciate the contributions of the X-57 CFD team from NASA ARC and NASA Armstrong Flight Research Center (AFRC) for their computational data for comparisons with data from the NASA Langley Research Center (LaRC). The three NASA centers that comprise the X-57 CFD team provided thousands of computational data points for the X-57 aerodynamic database. The Launch Ascent and Vehicle Aerodynamics (LAVA) team from ARC included Jared Duensing, Daniel Maldonado, James Jensen, and Jeffrey Housman. The AFRC team included Seung Yoo, Michael Frederick and Trong Bui. The LaRC team included Karen Deere, Jeffrey Viken, Sally Viken, Melissa Carter, Norma Farr and Michael Wiese.

Available from:

NASA STI Program / Mail Stop 150
NASA Langley Research Center
Hampton, VA 23681-2199

Abstract

The X-57 Maxwell was an all-electric airplane with a distributed electric propulsion system used for a high-lift system at takeoff and landing conditions. The focus of this paper is the cruise configuration with the wingtip propellers operating and the distributed electric propulsion propellers stowed. The computational fluid dynamics flow solver, USM3D, was used to investigate the performance of the X-57 Maxwell at flight Reynolds numbers from 1.4 million to 2.8 million, based on mean aerodynamic chord. Numerical solutions were computed at 2° angle of attack for Mach numbers from 0.1 to 0.3 (64.3 KTAS to 141.6 KTAS), at altitudes of 2500 feet, 8000 feet, and 15000 feet, and cruise power at 1150 RPM, 2000 RPM, and 2250 RPM, and no high-lift blowing. Data were also computed at angles of attack of 8°, 12°, and 16° for a Mach number of 0.1355 (85.7 KTAS), at an altitude of 2500 feet for no high-lift blowing and cruise power at 2250 RPM. An actuator disk was used to model the cruise propellers.

The X-57 Maxwell wingtip propellers opposing the wingtip vortex reduced the induced drag penalty for angles of attack less than 16°. Increasing thrust reduced drag and the greatest drag reduction occurred at the lowest airspeed. The cruise thrust increased lift for all angles of attack less than 16°. The increased lift from cruise power was larger at 85.7 KTAS, than at an airspeed of 128.2 KTAS. The effect of cruise thrust on pitching moment was a slight increase in nose-down pitching moment coefficient with increasing thrust coefficient for both airspeeds and angles of attack less than 16°. There was little to no effect of cruise thrust on yawing moment coefficient for angles of attack less than 16°. The effect of cruise thrust on rolling moment was larger at 85.7 KTAS than at 128.2 KTAS. The change in rolling moment between powered and unpowered conditions was significantly larger at 85.7 KTAS, than at 128.2 KTAS. These data were important to understand the effect of differential cruise thrust on rolling moment to add the effects in the X-57 Maxwell flight simulator. The effect of cruise power on rolling moment predicted from three computational fluid dynamics codes, from three NASA centers, compared very well for low angles of attack of 0° and 2°, and moderately well for angles of attack of 8° and 12°. These data comparisons were important for gaining confidence in the computational data when no experimental data were available prior to flight testing.

Contents

List of Figures

List of Tables

Nomenclature

α	=	angle of attack, degrees
a	=	successive ratio growth rate for the viscous layers
a_∞	=	freestream speed of sound, feet/second
b	=	growth rate of the successive ratio
b_{ref}	=	reference span, inches
β	=	angle of sideslip, degrees
$cfl1$	=	numerical field in USM3D input file representing the minimum CFL number
$cfl2$	=	numerical field in USM3D input file representing the maximum CFL number
c_{ref}	=	reference chord, mean aerodynamic chord, 25.56 inches
C_D	=	drag coefficient = drag force / (q_∞ S_{ref})
C_f	=	magnitude of the skin friction coefficient
C_l	=	rolling moment coefficient = rolling moment / (q_∞ S_{ref} b_{ref})
C_L	=	lift coefficient = lift force / (q_∞ S_{ref})
$C_{L,max}$	=	maximum lift coefficient = maximum lift force / (q_∞ S_{ref})
C_m	=	pitching moment coefficient = pitching moment / (q_∞ S_{ref} c_{ref})
$C_{m,X}$	=	body-axis moment coefficient around the x axis
$C_{m,Y}$	=	body-axis moment coefficient around the y axis, equivalent to C_m
$C_{m,Z}$	=	body-axis moment coefficient around the z axis
C_n	=	yawing moment coefficient = yawing moment / (q_∞ S_{ref} b_{ref})
C_p	=	pressure coefficient = (p – P_∞) / (q_∞)
C_T	=	thrust coefficient = T / (ρ_∞*(RPM/60)^2*D^4)
$C_{T,usm}$	=	normalized thrust coefficient for USM3D = $4/\pi^3$*C_T
C_Q	=	torque coefficient = Q / (ρ_∞*(RPM/60)^2*D^5)
$C_{Q,usm}$	=	normalized torque coefficient for USM3D = $8/\pi^3$*C_Q
C_Y	=	side force coefficient = side force / (q_∞ S_{ref})
δ_1	=	height of the first node off the surface, inches
$delta_t$	=	nondimensional time step for time-accurate computations in USM3D, Equation 3
$D_{t,char}$	=	distance a signal travels in one time step, Equation 2, inch/step
γ	=	gamma, specific heat ratio
J	=	propeller advance ratio = V_∞ / ((RPM/60)*D)
J_{usm}	=	normalized propeller advance ratio for USM3D = J/π
$log(r/r0)$	=	log scale L2-norm of the mean flow residue, normalized by the initial value
$log(tnu/tnu0)$	=	log scale L2-norm of the turbulent residue, normalized by the initial value
L/D	=	lift to drag ratio
L_{char}	=	characteristic reference length, inches
M	=	freestream Mach number
N	=	number of time steps
ϕ	=	roll angle, degrees
P	=	pressure, generic expression, psf
P_∞	=	freestream static pressure, psf
q_∞	=	freestream dynamic pressure = ρ V^2 / 2, psf
Q	=	torque, lbf-ft
r	=	radial location, inches
R	=	radius, inches

ρ_∞	=	freestream density, slugs/feet^3
Re	=	unit Reynolds number, per foot
Re_c	=	Reynolds number based on reference chord
$ReUe$	=	freestream Reynolds number per unit length, specified in millions
RA	=	grid growth rate A
RB	=	grid growth rate B
S_{ref}	=	reference area, 66.67 feet^2
s	=	primary length scale at the source center
S	=	stretched length scale at the source center
T	=	thrust, lbf
T_∞	=	freestream temperature, °R
T_{max}	=	maximum thrust along the propeller radius, lbf
u	=	dimensional velocity, feet/second
U	=	nondimensional velocity used in USM3D = u / a_∞
V_∞	=	freestream velocity, feet/second
V_o	=	velocity vector
x, y, z	=	Cartesian coordinates, inches
xmc	=	moment center in X-direction (streamwise direction), inches
ymc	=	moment center in Y-direction (spanwise direction), inches
y^+_{cell}	=	nondimensional height of the first cell in the boundary layer
y^+_{node}	=	nondimensional height of the first node in the boundary layer
zmc	=	moment center in Z-direction (normal direction), inches

Acronyms and Abbreviations

AFRC	Armstrong Flight Research Center
ARC	Ames Research Center
AoA	angle of attack, degrees
CAD	computer aided design
CFD	computational fluid dynamics
CTU	convective time unit
CFL	Courant–Friedrichs–Lewy [number]
DEP	distributed electric propulsion
GEOLAB	GEOmetry LABoratory
KCAS	knots calibrated airspeed
KEAS	knots equivalent airspeed
KTAS	knots true airspeed
LaRC	Langley Research Center
LES	Large Eddy Simulation
LGC	landing gear cover
NASA	National Aeronautics and Space Administration
NL	the maximum number of layers in the boundary layer
NPS	nacelles, pylons, strakes
psf	pounds per square feet
POR	percent over range convergence equation
QCR	quadratic constitutive relation
RANS	Reynolds-averaged Navier-Stokes [equations]

RC	rotation curvature [correction]
RPM	revolutions per minute
SA	Spalart-Allmaras [turbulence model]
SST	Shear Stress Transport [turbulence model]
TN	wingtip nacelle
TetrUSS	NASA Tetrahedral Unstructured Software System
VG	vortex generator

1 Introduction

The X-57 Maxwell was an all-electric airplane with a distributed electric propulsion (DEP) system to increase lift at takeoff and landing conditions [1–3]. The X-57 airplane was designed to cruise efficiently at 150 knots true airspeed (KTAS), which is a Mach number (M) of $M = 0.233$ at an altitude of 8,000 feet. A concept image of the X-57 Maxwell aircraft is shown in Figure 1. The DEP system included twelve high-lift, electrically-powered propellers positioned along the wing leading edge to increase the velocity over the wing, and thus, reduce the upper-surface pressure, for a boost of lift. The high-lift propellers folded conformally onto the high-lift nacelles at cruise conditions to minimize drag when the DEP high-lift system was not needed. The electrically-powered cruise propellers are located on the wingtip nacelles. Some previous computational fluid dynamics (CFD) results on earlier variations of the airplane have been published [4–10].

The initial objective of the X-57 Maxwell project was to demonstrate that emission-free electric motors could be integrated with the aircraft configuration to increase overall aircraft efficiency. The goal was to demonstrate that the small cruise efficient wing, integrated with the DEP system, could achieve the flight objectives with at least 3x lower energy use compared to the baseline Tecnam P2006T aircraft [1]. The lower energy consumption resulted from a combination of improved aerodynamic efficiency from reducing the wing area, an improvement in motor efficiency, and an improvement in propulsion efficiency from the wingtip propellers operating opposite to the wingtip vortex to reduce induced drag. To meet the cruise performance goal of $M = 0.233$ and at an altitude of 8000 feet, the X-57 had a cruise lift coefficient ($C_{L,cruise}$) of 0.7516 and needed to have a cruise drag coefficient of 0.05423 or less.

In the X-57 Maxwell project, the development and analysis of the airplane was divided into four phase modifications (Mods), with each Mod focused on a different aircraft configuration. The Mod I aircraft configuration was the original Tecnam P2006T aircraft and is shown in Figure 2. The P2006T aircraft had a wing area of 158.8 feet^2, a wing loading of 17 pounds per square feet (psf), a wing span of 37.4 feet, a root chord of 4.57 feet (54.84 inches), and a tip chord of 2.9 feet (34.8 inches). The Mod II aircraft configuration was an electric version of the P2006T, with electric motors and X-57 cruise propellers replacing the original combustion engines and propellers on the P2006T aircraft. A front view of the Mod II configuration with the electric motors running is shown in Figure 3. The Mod II aircraft configuration

was planned to test engine safety and service during taxi tests, and then flight test the electric motors, the batteries, and the instrumentation before they would have been flown in the Mod III configuration. For the Mod III aircraft configuration, the P2006T wing would have been replaced with the X-57 wing, and the Mod II electric cruise motors and propellers would have been moved out to the wingtip nacelles, see Figure 4. The X-57 Maxwell Mod III wing had a reduced wing area of 66.7 feet^2, a higher wing loading of 45 psf, a shorter wing span of 31.6 feet (379.47 inches), and a shorter mean aerodynamic chord of 2.13 feet (25.56 inches), compared to the original Tecnam P2006T airplane. The Mod IV aircraft configuration had the 12 high-lift motors and propellers integrated into the X-57 Mod III wing for the final, all-electric X-57 Maxwell aircraft, see Figure 5. The high-lift propellers would have only been operational at takeoff and landing conditions, to produce the extra lift needed at low airspeeds with the smaller wing.

The primary driver of reduced wing area for the X-57 Mod III was reduced drag and increased efficiency. The smaller wing area reduced the total wetted area and the skin friction drag. The wing aspect ratio was increased from 8.8 to 15.0 for the X-57 to minimize the induced drag penalty of the increased gross weight. The minimum wing area was determined based upon the limits of the powered high-lift augmentation, the wing structural stiffness, and the wing internal volume.

The X-57 Maxwell airplane had an increased gross weight and had only 42% of the wing area of the original Tecnam P2006T wing. The increased gross weight was due to the battery weight in the X-57 Maxwell airplane. The weight of the batteries and the controller was 858 lbs. The total installed electrical power system weight was 1,071 lbs with the addition of the electric motors and controllers. This replaced the weight of the Tecnam Rotax engines of 305 lbs and 53 gallons of fuel, a total weight of 623 lbs.

The X-57 Maxwell would experience significantly smaller g-loadings in gusts compared to the Tecnam P2006T airplane. The g-loading in gusts is caused by an instant change in angle of attack. Airplanes that fly at cruise with a higher lift coefficient will experience a smaller lift coefficient increase for a given delta angle of attack than those that cruise at a smaller lift coefficient. For a given gross weight, the change in cruise coefficient is inversely proportional to the change in wing area (or wing loading). The cruise coefficient for the X-57 Maxwell was 0.75 compared to the Tecnam P2006T that has a cruise coefficient of 0.28, a factor of 2.7. The wing loading of the X-57 Maxwell was 45 psf and the Tecnam P2006T has a wing loading of 17 psf. The increase in g-loading for the Tecnam P2006T is a factor of 2.0 times the increase in g-loading for the X-57 Maxwell. For example, experiencing a 25.0 feet/sec gust the Tecnam P2006T will experience a g-loading of 2.4, while the X-57 Maxwell would experience a g-loading of 1.7.

The directional stability on airplanes with tip-mounted propellers can be affected by the longitudinal location of the propeller plane with respect to the center of gravity (CG). For airplanes with the propeller plane behind the CG, the tip-mounted propellers can be directionally stabilizing [11]. However, the X-57 tip-mounted propellers are ahead of the CG, and therefore, may reduce the directional stability. Thus, the directional stability of the X-57 airplane would need to be evaluated in flight tests.

Since there were no reliable experimental performance data for the X-57 airplane, the CFD results from three NASA centers were used to develop an aerodynamic database and establish uncertainty bounds for the force and moment coefficients for the X-57 Maxwell. The X-57 CFD team at LaRC used the USM3D code [12, 13] developed at Langley, and the Kestrel code [14, 15] developed by the Department of Defense (DoD) Computational Research and Engineering Acquisition Tools and Environment (CREATE-AV) group. The X-57 CFD team at the NASA Armstrong Flight Research Center (AFRC) used the commercially developed STAR-CCM+ code [16]. The X-57 CFD team at the NASA Ames Research Center (ARC) used the ARC developed Launch Ascent and Vehicle Aerodynamics (LAVA) code [17]. Some X-57 CFD team results from STAR-CCM+ and from LAVA have been published in References [18–20]. The fuselage geometry at the wing root for the configuration discussed in this paper is slightly different than the fuselage used with LAVA and STAR-CCM+. The configurations herein used the OpenVSP analytic fuselage geometry (preliminary fuselage), while a wind-tunnel model fuselage geometry was scaled up to full size for the LAVA and STAR-CCM+ solutions. The configurations with the preliminary fuselage and with the wind-tunnel model fuselage compare well except at the junction of the fuselage and wing-root where the smaller X-57 wing replaced the larger P2006T wing and the intersection geometries were developed differently. Additionally, the results from LAVA and STAR-CCM+ were typically computed with a local time stepping or steady-state Reynolds-averaged Navier-Stokes (RANS) approach, while the current solutions were computed with a global time stepping or time-accurate RANS approach. A time-accurate RANS approach was believed to be more appropriate for high-lift configurations near stall and for configurations with flow separation, as was expected for the X-57 Maxwell airplane. However, a hybrid Reynolds-averaged Navier-Stokes Large Eddy Simulation (hybrid RANS-LES) approach may be required to more accurately predict the maximum lift coefficient ($C_{L,max}$) and stall.

This is the third paper in a series of NASA technical memorandum papers from the NASA Langley Research Center (LaRC) documenting the computational results for the X-57 Maxwell airplane. The first paper documented the unblown and unpowered performance [21]. The second paper documented the Mod IV configuration with a landing flap deflection (δ_f) of 30° with high-lift blowing (HLB), and with aileron deflections [22]. This third paper records results for the X-57 at cruise power without high-lift blowing. The fourth paper will present the effects of high-lift power and flap deflection for the Mod IV configuration. The X-57 documentation catalog will eventually include two sets of papers. The first set will contain four papers documenting the results for the X-57 with the preliminary fuselage that was available the first three years of the project. The second set will contain papers for the X-57 flight fuselage and fairing; showing the effects of the flight fuselage as compared to the preliminary fuselage, the motor-out effects with and without aileron deflections, and the effects of the updated takeoff flap setting of $\delta_f = 20°$, on the aerodynamic coefficients.

The purpose of this paper is to document the performance of the cruise configuration with the wingtip propellers operating and the distributed electric propulsion propellers stowed. The computational fluid dynamics (CFD) flow solver, USM3D,

was used to predict the cruise performance at flight Reynolds numbers from 1.4 million to 2.8 million, based on mean aerodynamic chord. Numerical solutions were computed at an angle of attack of $\alpha = 2°$ for Mach numbers (M) from $M = 0.1$ to $M = 0.3$ (64.3 KTAS to 141.6 KTAS), at altitudes of 2500 feet, 8000 feet, and 15000 feet, and cruise power at 1150, 2000, and 2250 revolutions per minute (RPM), and no high-lift blowing. Data were also computed at angles of attack of 8°, 12°, and 16° for $M = 0.1355$ (85.7 KTAS), at an altitude of 2500 feet for no high-lift blowing and cruise power at 2250 RPM. Additionally, solutions were computed for the cruise configuration at unpowered conditions such that coefficient deltas could be computed between the power-on and power-off solutions. An actuator disk was used to model the cruise propellers. This paper does not include results for the high-lift blown wing with the DEP system operational.

Figure 1. Concept image of the X-57 Maxwell Airplane [Source: NASA / Advanced Concepts Lab].

Figure 2. Mod I, the Tecnam P2006T Airplane [Source: NASA].

Figure 3. Mod II, the Tecnam P2006T Airplane with electric cruise motors [Source: NASA AFRC TV / Steve Parcel].

Figure 4. Concept image of Mod III, the X-57 Maxwell Airplane with the cruise propellers operating and the high-lift propellers stowed [Source: NASA / Advanced Concepts Lab].

Figure 5. Concept image of Mod IV, the X-57 Maxwell Airplane with the cruise propellers and the high-lift propellers operating [Source: NASA / Advanced Concepts Lab].

2 Methods Description

This section describes the details for generating the computational data in this report. The majority of the data was generated with the USM3D CFD flow solver [12, 13] developed at NASA Langley Research Center (LaRC) as part of the Tetrahedral Software System (TetrUSS). Additionally, some test cases were also computed with the CREATE-AV Kestrel software developed by the Department of Defense [14, 15].

2.1 Computational Flow Solver

The TetrUSS flow solver USM3D is a tetrahedral cell-centered, finite volume Euler and Reynolds-averaged Navier-Stokes (RANS) method. The USM3D version used for this work was usm3d.cvs20160902+rotorextensions+SADDES+MachBC1002-Goldstein. The USM3D code has a variety of options for solving the flow equations and several turbulence models for closure of the RANS equations [13]. Fully turbulent predictions were computed with USM3D using the Spalart-Allmaras (SA) one-equation turbulence model [23] with the quadratic constitutive relation (QCR) [24]. The QCR2000 model is implemented in USM3D and is referred to as QCR within this paper. The SA model was chosen because the data from the SA model on a generic high-lift configuration were in better agreement with wind tunnel data than the shear stress transport (SST) turbulence model [25], although both models underpredicted upper surface pressures with less suction near the wingtip than wind tunnel data [26]. The SA-QCR2000 model has been shown to predict the presence of complex flow features arising from turbulent stresses with greater accuracy when compared to the baseline SA model [27].

This study used the implicit Gauss-Seidel scheme and the Roe flux difference-splitting scheme. The code was run in first-order spatial accuracy until the residual dropped two orders of magnitude. Then the code automatically switched to generate second order spatially accurate solutions.

2.2 Freestream Conditions

The freestream conditions studied in this paper are listed in Table 1 with velocity listed in units of knots true airspeed (KTAS). The freestream flow conditions specified in the USM3D code input file were Mach number (M), unit Reynolds specified in millions (ReUe), and freestream temperature (T_∞) in degrees Rankine (°R).

Table 1. Freestream Conditions.

Velocity KTAS	M	Altitude feet	$ReUe$ million	Re_c	T_∞ °R	ρ_∞ slugs/ft^3	α deg.
64.3	0.1016	2500	0.056134	1.44E+06	509.76	0.002208	2
85.7	0.1355	2500	0.074817	1.91E+06	509.76	0.002208	2, 8, 12, 16
98.6	0.1728	8000	0.086079	2.09E+06	490.15	0.001868	2
118.4	0.2073	8000	0.098126	2.51E+06	490.15	0.001868	2
128.2	0.2246	8000	0.106248	2.72E+06	490.15	0.001868	0, 2, 8, 16
123.8	0.2493	15000	0.095785	2.45E+06	465.22	0.001496	2
125.8	0.2533	15000	0.097333	2.49E+06	465.22	0.001496	2
141.6	0.2851	15000	0.109557	2.80E+06	465.22	0.001496	2

2.3 Cruise Power Conditions

The USM3D code has an actuator disk to mathematically model the cruise propellers, which creates the global effect of thrust and torque of the propellers. An actuator disk model would not capture the details of the blades or physics of flow from propeller tips but does provide an efficient means for representing the thrust and torque from the propellers. The actuator disk model was a practical approach to efficiently compute hundreds of solutions for the X-57 aerodynamic database.

The actuator disk inputs for cruise power were thrust coefficient (C_T), torque coefficient (C_Q), and advance ratio (J). These parameters were normalized for the USM3D code and are specified as $C_{T,usm}$, $C_{Q,usm}$, and J_{usm}. The cruise propellers were designed for maximum cruise efficiency and were best modeled with a Goldstein distribution [28]. A MATLAB/octave script was created to compute and output the Goldstein thrust and torque radial distributions. The algorithm in the MATLAB script used to find the distributions was based on Reference [29]. The inputs to the MATLAB script included the inner and outer radius, $C_{T,usm}$, J_{usm}, the number of propellers, and the number of output stations along the radius. For this work, 103 stations along the radius were used. The script outputs of the Goldstein thrust and torque coefficient distributions were copied into a file called projectname.patchdata, which USM3D uses for user-defined thrust and torque distributions, along with the projectname.inpt file, to run powered simulations.

The cruise power conditions studied in this paper are listed in Tables 2 to 9. The thrust and torque distributions as a function of radius are shown in Figures 6–13. The negative thrust values were meant to represent an idling condition.

Table 2. Cruise Power Conditions for 64.3 KTAS, 2250 RPM, and J = 0.6.

Thrust lbf	Torque $lbf-ft$	C_T	C_Q	J	$C_{T,usm}$	$C_{Q,usm}$	J_{usm}
104.51	64.97	0.0539	0.0067	0.6	0.00695	0.00173	0.19099
194.16	121.64	0.1001	0.0125	0.6	0.01291	0.00323	0.19099
275.98	184.47	0.1422	0.0190	0.6	0.01835	0.00491	0.19099
338.40	243.87	0.1744	0.0251	0.6	0.02250	0.00649	0.19099

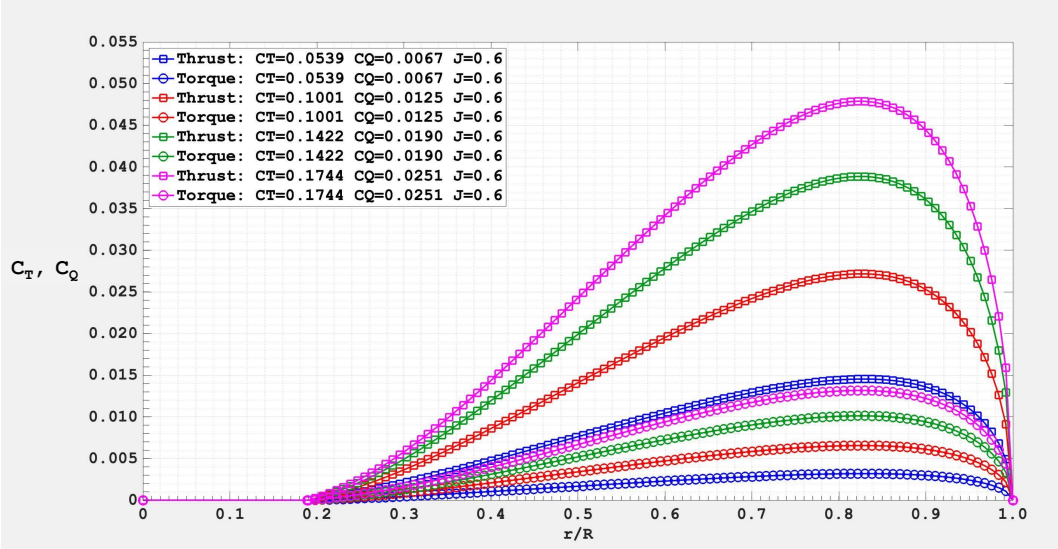

Figure 6. Thrust and torque distributions for cruise power conditions at an airspeed of 64.3 KTAS, 2250 RPM, and J = 0.6.

Table 3. Cruise Power Conditions for 85.7 KTAS, 2250 RPM, and J = 0.8.

Thrust lbf	Torque $lbf-ft$	C_T	C_Q	J	$C_{T,usm}$	$C_{Q,usm}$	J_{usm}
-0.79	11.44	-0.0004	0.0012	0.8	-0.00005	0.00030	0.25465
96.80	74.99	0.0499	0.0077	0.8	0.00644	0.00199	0.25465
194.63	151.25	0.1003	0.0156	0.8	0.01294	0.00402	0.25465
284.53	233.85	0.1466	0.0241	0.8	0.01892	0.00622	0.25465

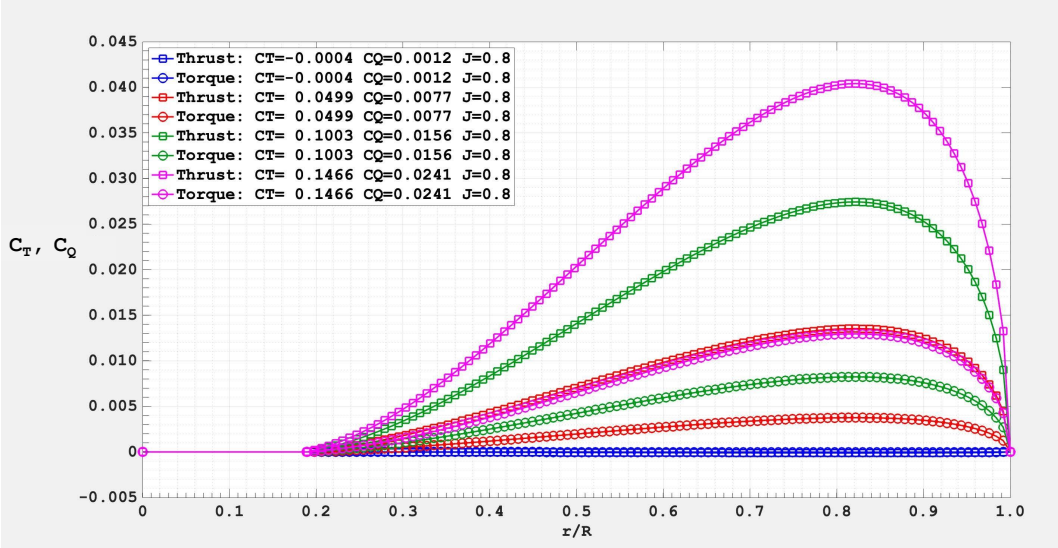

Figure 7. Thrust and torque distributions for cruise power conditions at an airspeed of 85.7 KTAS, 2250 RPM, and J = 0.8.

Table 4. Cruise Power Conditions for 98.6 KTAS, 2250 RPM, and J = 1.0.

Thrust lbf	Torque $lbf-ft$	C_T	C_Q	J	$C_{T,usm}$	$C_{Q,usm}$	J_{usm}
-10.43	1.85	-0.0064	0.0002	1.0	-0.00082	0.00006	0.31831
78.71	73.56	0.0479	0.0090	1.0	0.00618	0.00231	0.31831
167.68	156.95	0.1021	0.0191	1.0	0.01317	0.00493	0.31831
249.84	246.12	0.2	0.0300	1.0	0.01963	0.00773	0.31831

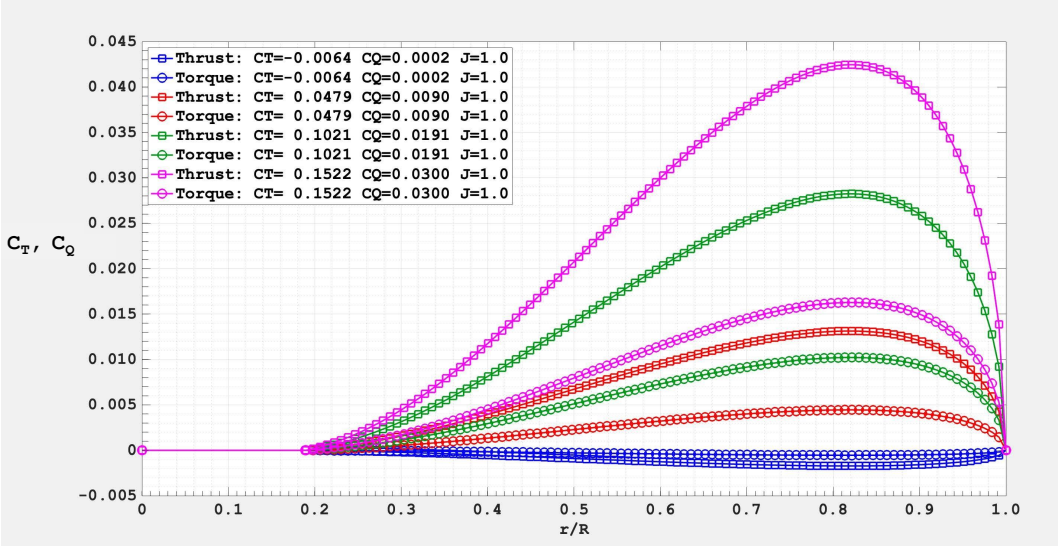

Figure 8. Thrust and torque distributions for cruise power conditions at an airspeed of 98.6 KTAS, 2250 RPM, and J = 1.0.

Table 5. Cruise Power Conditions for 118.4 KTAS, 2250 RPM, and J = 1.2.

Thrust lbf	Torque $lbf-ft$	C_T	C_Q	J	$C_{T,usm}$	$C_{Q,usm}$	J_{usm}
-13.88	-2.79	-0.0085	-0.0003	1.2	-0.00109	-0.00009	0.38197
81.78	89.68	0.0498	0.0109	1.2	0.00642	0.00282	0.38197
176.51	194.64	0.1075	0.0237	1.2	0.01387	0.00612	0.38197

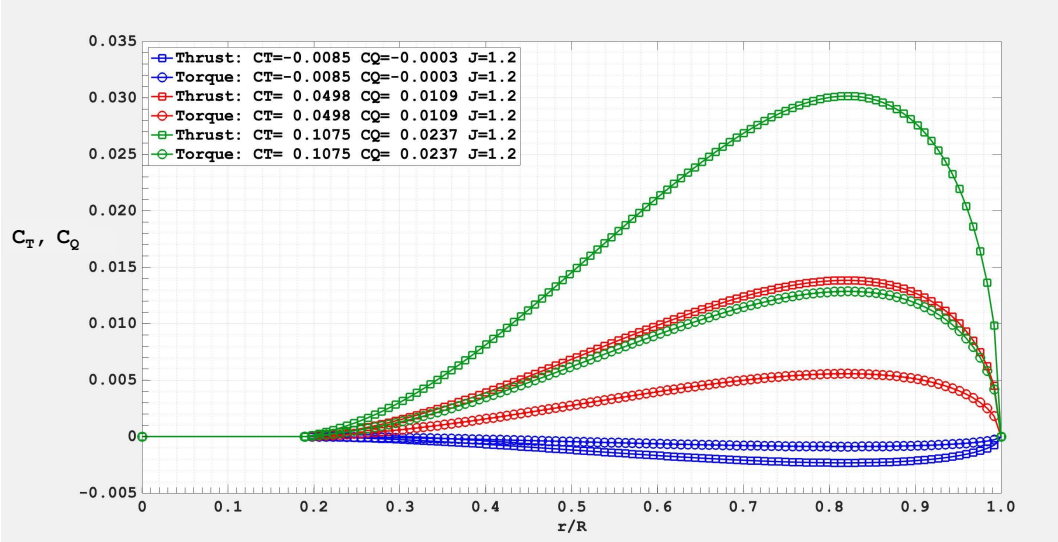

Figure 9. Thrust and torque distributions for cruise power conditions at an airspeed of 118.4 KTAS, 2250 RPM, and J = 1.2.

Table 6. Cruise Power Conditions for 128.2 KTAS, 2250 RPM, and J = 1.3.

Thrust lbf	Torque $lbf-ft$	C_T	C_Q	J	$C_{T,usm}$	$C_{Q,usm}$	J_{usm}
-60.07	-47.67	-0.0366	-0.0058	1.3	-0.00472	-0.00150	0.41380
36.57	47.63	0.0223	0.0058	1.3	0.00287	0.00150	0.41380
135.57	158.76	0.0826	0.0193	1.3	0.01065	0.00499	0.41380
230.09	279.87	0.1401	0.0341	1.3	0.01808	0.00879	0.41380

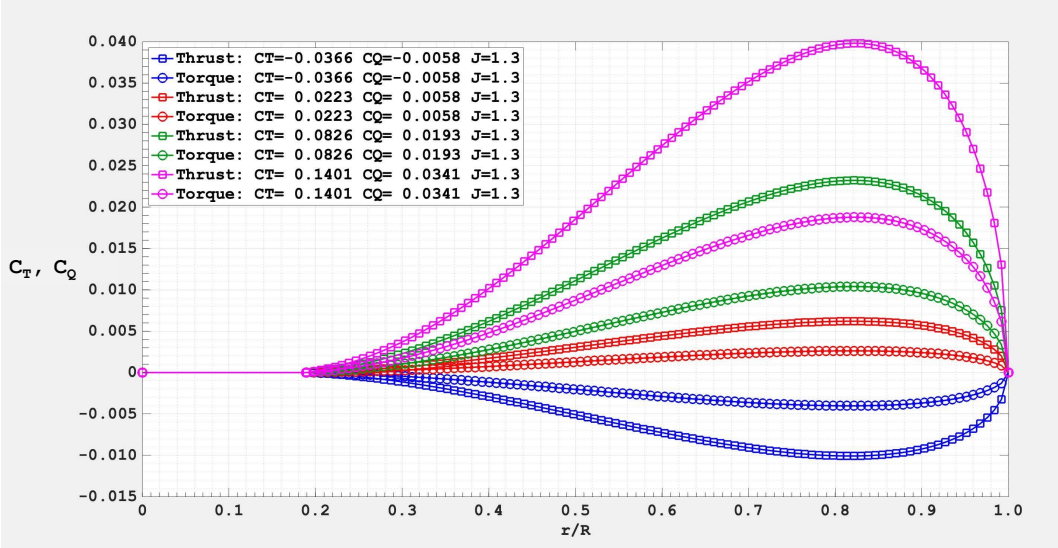

Figure 10. Thrust and torque distributions for cruise power conditions at an airspeed of 128.2 KTAS, 2250 RPM, and J = 1.3.

Table 7. Cruise Power Conditions for 123.8 KTAS, 2250 RPM, and J = 1.4.

Thrust lbf	Torque $lbf-ft$	C_T	C_Q	J	$C_{T,usm}$	$C_{Q,usm}$	J_{usm}
-7.44	0.35	-0.0057	0.0001	1.4	-0.00073	0.00001	0.44563
74.49	93.74	0.0567	0.0143	1.4	0.00731	0.00368	0.44563
154.69	197.584	0.1177	0.0301	1.4	0.01518	0.00776	0.44563

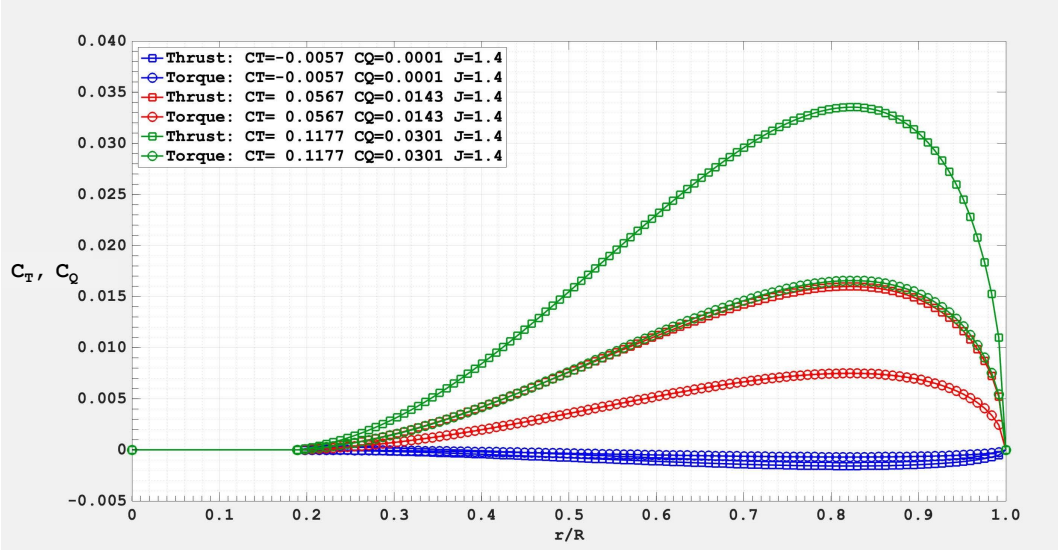

Figure 11. Thrust and torque distributions for cruise power conditions at an airspeed of 123.8 KTAS, 2250 RPM, and J = 1.4.

Table 8. Cruise Power Conditions for 125.8 KTAS, 2000 RPM, and J = 1.6.

Thrust lbf	Torque $lbf-ft$	C_T	C_Q	J	$C_{T,usm}$	$C_{Q,usm}$	J_{usm}
3.10	11.10	0.0030	0.0021	1.6	0.00039	0.00055	0.5093
72.11	102.68	0.0694	0.0198	1.6	0.00896	0.00510	0.5093
139.33	205.16	0.1341	0.0395	1.6	0.01731	0.01019	0.5093

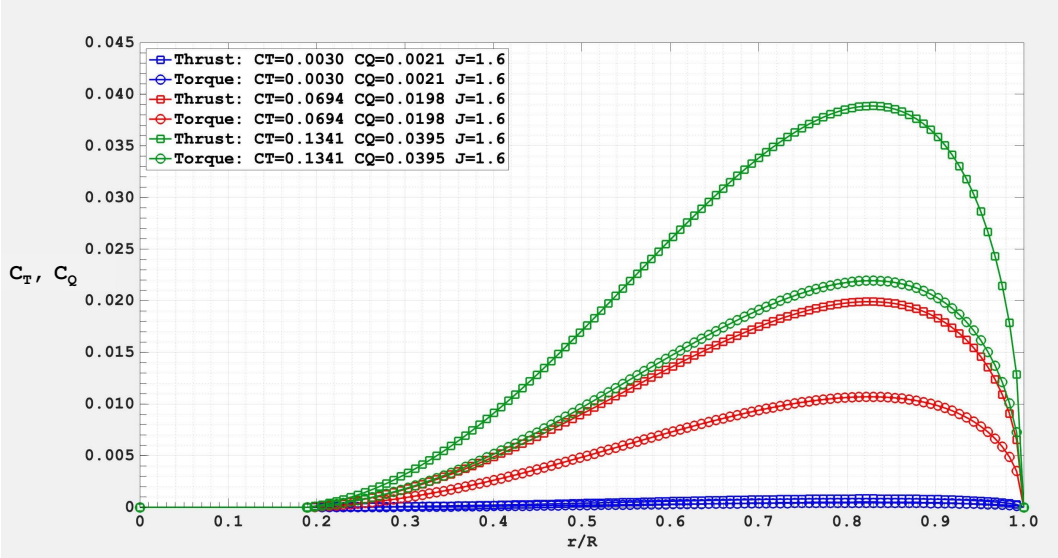

Figure 12. Thrust and torque distributions for cruise power conditions at an airspeed of 125.8 KTAS, 2000 RPM, and J = 1.6.

Table 9. Cruise Power Conditions for 141.6 KTAS, 2000 RPM, and J = 1.8.

Thrust lbf	Torque $lbf-ft$	C_T	C_Q	J	$C_{T,usm}$	$C_{Q,usm}$	J_{usm}
-52.37	-62.45	-0.0504	-0.0120	1.8	-0.00651	-0.00310	0.57296
19.01	35.10	0.0183	0.0068	1.8	0.00236	0.00174	0.57296
93.13	150.07	0.0897	0.0289	1.8	0.01157	0.00746	0.57296
128.13	209.67	0.1234	0.0404	1.8	0.01591	0.01042	0.57296

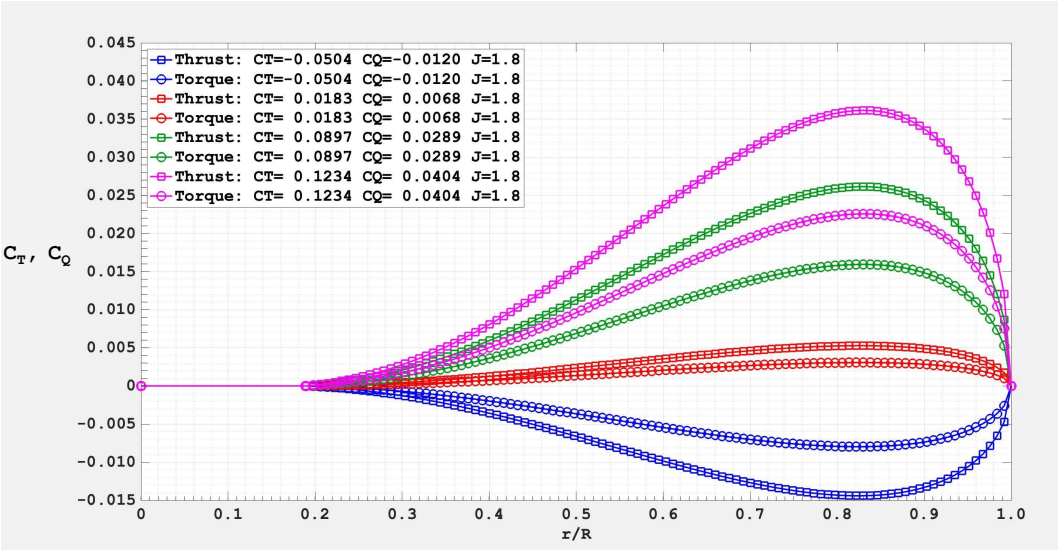

Figure 13. Thrust and torque distributions for cruise power conditions at an airspeed of 141.6 KTAS, 2000 RPM, and J = 1.8.

2.4 Initial and Boundary Conditions

A no-slip boundary condition was used on all solid surfaces. For these subsonic flow conditions, a characteristic inflow and outflow boundary condition was used at the inflow face of the computational domain and at the downstream outflow face of the computational domain. The inflow boundary condition was implemented by setting the Mach number, Reynolds number and temperature. A characteristic inflow and outflow boundary condition was also used along the far field, lateral faces of the computational domain. The characteristic boundary condition used fixed and extrapolated Riemann invariants of the incoming and outgoing waves along characteristic directions defined normal to the boundary. Local velocity components and speed of sound were computed from the invariants, density was computed from the entropy relationship and pressure was computed from the ideal gas law using the square of the speed of sound.

An actuator disk boundary condition was used on an annulus patch to model the cruise propellers at the wingtips. The actuator disk model in Kestrel can be implemented with a uniform loading or with a triangular radial thrust distribution. The triangular radial thrust distribution is defined by a linear radial thrust distribution from T=0 at the hub, to the maximum thrust (T_{max}) at a position of ($r_{T_{max}}/R$), and then a linear decrease to T=0 at the propeller tip ($r/R = 1$). The triangular thrust distribution option was used successfully to represent the thrust distributions of the high-lift propellers for studies with the landing and takeoff configurations, but it was questioned if it was appropriate for representing the thrust distribution of cruise propellers for the cruise configuration.

A few solutions were computed with Kestrel using two triangular thrust distributions and the data were compared with the USM3D Goldstein method in an effort to guide the decision of whether a triangular thrust distributions would be a suitable substitution for the Goldstein distribution. One triangular thrust distribution was set for the maximum thrust at a radial position 50% of the tip radius (T_{max} at r=0.5R) and the other with maximum thrust at a radial position 90% of the tip radius (T_{max} at r=0.9R). The inputs for the Kestrel actuator boundary condition included the RPM, the thrust vector direction, the total thrust, and the position of the maximum thrust along the radius. Since the grids were made with positive x in the flow direction, the thrust vector for the high-lift propellers was specified as (-1, 0, 0). A positive RPM is used when the rotation gives a right-hand rule vector in the direction of the thrust vector. Therefore, a positive RPM was used to model the propellers rotating in the direction opposing the wingtip vortex. A comparison of the triangular distributions (T_{max} at r=0.9R) of thrust and torque with the Goldstein distributions for T = 284.53 lbf and Q = 233.85 lbf-ft at 85.7 KTAS and α = 2° is shown in Figure 14. Although the triangular thrust distribution generally approximates the Goldstein distributions, there are obvious discrepancies, especially at the maximum thrust location.

The comparisons of rolling moment and drag coefficients between the Kestrel triangular thrust distributions results and the USM3D Goldstein thrust distribution data are shown in Figure 15. First, the USM3D Goldstein distribution produced larger negative rolling moment coefficients (Figure 15(a)), than the triangular thrust

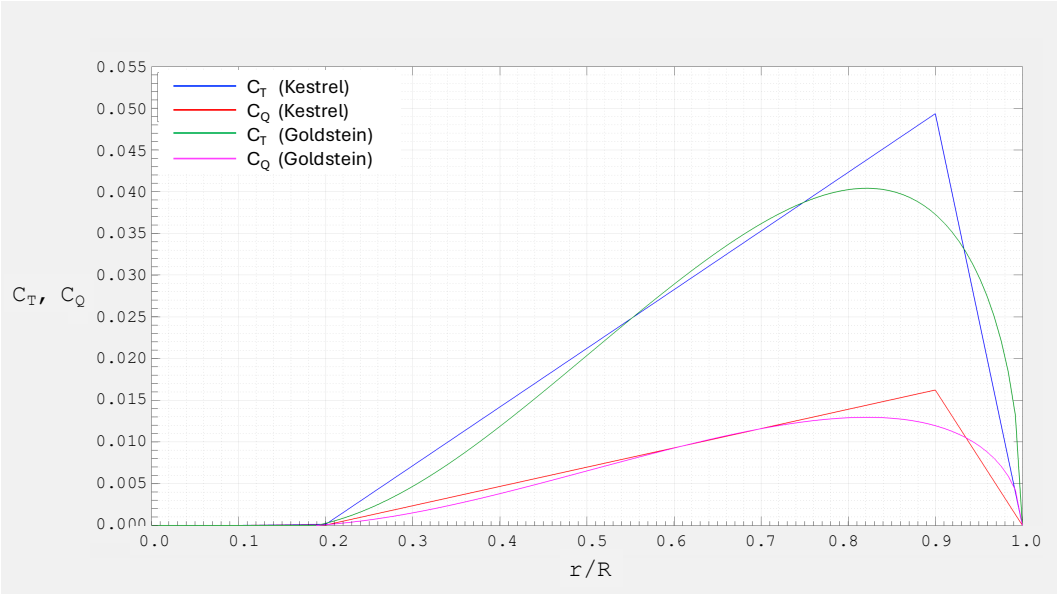

Figure 14. A comparison of the Kestrel triangular distributions with the Goldstein distributions for $T = 284.53$ lbf and $Q = 233.85$ lbf-ft at 85.7 KTAS and $\alpha = 2°$.

distributions in Kestrel. The location of maximum thrust in the Kestrel triangular thrust distributions had no effect on rolling moment coefficient for $C_T = 0.15$. Second, the USM3D Goldstein distribution produced significantly lower drag coefficients (Figure 15(b)), compared to the triangular thrust distributions in Kestrel. Therefore, Kestrel was not used for the rest of the solutions shown in this paper, since the triangular thrust distribution was not a good representation of the Goldstein distributions as seen in Figure 14 and measured by the overprediction of drag. Additionally, the triangular thrust distribution with T_{max} at r=0.5R had an even higher drag coefficient than with T_{max} at r=0.9R for $C_T = 0.15$ and therefore, solutions were not computed with T_{max} at r=0.5R for the other C_T values. Note that the propeller thrust force is not considered in the computation of forces and moments for the airplane configuration. The drag change due to propeller thrust represents the result of increased drag due to the higher velocity flow over the configuration and the reduction of induced drag.

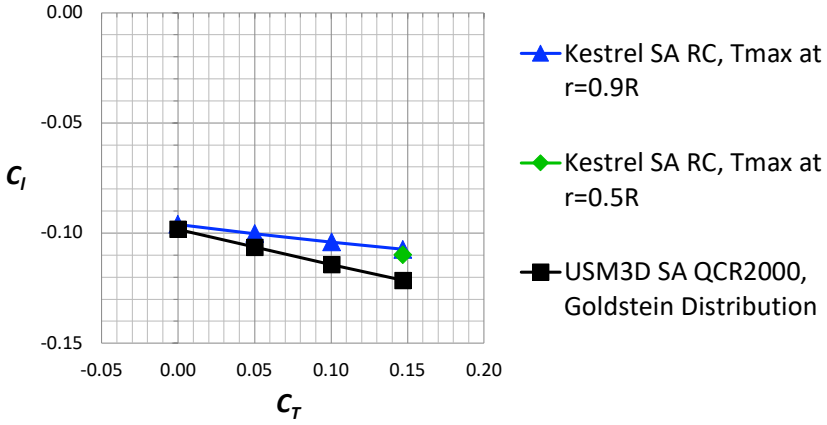

(a) Rolling Moment Coefficient

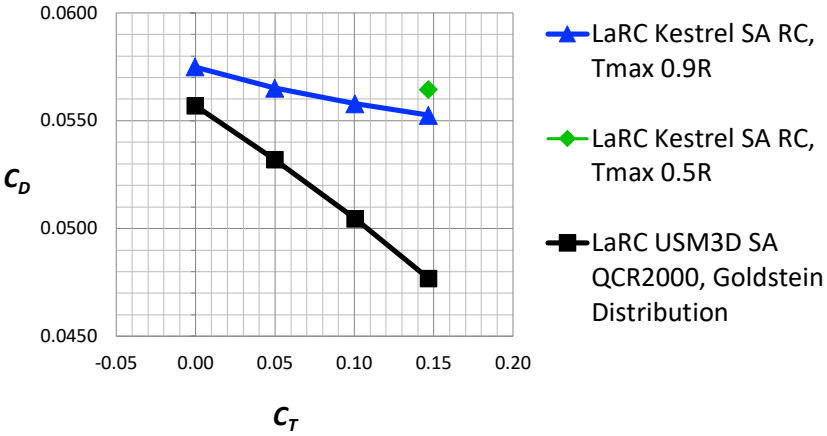

(b) Drag Coefficient

Figure 15. The effect of thrust distributions on rolling moment coefficient and drag coefficient for 85.7 KTAS ($M = 0.1355$), at an altitude of 2500 feet, and $\alpha = 2°$.

2.5 Input File and Solution Procedure

A typical USM3D input file for a time-accurate solution is shown in Figure 16. The freestream conditions are specified with the Mach number (M), the angle of attack (alpha) in degrees, the sideslip angle (beta) in degrees, the freestream Reynolds number per unit length specified in millions (ReUe, mil), and the freestream temperature (T_∞) in degrees Rankine. The reference parameters specific for each configuration are area (sref), length (cref), span (bref), moment center in X-direction (xmc), moment center in Y-direction (ymc), and moment center in Z-direction (zmc).

The solutions were computed with a time-accurate approach (itimeacc = 2), which required a timestep (deltat), the number of subiterations (ncyc) allowed for each timestep, and a total number of timesteps (ntstep). The timestep used in this study is discussed in further detail in Section 2.10. The irest parameter was used for

Mach	alpha	beta	ReUe,mil	Tinf,dR	itwall	Tw/Tinf	ipwall
0.1355	8.0	0.0	0.07488	509.73	0	-1.0	0
sref	cref	bref	xmc	ymc	zmc		
4800.00	25.560833	189.73666	154.797	0.0	64.527		
ioverset	impl	dt/cfl1	iramp	cfl2	cflmin	GS_tol	crelax
0	1	-20.0	5	150.0	1.0	-20.0	0.7
itimeacc	deltat	ntstep	res-step	imvgrd	isolavg	nbgnavg	
2	7.25	1000	-3.00	0	1	1000	
irest	mstage	iresmth	dqmax	p_break	p_min	limiter	lim_coeff
1	3	1	0.1	0.05	0.001	0	0.01
nupdate	nwrest	nwflo	nwflobgn	ipltqn	idiagnos	nodeypl	lim_frz
1	1000	0	0	2	1	0	0
iorder	lapl-avg	high-bc	ifds	ivisc	itrp	EV_lim	iqcrflg
2	1	1	1	2	0	0	1
ncyc	nengines	nsinkbc	nrotor	compF&M	p_bc1002		cldes
20	0	0	0	-1	0.714290		0.0
ikeord	icons	nstagek	t_dtfact	t_intsity	mut/mul	ratiokp	dkemax
1	1	10	1.0	1.0e-3	0.009	0.00	0.25
inl	ilhg	iwallf	icompCorr	itempCorr	itk	isk	idt_proc
0	-14	0	0	0	2	0	0
f1kemax	itranflg						
1.0	0						

Figure 16. An input file for USM3D with the SA QCR turbulence model selected.

a new solution (irest = 0) or to continue a solution, which had a restart file available (irest = 1). Second-order spatial accuracy was used (iorder = 2). The spatial differencing scheme for inviscid fluxes was the Roe flux difference splitting scheme (ifds = 1), typical for Mach numbers less than 2.5. Flux limiters are used within CFD codes to prevent oscillations due to shocks and discontinuities by limiting the values of the spatial derivatives. Typically, a limiter is required and turned on for supersonic flows and is turned off for subsonic flows. Turning on the limiter can also help to run unstable cases, but it does affect the predicted drag value. Therefore, the limiter was off (limiter = 0) except for a few troubled cases at high angles of attack where the MINMOD limiter (limiter = 1) was used. However, because of the effects of the limiter on drag, additional solutions were computed for the troubled cases on a modified mesh. The calculations in this paper were fully turbulent as computed with the SA turbulence model (ivisc = 2) with the Quadratic Constitutive Relation (QCR) (iqcrflg = 1).

2.6 Computer Platform

The resources supporting this work were provided by the NASA High-End Computing (HEC) Program through the NASA Advanced Supercomputing (NAS) Division at Ames Research Center. The Pleaides supercomputer at NAS was used for all the computational solutions within this report. The solutions were computed using 480 cores on the Ivy nodes.

2.7 Coordinate System

The reference coordinate system used for the USM3D and Kestrel codes is shown in Figure 17, with the reference axes positioned at the main coordinate system origin for the project ((x, y, z) = (0 inches, 0 inches, 0 inches)). The positive y-axis was

aligned with the pilot's right wing. The positive x-axis was in the direction of the freestream flow and the y-axis and z-axis are specified normal to the x-axis. The angle of attack (α) was defined in the x-z plane and the sideslip angle (β) was defined in the x-y plane. The moment reference center ((x, y, z) = (154.797 inches, 0 inches, 64.527 inches)) is shown in Figure 18.

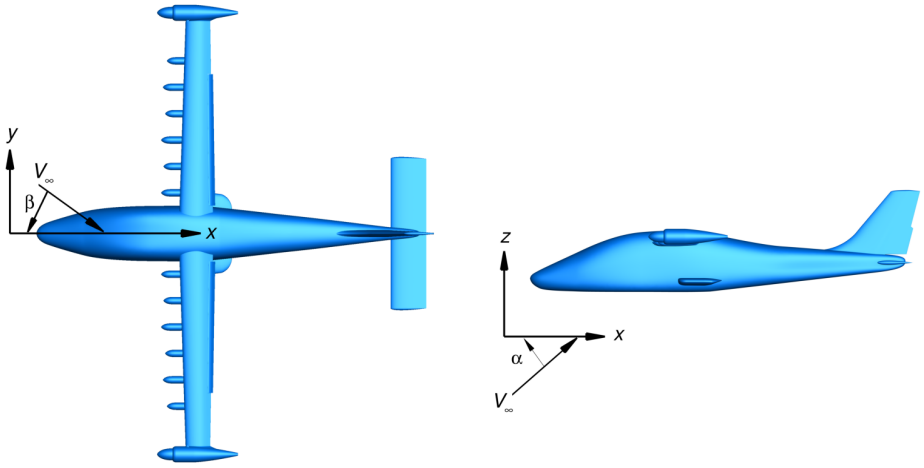

(a) Top View, x-y plane (b) Side View, x-z plane

Figure 17. The computer aided design (CAD) geometry reference coordinate system.

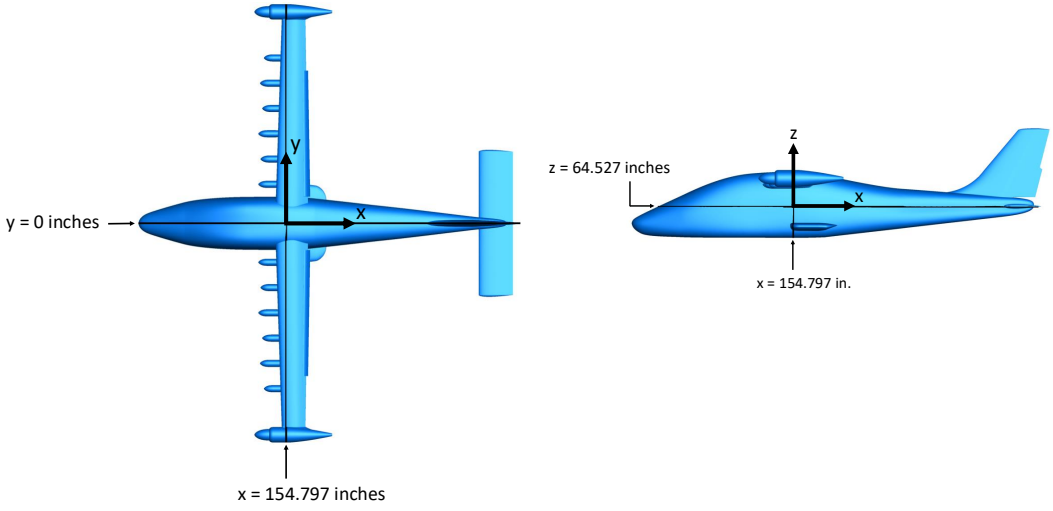

(a) Top View, x-y plane (b) Side View, x-z plane

Figure 18. The moment reference center location.

2.8 Geometry Definition

The Vehicle Sketch Pad (OpenVSP) software [30, 31] was used to generate the geometry of the cruise-powered X-57 Maxwell Mod III configuration (Figure 4), which had cruise propellers operating and the high-lift blowing propellers stowed. The X-57 Maxwell had a root chord (25.56 inches) that was nearly half the original Tecnam P2006T root chord (54.84 inches). Figure 19(a) shows a top down view of the airplane wireframe with the Tecnam wing shaded blue and the X-57 wing shaded green (with a pink and blue arrow highlighting the boundary). Figure 19(b) shows an isometric view of the wing root region, again with the larger Tecnam wing shaded blue and the smaller X-57 wing shaded green. The intersection of the X-57 wing into the fuselage was completely different than the original Tecnam P2006T because of the large difference in root chords. The fit routine in the OpenVSP software was used to modify the original computer aided design (CAD) of the isolated fuselage, to define the new fuselage outer mold line using analytical curves in both the x-y and y-z planes. This fuselage from the OpenVSP fit routine will be referred to as the 'preliminary fuselage'. The preliminary fuselage was used for CFD computations at NASA Langley for the first three years before the actual X-57 flight fuselage geometry was available. During the structural design for the X-57 Maxwell, it was discovered that the preliminary fuselage would not contain the hardware that was designed to attach the X-57 Mod III wing to the original Tecnam P2006T fuselage structure within its outer mold line. A final 'X-57 fuselage' was designed to completely contain the structure required to support the wing. In future publications, the final X-57 flight fuselage geometry will be modeled in NASA Langley computational results. However, this paper reports results for the X-57 Mod III geometry with the preliminary fuselage.

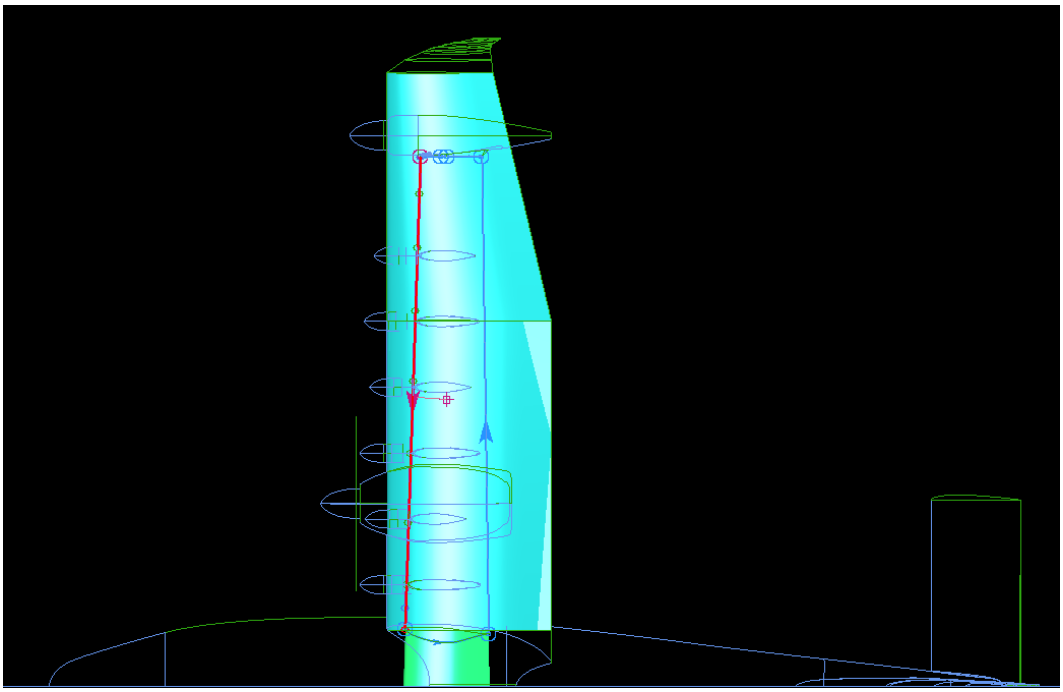

(a) Top down view of the smaller X-57 wing inside of the Tecnam wing

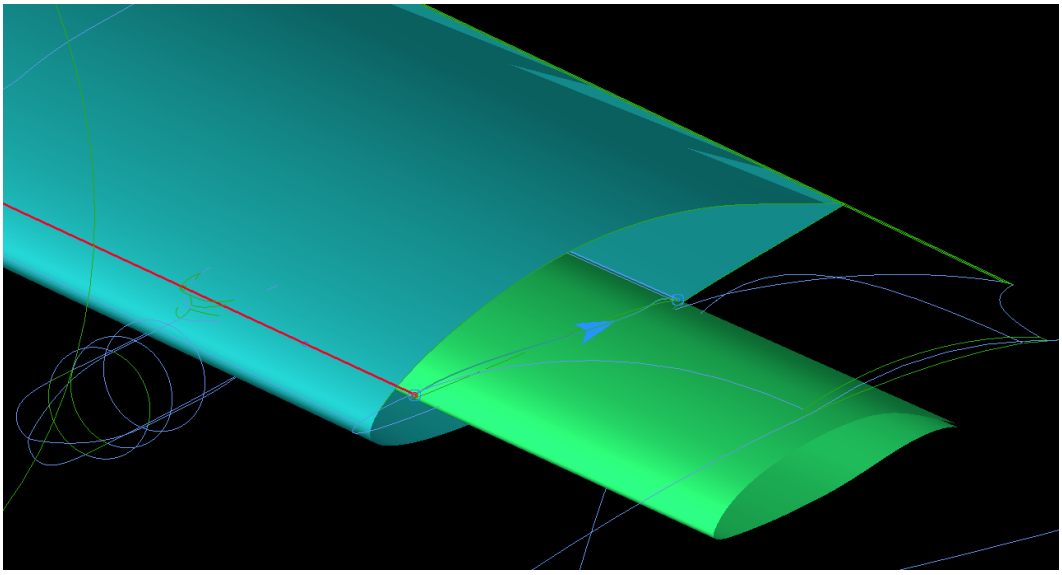

(b) Isometric View of wing root region with the smaller X-57 wing inside of the Tecnam wing

Figure 19. Comparison of the Tecnam wing (blue) with the X-57 wing (green).

The NASA LaRC GEOmetry LABoratory (GEOLAB) supported this effort by processing the CAD geometry from OpenVSP for grid generation. The OpenVSP geometry was imported into the commercial CAD package, Siemens NX. All the components were intersected and a final geometry was sewn together to create a single, water-tight configuration.

The shaded CFD surface of the powered X-57 Mod III is shown in (Figure 20) with details of some components shown in Figure 21. The geometry with the preliminary fuselage included the cruise propellers, the cruise wing (no flap deflection), a neutral horizontal stabilator, neutral ailerons, a vortex generator (VG) (Figure 21(b)) on the wingtip nacelle, a t-strip (Figure 21(d)) on the rudder of the vertical tail, a gurney flap (Figure 21(f)) on the stabilator, and a wingtip fillet at the intersection of the wing and wingtip nacelle.

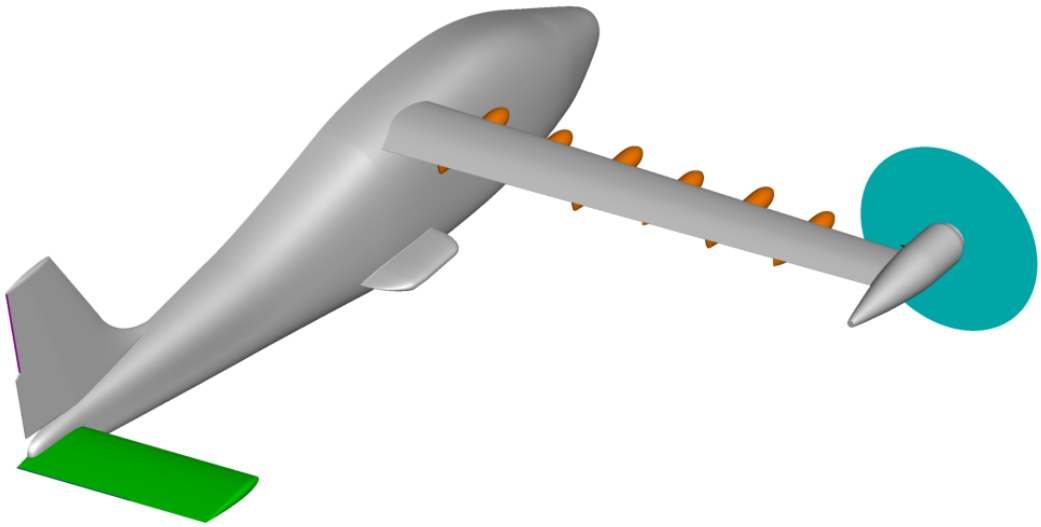

Figure 20. The shaded CFD semispan geometry with the cruise wing, a neutral stabilator (green), high-lift nacelles (orange), and cruise propellers (cyan).

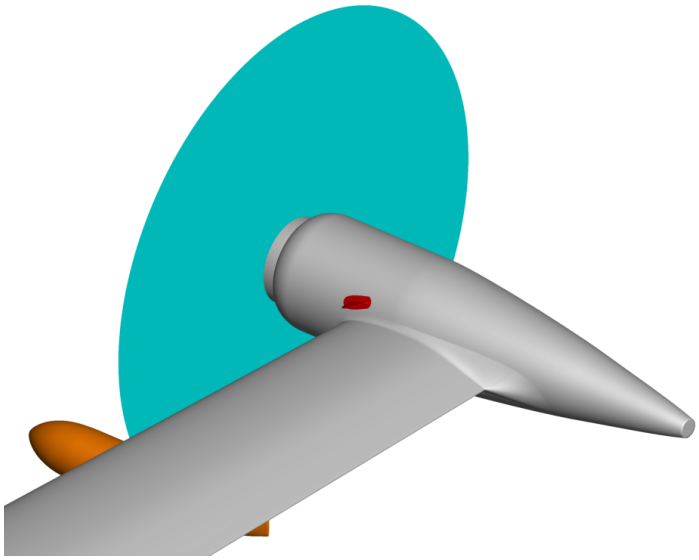

(a) Cruise propeller (cyan), Outboard High-Lift Nacelle (orange), and Vortex Generator (red) on the Starboard Wingtip Nacelle

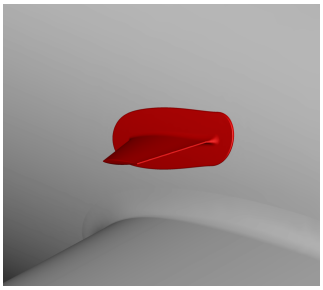

(b) Vortex Generator (red)

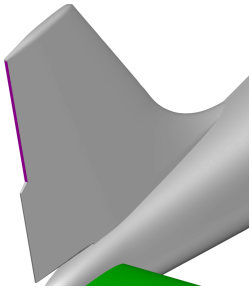

(c) Vertical Tail and T-strip

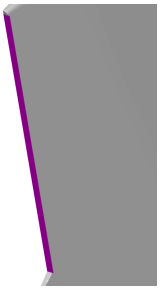

(d) T-strip (magenta)

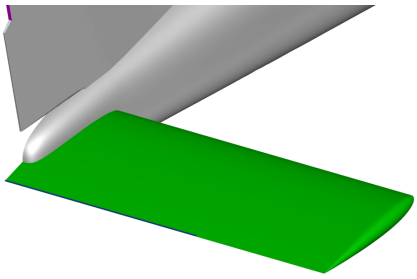

(e) Stabilator and Gurney Flap

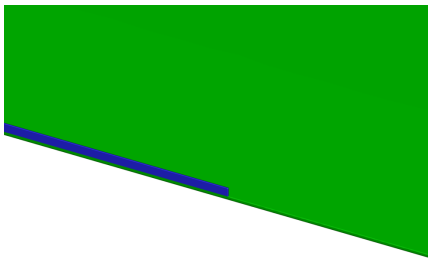

(f) Gurney Flap (blue)

Figure 21. Details of the shaded CFD geometry used for the X-57 Maxwell Mod III configuration with cruise power.

2.9 Grid Generation

The NASA LaRC GEOLAB also supported the grid generation effort for the meshes used in this investigation. The geometry definition was prepared in GridTool [32] by creating surface patches on the configuration and by placing sources throughout the domain to capture configuration characteristics. The sources can be visualized in Figure 22. The projectname.rst output file from GridTool was used to generate the computational domains with the Heldenmesh unstructured grid generation software, developed by Helden Aerospace Inc. [33].

The GridTool software has an internal boundary-layer calculator that was used to generate the parameters needed to create the viscous portion of the mesh. The inputs to the calculator included the Reynolds number based on reference chord (Re_c), the reference chord (c_{ref}), the growth rate of the successive ratio (b), the nondimensional first node height (y^+_{node}), and the maximum number of layers in the boundary layer (NL). The outputs from the calculator included the successive ratio growth rate for the viscous layers (a) and the dimensional first node height (δ_1).

The Heldenmesh software used an advancing layers method similar to reference [34] to create a boundary layer mesh as the mesh propagated from the surface. For the tetrahedral mesh needed for USM3D, each prism layer in the boundary layer was divided into three cells per prism. An advancing front method, similar to reference [35], was used to generate the inviscid volume mesh from the boundary layer to the farfield. The volume growth rate was computed with Equation 1.

$$\delta_j = \delta_1[1 + a(1 + b)^{(j-1)}]^{(j-1)} \tag{1}$$

The Heldenmesh software produced an unstructured, tetrahedral mesh needed for the legacy USM3D code in the .cogsg, .mapbc and .bc formats. The three USM3D grid files were inputs to the CREATE-AV utility called CARPENTER, which was used to generate the mixed-element mesh for Kestrel. The boundary layer cells of the all-tetrahedral mesh were merged into prisms for the Kestrel flow solver and the mesh was written in an .avm format for the Kestrel KCFD code.

The full domain mesh was specified 10,000 inches from the geometry, which was approximately 400 reference chord lengths from the geometry. The placement of sources for defining grid resolution for the cruise wing configuration, with propeller volume sources at the actuator disk plane, are shown in yellow in Figure 22.

Three meshes were used for this study. The mesh sizes are shown in Table 10 and the boundary layer settings are shown in Table 11. The first mesh had a first cell height for a $y^+_{cell} = 0.125$ to prevent $y^+_{cell} > 1$ on the leading edge, especially in the region behind the propeller with increased velocity relative to the freestream. This mesh was initially used for the whole range of conditions, but some cases were difficult to converge. In order to determine if the very small y^+_{cell} value was the cause of the convergence problem, a second mesh was created with a first cell height specified as three times the height in mesh 1, $y^+_{cell} = 0.375$. The mesh with $y^+_{cell} = 0.375$ was still small enough to keep y^+_{cell} at or less than 1 on the leading edge behind the propellers. The second mesh alleviated the convergence problems, but for some high angle of attack cases, the code still had stability issues and the troubled area was found behind the t-strip. Therefore, a third mesh was created by eliminating

the t-strip. As shown in Section 2.12, the effect of the t-strip was small. Therefore, the cases with stability issues at high angle of attack were run with mesh 3 (cases 26-35 and 125-129).

Table 10. Mesh Details, Sizes Specified in Millions.

Mesh	y^+_{cell}	y^+_{node}	Surface Triangles	Prisms	Pyramids	Tetrahedra	Total Cells
1	0.125	0.5	1.06	64.64	0.097	66.23	140.35
2	0.375	1.5	1.06	25.96	0.119	63.81	141.94
3	0.375	1.5	1.04	25.02	0.334	63.41	139.13

Table 11. Mesh Boundary Layer Settings.

Mesh	y^+_{cell}	y^+_{node}	δ_1	a	b	NL	Total Cells, Millions
1	0.125	0.5	0.0001485	0.1242	0.02	100	140.35
2	0.375	1.5	0.0004463	0.0949	0.02	100	141.94
3	0.375	1.5	0.0004463	0.0949	0.02	100	139.13

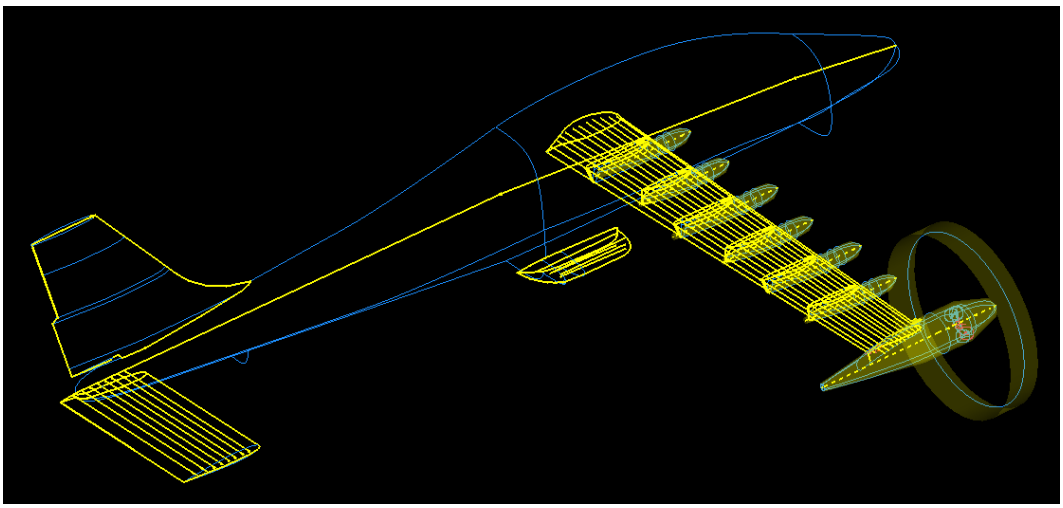

Figure 22. Placement of sources for defining grid resolution for the cruise wing configuration. Two volume source are used at the actuator disk plane.

2.10 Timestep

The USM3D code was run with a global time stepping, time-accurate RANS approach or also referred to as URANS. For USM3D nondimensionalization, the relationship between timestep ($delta_t$), Mach number and the number of time steps (N) to traverse a characteristic length (L_{char}) is shown in Equation 2. The distance a signal travels in one time step ($D_{t,char}$) is computed with Equation 3. The number of time steps (N) to traverse one characteristic length (L_{char}) is one convective time unit (CTU).

$$delta_{t,USM3D} = \frac{L_{char}}{N * M} \tag{2}$$

$$D_{t,char} = \frac{L_{char}}{N} \tag{3}$$

The characteristic length L_{char} used for this work was the mean aerodynamic chord, c_{ref}= 25.56 inches. A value of $N = 26$ in Equation 2 was used to determine the incremental timestep for the fluid to travel across the mean aerodynamic chord in 26 timesteps, or approximately $D_{char} = 1$ inch. The incremental timestep used in this study for each Mach number are listed in Table 12.

Table 12. Timestep as a Function of Mach Number.

Velocity, KTAS	M	$delta_t$ for $D_{t,char} = 1$ in/step	$delta_t$ for $D_{t,char} = 0.5$ in/step
64.3	0.1016	9.68	4.84
85.7	0.1355	7.25	3.63
98.6	0.1728	5.69	2.85
118.4	0.2073	4.74	2.37
128.2	0.2246	4.38	2.19
123.8	0.2493	3.94	1.97
125.8	0.2533	3.88	1.94
141.6	0.2851	3.45	1.72

To determine the effect of incremental timestep on aerodynamic coefficients, a solution was computed with $N = 26$ ($D_{char} = 1.0$ inch/step) for the first 8,000 timesteps, and then changed to a timestep computed with $N = 52$ ($D_{char} = 0.5$ inch/step) for timesteps 8,001–12,500. The coefficient averages and standard deviations were computed for 40 CTU, which was 1,040 total timesteps for $N = 26$ and 2,080 total timesteps for $N = 52$. The coefficient averages and standard deviations are shown in Tables 13 and 14 for the timesteps using $D_{char} = 1.0$ inch/step ($N = 26$) and $D_{char} = 0.5$ inch/step ($N = 52$), respectively. Tables 13 and 14 include the wind-axis system lift, drag, and pitching moment coefficients (C_L, C_D, and C_m, respectively). The body-axis system moment coefficients around the x-axis, y-axis and z-axis ($C_{m,X}$, $C_{m,Y}$, and $C_{m,Z}$, respectively) are also included. Note that the wind-axis pitching moment coefficient and the body-axis moment coefficient around the y-axis are equivalent.

The convergence history is shown in Figure 23. The lift coefficient decreased 0.3%, the drag coefficient increased 0.8%, and the moments remained nearly the same between the two timesteps. Therefore, the timestep for 1-inch increments was sufficient and there was no reason to pay the extra cost of running a smaller timestep. A minimum of a third-order drop in residual per timestep was used (res–step = -3) for the time-accurate solutions, and the code used subiterations to progress the solution until the drop in residuals reached the value of res–step, at which point a new iteration would commence. Most solutions reached a third-order drop in residuals within the 20 subiterations, but the number of subiterations could be increased if necessary to obtain better convergence.

Table 13. Data for 40 CTU Averaging Range for $D_{t,char} = 1.0$ inch/step.

	C_L	C_D	C_m	$C_{m,X}$	$C_{m,Y}$	$C_{m,Z}$
Average	1.5829	0.1031	-0.7435	-0.7062	-0.7435	-0.0611
Standard Deviation	0.0002	0.0000	0.0003	0.0003	0.0003	0.0000

Table 14. Data for 40 CTU Averaging Range for $D_{t,char} = 0.5$ inch/step.

	C_L	C_D	C_m	$C_{m,X}$	$C_{m,Y}$	$C_{m,Z}$
Average	1.5781	0.1039	-0.7434	-0.7047	-0.7434	-0.0607
Standard Deviation	0.0009	0.0001	0.0013	0.0004	0.0013	0.0000

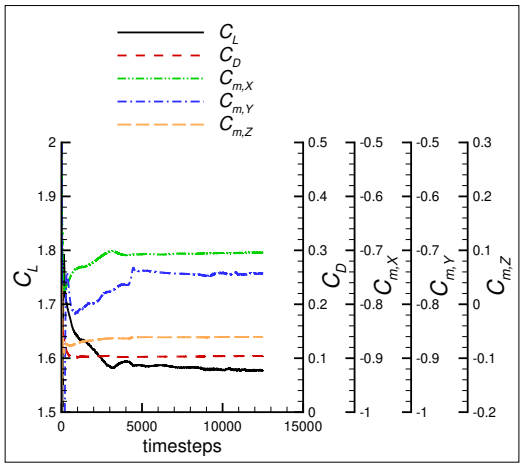

(a) Full Solution History

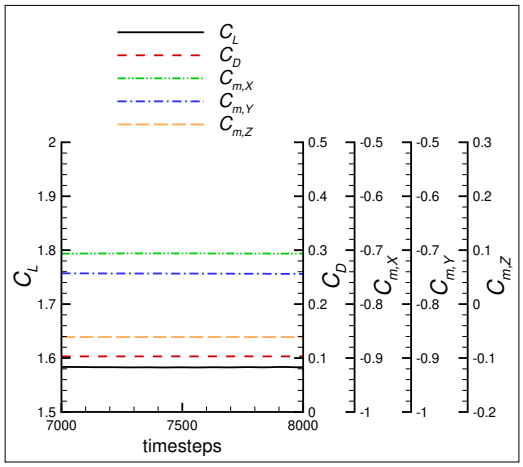

(b) Average 40 CTU for $D_{t,char} = 1.0$ in/step

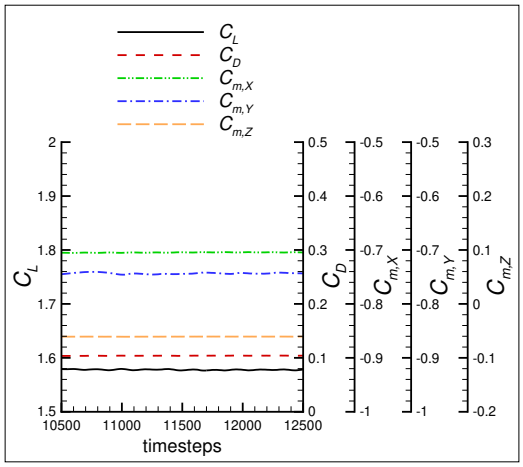

(c) Average 40 CTU for $D_{t,char} = 0.5$ in/step

Figure 23. Effect of timestep on forces and moments, 128.2 KTAS, $M = 0.2246$, and $\alpha = 8°$. Cruise propellers: T = 230.09 lbf/prop, Q = 279.87 lbf-ft/prop, 2250 RPM.

2.11 Convergence

Two main criteria were used to determine solution convergence; a drop in residual of two orders of magnitude and the convergence of force and moment coefficients to less than 0.5% change over a specified range of iterations. The coefficients were averaged over a range of at least 10 CTU using Equation 4. The standard deviation and the percent over range (POR) were also calculated for each coefficient over a specified range. The POR was calculated with Equation 5, where $C_{N,max-range}$ and $C_{N,max}$ are the values of the coefficient at the first and last iterations of the range, respectively. The solutions were deemed converged when the POR values were less than 0.5. In the situation where the coefficient was approaching zero, the POR values were larger than 0.5% because of the near zero average value of the coefficient in the denominator of Equation 5. These higher POR calculations when the average was near zero can be deceiving and therefore, engineering judgment was used with the standard deviation to determine if properly converged for cases where $POR > 0.5$. In general, it was easier to judge convergence when a solution was steady because the residuals were usually smooth, and the coefficients were constant with a very small standard deviation from the average. However, evaluating the convergence of the unsteady problems required engineering judgment in determining solution convergence and the averaging of coefficients was done over a reasonable period after which the solution became statistically stationary.

$$C_{average} = \frac{1}{range} \sum_{j=N_{max}-range}^{N_{max}} (C_j) \tag{4}$$

$$POR = \left(\frac{C_{N,max} - C_{N,max-range}}{C_{average}} \right) * 100 \tag{5}$$

An example of force and moment convergence data for a steady solution is shown in Table 15. In this example for the cruise configuration at $M = 0.1355$ and $\alpha = 2^\circ$, the lift coefficient, the drag coefficient, and the pitching moment coefficient are all very well converged. Note that the wind-axis pitching moment coefficient (C_m) and the body-axis moment coefficient around the y-axis ($C_{m,Y}$) are equivalent. A grouping of plots used to evaluate convergence is shown in Figure 24. There was a five-order reduction of both the mean flow and turbulence model residuals (Figure 24(a)) and the residual histories are mostly smooth. The subiteration residual convergence is very good, as shown in Figure 24(b). The force and moment coefficients shown in Figure 24(c) indicate good convergence as expected from the tabulated data in Table 15. In general, the solutions for $\alpha < 8^\circ$ were steady, while $\alpha \geq 8^\circ$ were slightly unsteady, but statistically stationary.

An example of force and moment convergence data for a slightly unsteady solution is shown in Table 16 and in Figure 25. In this example for $M = 0.2246$ and $\alpha = 8^\circ$, the forces and moments were still very well converged, but the solution was run for more than twice the number of timesteps as the steady example for $\alpha = 2^\circ$. There was still a five-order reduction of the mean flow residual and turbulence model residual had a four-order reduction but there were more spikes in the residuals as the solution developed (Figure 25(a)). The subiteration residual convergence was

very good, as shown in Figure 25(b). The force and moment coefficients shown in Figure 25(c) indicate good convergence although it took at least 5,500 timesteps to become statistically stationary.

A final example of force and moment convergence data for an unsteady solution is shown in Table 17 and in Figure 26. Again, in this example for $\alpha = 16°$, the force and moment coefficients were still well converged, but the solution took 8,000 timesteps before is was statistically stationary and the time averaging could start. The solution was continued to 10,000 time steps and the time averaging occurred from 9,000 to 10,000 time steps. The residuals were not as deeply converged as the other two examples, but there was over a four-order reduction of the mean flow residual and a third-order reduction in turbulence model residual (Figure 26(a)). The subiteration residual convergence was good, as shown in Figure 26(b). The force and moment coefficients shown in Figure 26(c) indicate good convergence.

Table 15. Typical Steady Convergence Data, 85.7 KTAS, $M = 0.1355$, $\alpha = 2°$, $T = 96.8$ lbf, $Q = 23.96$ lbf-ft, USM3D SA QCR, Range of 300 timesteps.

	C_L	C_D	C_m	$C_{m,X}$	$C_{m,Y}$	$C_{m,Z}$
Average	0.884	0.0532	-0.095	-0.425	-0.095	0.013
Standard Deviation	0.000	0.0000	0.000	0.000	0.000	0.000
POR	-0.03	0.02	0.00	0.03	0.00	0.38

Table 16. Typical Unsteady Convergence Data, 128.2 KTAS, $M = 0.2246$, $\alpha = 8°$, T = 135.57 lbf, Q = 158.76 lbf-ft, USM3D SA QCR, Range of 1,000 timesteps.

	C_L	C_D	C_m	$C_{m,X}$	$C_{m,Y}$	$C_{m,Z}$
Average	1.563	0.1060	-0.730	-0.688	-0.730	-0.057
Standard Deviation	0.001	0.0000	0.001	0.000	0.001	0.000
POR	-0.05	-0.08	0.07	0.07	0.07	-0.05

Table 17. Typical Unsteady Convergence Data, 128.2 KTAS, $M = 0.2246$, $\alpha = 16°$, T = 230.09 lbf, Q = 279.87 lbf-ft, USM3D SA QCR, Range of 1,000 timesteps.

	C_L	C_D	C_m	$C_{m,X}$	$C_{m,Y}$	$C_{m,Z}$
Average	2.053	0.2789	-1.991	-0.846	-1.991	-0.191
Standard Deviation	0.001	0.0002	0.000	0.001	0.000	0.000
POR	0.01	-0.04	-0.03	0.01	-0.03	0.00

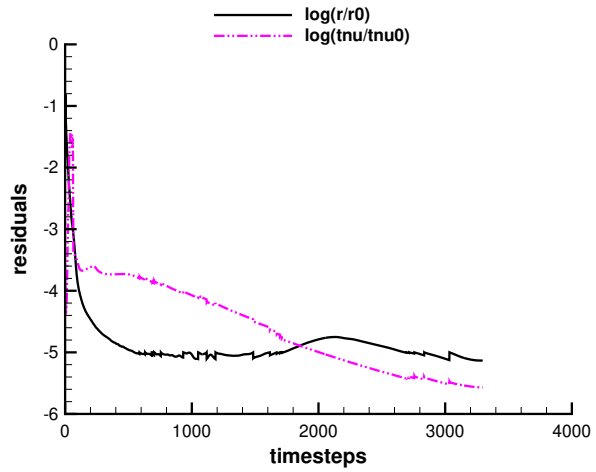

(a) Residuals

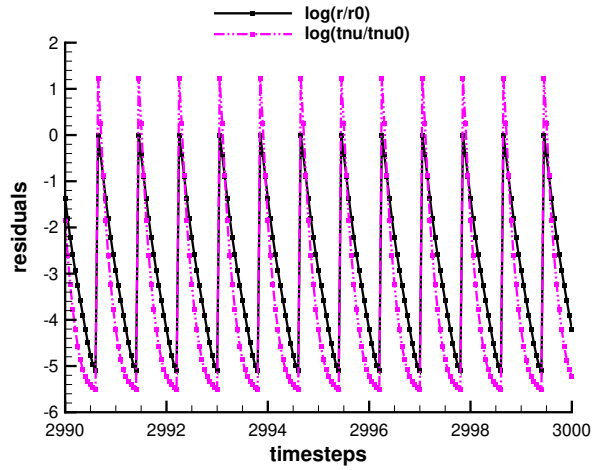

(b) Subiteration Residuals

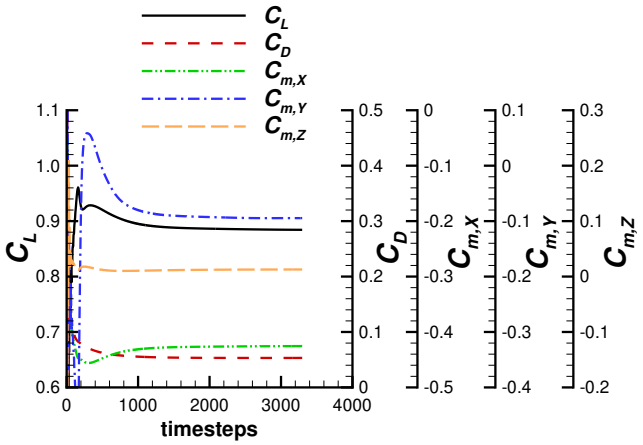

(c) Force and Moment Coefficients

Figure 24. A typical steady solution history for the cruise wing configuration at 85.7 KTAS, $M = 0.1355$, $\alpha = 2°$, T = 96.8 lbf, Q = 23.96 lbf-ft, USM3D SA QCR.

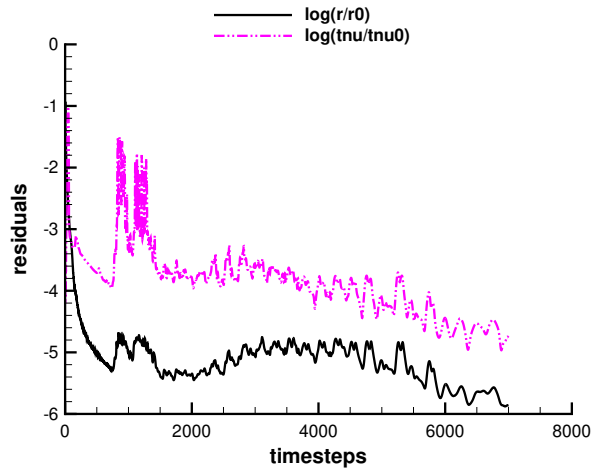

(a) Residuals

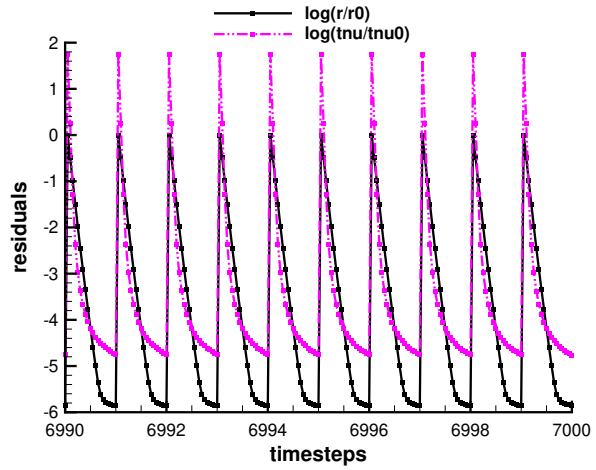

(b) Subiteration Residuals

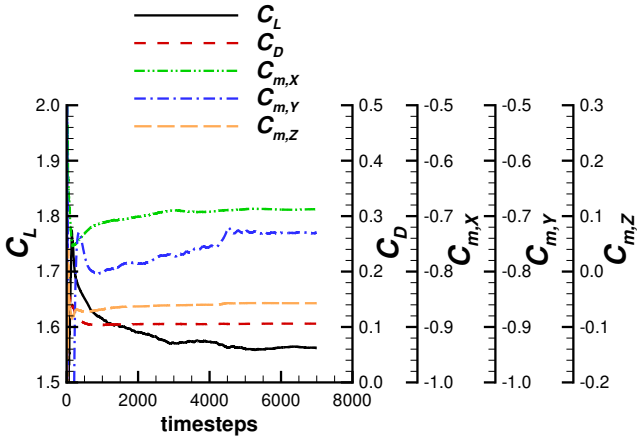

(c) Force and Moment Coefficients

Figure 25. A typical unsteady solution history for the cruise wing configuration at 128.2 KTAS, $M = 0.2246$, $\alpha = 8°$, T = 135.57 lbf, Q = 158.76 lbf-ft, USM3D SA QCR.

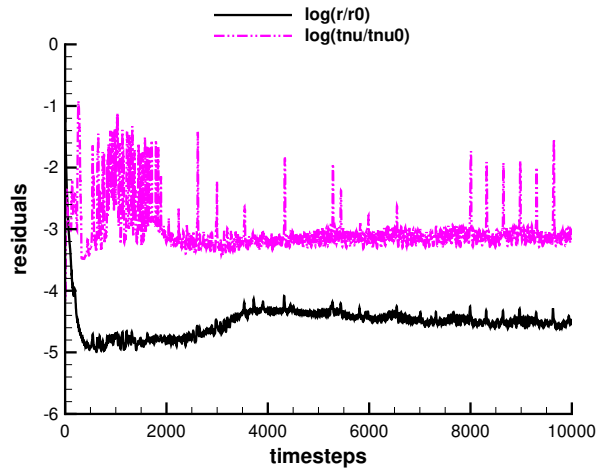

(a) Residuals

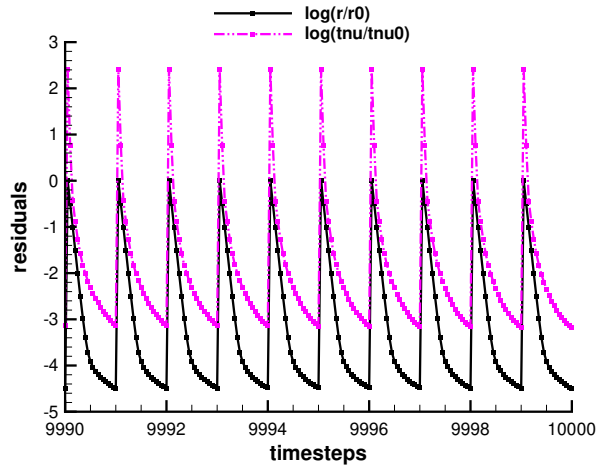

(b) Subiteration Residuals

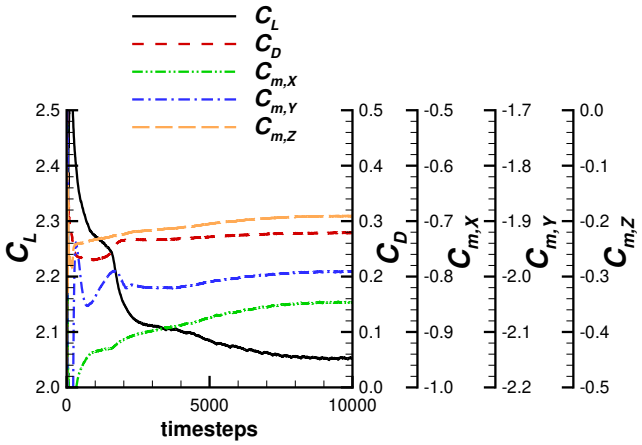

(c) Force and Moment Coefficients

Figure 26. A typical unsteady solution history for the cruise wing configuration at 128.2 KTAS, $M = 0.2246$, $\alpha = 16°$, T = 230.09 lbf, Q = 279.87 lbf-ft, USM3D SA QCR.

2.12 Effect of Mesh and Solution Parameters on Force and Moment Coefficients

Some of the cruise power cases were unstable and did not converge when the X-57 database was being developed. To quickly remedy the instability, the solutions were run with a limiter turned on and with first-order boundary conditions instead of second order. At the time, the coefficients were being used to compute deltas, the change in the coefficients from unpowered to cruise power, and specifically rolling moment was of interest. Therefore, since absolute magnitudes of the force and moment coefficients were not being used directly, the authors accepted the suggested code parameters (using a limiter) to get the solutions to converge. For this document, the authors want to report the magnitude of force and moment coefficients and the benefit of cruise power on induced drag. However, since using a limiter to obtain a solution can impact drag, the authors decided to run with variations of code parameters and mesh modifications in attempt to determine the best approach for obtaining consistent results.

Several approaches were attempted to achieve converged solutions: (1) reducing the order of the boundary conditions from second order to first order and using a limiter, (2) increasing the first cell height, and (3) modifying the mesh to eliminate the t-strip on the rudder of the vertical tail. The effect of the mesh first cell height, a limiter, and the order of the boundary conditions on force and body-axis moment coefficients for 85.7 KTAS ($M = 0.136$, 2500 feet, 2250 RPM, $J = 0.8$) at $\alpha = 2^\circ$ is shown in Figure 27. Since some of the cases would not converge with the best practice approach of using second-order boundary conditions and the limiter off, this condition where both approaches could be computed was used to compare results.

Using the same mesh with $y^+_{node} = 0.5$, while changing the code parameters from second-order boundary conditions with the limiter off (yellow circles), to first-order boundary conditions and the limiter on (grey squares) had a significant impact on drag. The differences in force and moment coefficients were: 14–16% in C_D (80–83 counts), 2.5% (0.02) in C_L, and 10–16% in C_m (0.041). For this paper, the authors wanted to be able to compare drag between conditions, and therefore, two other meshing approaches were used to achieve converged solutions.

Typical aerodynamic solutions require first cell heights set for $y^+_{cell}<1$. The first mesh used for this work was made with $y^+_{cell}<< 1$. However, since these solutions did not include high-lift propellers, the first attempt to converge some of the troubled cases was to increase the first cell height by increasing $y^+_{node} = 0.5$ ($y^+_{cell} = 0.125$) to $y^+_{node} = 1.5$ ($y^+_{cell} = 0.375$). There was little difference in force and body-axis moment coefficients between $y^+_{node} = 0.5$ (yellow circles) to $y^+_{node} = 1.5$ (blue triangles). The difference in force and moment coefficients were: 1.2% in C_D (6–7 counts), 1.2% (0.003) in C_L, and 10–16% in C_m (0.013). The large percent for C_m is a result of C_m being nearly zero.

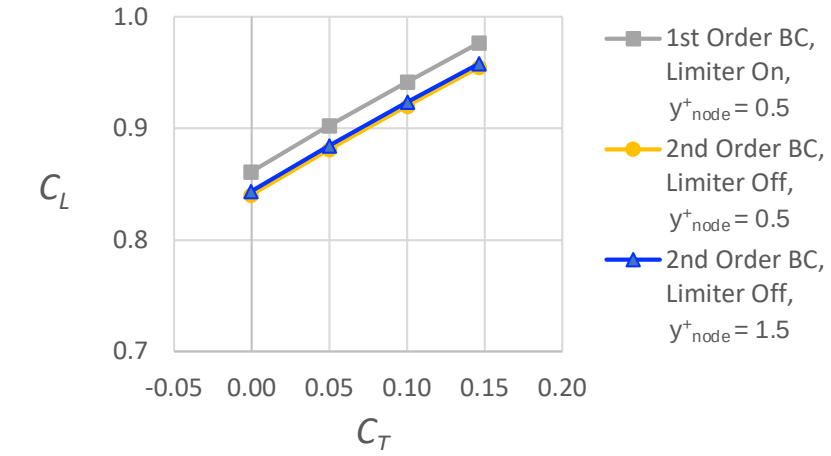

(a) Effects on Lift Coefficient

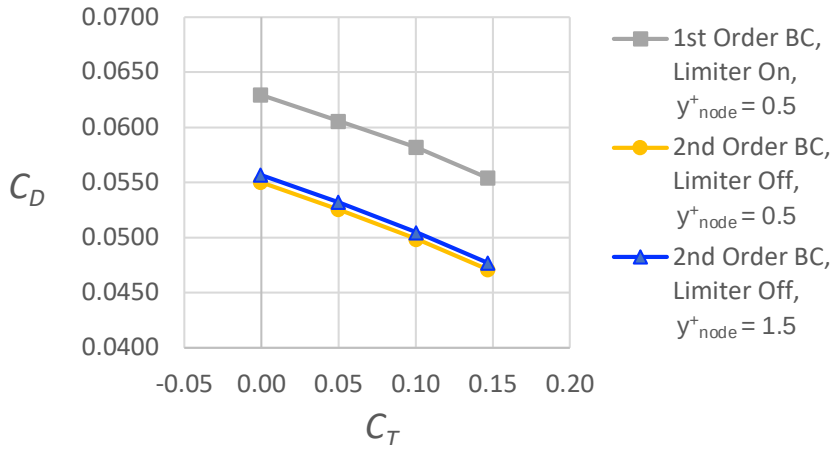

(b) Effects on Drag Coefficient

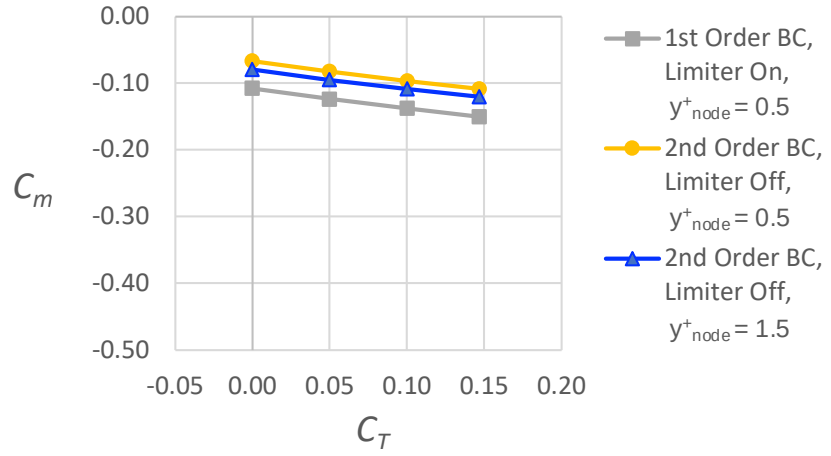

(c) Effects on Pitching Moment Coefficient

Figure 27. Effect of mesh first cell height, limiter, and order of boundary conditions on lift, drag, and pitching moment coefficients for 85.7 KTAS ($M = 0.136$, 2500 feet, 2250 RPM, $J = 0.8$), $\alpha = 2°$.

The use of the mesh with the larger first cell height had less impact on force and moment coefficients than using a limiter with first-order boundary conditions, 7 counts of drag compared to 83 counts. Approximately half of the troubled cases converged on the mesh with the larger first cell height $y^+_{node} = 0.5$ using second-order boundary conditions and no limiter. However, further investigation into the rest of the troubled cases at angles of attack of 12° and 16°, uncovered unrealistic density values near zero behind the vertical tail. Therefore, solutions were computed on a mesh without the t-strip. To quantify the impact of removing the t-strip, two cases that converged with the t-strip were repeated using the mesh without the t-strip to understand the effect of removing the tstrip. For a cruise power case, the difference in coefficients was 0.5% in C_D (5 counts), 0.2% (0.003) in C_L, and 0.9% in C_m (0.007). For an unpowered case, the difference in coefficients was 1.0% in C_D (10 counts), 0.1% (0.002) in C_L, and 0.8% in C_m (0.003). These impacts were less significant than using the limiter and lower-order boundary conditions.

Since the project closeout was scheduled for March 2024, there was no time available to run all the cases on the same mesh. Table 18 shows the mesh used for each of the converged cases.

Table 18. Mesh Used for Each Case.

Mesh	y^+_{node}	t-strip	Velocity, KTAS	α deg.	J	Case Number
1	0.5	Yes	98.6	2	1.0	78–82
1	0.5	Yes	118.4	2	1.2	100–103
1	0.5	Yes	128.2	2	1.3	110–114
1	0.5	Yes	123.8	2	1.4	154–157
1	0.5	Yes	125.8	2	1.6	164–167
1	0.5	Yes	141.6	2	1.8	174–178
2	1.5	Yes	64.3	2	0.6	11–15
2	1.5	Yes	85.7	2	0.8	16–20
2	1.5	Yes	85.7	8	0.8	21–25
2	1.5	Yes	128.2	0	1.3	120–124
2	1.5	Yes	128.2	8	1.3	115–119
3	1.5	No	85.7	12	0.8	26–30
3	1.5	No	85.7	16	0.8	31–35
3	1.5	No	128.8	16	1.3	125–129

3 Results

This section documents the aerodynamic performance computed with USM3D for the X-57 Maxwell at numerous flight conditions for the unblown wing with various cruise power settings, which was referred to as Mod III configuration within the project. Data were also computed at each flight condition without cruise power to compute a delta coefficient between cruise power on and power off solutions. The delta coefficients were computed with Equation 6 where subscript "i" was the force or moment coefficient of interest. Note that the propeller thrust force was not considered in the computation of forces and moments for the airplane configuration. The data reported in Sections 3.1–3.5 were calculated in the wind-axis system: lift coefficient (C_L), drag coefficient (C_D), rolling moment coefficient (C_l), pitching moment coefficient (C_m), and yawing moment coefficient (C_n). The data reported in Section 3.6 are the body-axis rolling moment coefficient around the x-axis ($C_{m,X}$).

The results are first presented for the effect of cruise power on drag by operating the cruise propellers in the opposite direction of the wingtip vortex in Section 3.1. Second, the impact of cruise power on lift is discussed in Section 3.2. Third, the effect of cruise power on moment coefficients (roll, pitch, yaw) calculated in the wind-axis system are discussed in Sections 3.3–3.5, respectively. Finally, a three code comparison of the effect of cruise power on body-axis rolling moment is discussed in Section 3.6. Figure 28 shows the span locations along the starboard wing from 10 inches off centerline, to 190 inches at the wingtip nacelle, in increments of 10 inches.

$$\Delta C_i = C_{i,_{powered}} - C_{i,_{unpowered}} \tag{6}$$

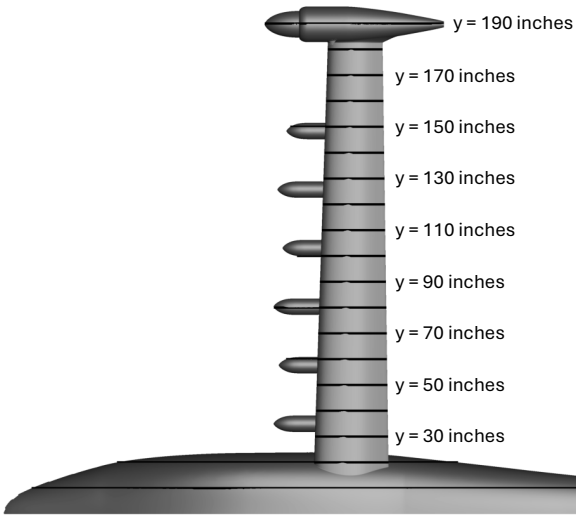

Figure 28. The spanwise locations along the starboard wing from 10 inches off centerline to 190 inches along the wingtip nacelle, in increments of 10 inches.

3.1 Effect of Cruise Power on Drag, USM3D

The motivation for rotating the X-57 Maxwell wingtip propellers in a direction opposite to that of the wingtip vortex was to reduce the penalty of induced drag from decreasing the wing span, compared to the baseline airplane. This section examines the effects of angle of attack, thrust coefficient, and airspeed on drag. The solutions were computed on a semispan mesh, but the drag reported is for the full airplane.

To begin, a few general observations are made by reviewing the drag coefficient as a function of thrust coefficient for two airspeeds, 85.7 KTAS and 128.2 KTAS, and for several angles of attack, see Figure 29. First, the drag increased with increased angle of attack and there was a significant amount of drag at $\alpha = 16°$, for both airspeeds. The second observation from Figure 29 was the drag reduction with increased thrust for $\alpha < 16°$. The drag reduction was reexamined by not only plotting at a refined scale, but also by plotting the change in drag (ΔC_D) between the cruise-powered condition and the unpowered condition, see Figure 30.

The details of the unpowered conditions ($C_T = 0$) are discussed first. The magnitude of the skin friction coefficient (C_f) contours at unpowered conditions are shown in Figure 31. The version of USM3D used for this work did not output individual components of the skin friction vector and therefore, values of skin friction in the x-axis direction that were less than zero could not be removed from view to confirm areas of flow separation. The regions of separated flow are confirmed when $C_f = 0$, but were also judged herein when the magnitude of the skin friction coefficient was constant with values of $C_f \leq 0.001$. For reference, Figure 31(d) shows the four span stations that will be discussed.

The distributions of pressure coefficient and the magnitude of the skin friction coefficient at the four spanwise stations are shown in Figures 32–33 to determine the location of flow separation for these unpowered cases. It can be difficult to judge flow separation from the C_p distributions for the full airfoil in Figure 32(a), except perhaps at $\alpha = 16°$ at a span station of y = 30 inches where the C_p is constant from approximately x = 154 inches to x = 174 inches. A smaller scale for the aft wing section in Figure 32(b) shows additional areas of constant pressure coefficient where flow separation was suspected. The magnitude of the skin friction coefficient was used to confirm the location of flow separation.

The first observation from the flow contours in Figure 31 was the increased region of very low values of C_f (dark blue contours) near the trailing edge of the wing, along the full span, with increased angle of attack. Figure 33(a) shows the C_f distributions for four span stations at four angles of attack for the upper surface of the wing, while Figure 33(b) shows data on the aft portion of the upper wing surface at a smaller y-axis scale for clarity. The location of flow separation moved upstream with increased angle of attack. At a span station of y = 30 inches, the flow was separated for $\alpha = 16°$ and $C_f \leq 0.001$ for the other angles of attack for the last few inches. At a span station of y = 85 inches, the location where $C_f < 0.001$ moved upstream from x = 172 inches for $\alpha = 8°$, to x = 165.5 inches at $\alpha = 12°$, and to x = 161.5 inches for $\alpha = 16°$. For a local chord length of 24 inches at y = 85 inches, the flow separation occurred over 8% of the local chord for $\alpha = 8°$, 31% at α

= 12°, and 48% at $\alpha = 16°$. Additionally at $\alpha = 16°$, outboard of the wingroot flow separation region, there was substantial chordwise flow separation along the entire span from the largest extent of 48% of the local chord at y = 85 inches, to 27% of the local chord at y = 160 inches. The extent of flow separation for span station y = 110 inches was from x = 164 inches to x = 173 inches, which was 37.5% of the local chord. The flow separation at a span location of y = 160 inches occurred from x = 166 inches to x = 172 inches, or 27% of the local chord.

The second observation from Figure 31(d) was the region of very low values of C_f at the wingroot for $\alpha = 16°$. The C_f data at y = 30 inches in Figure 33(a) show $C_f \leq 0.001$ from x = 154 inches to x = 174 inches for $\alpha = 16°$, which confirmed the suspicion drawn from the C_f contours that the flow was separated at the wingroot. The local chord of 28 inches at y = 30 inches had 71% flow separation and resulted in the large increased drag at unpowered conditions, compared to $\alpha < 16°$. In summary, the increased drag with increased angle of attack at a given C_T in Figure 29 was a result of the increased chordwise flow separation along the span, and the full chord flow separation that occurred at the wing root for $\alpha = 16°$.

Next, the details of the powered solutions, as compared to the unpowered data are discussed. Figure 30(a) shows the difference in drag ($\Delta C_D = C_{D,powered}$ - $C_{D,unpowered}$) as a function of thrust coefficient for $\alpha < 16°$, while Figure 30(b) shows the data for all angles of attack. The two significant results for $\alpha < 16°$ were a drag reduction ($\Delta C_D < 0$) with powered conditions ($C_T > 0$) and the drag reduction increased with thrust (Figure 30(a)). Note that the propeller thrust force was not accounted for and was independent of the reduction in drag. The drag reduction had more impact at the lower airspeed (85.7 KTAS) for a given thrust level. There was a 70 to 80 count reduction in drag at $C_T = 0.15$, and a 40 count drag reduction at 128.2 KTAS for $C_T = 0.14$. There was small effect of angle of attack on ΔC_D. The drag reduction with cruise power, compared to unpowered, varied about 10 drag counts with angle of attack at a specific thrust level for 85.7 KTAS, while the variation with angle of attack at 128.2 KTAS was smaller. This trend was reversed for $\alpha = 16°$; the drag increased about $\Delta C_D = 0.0155$ counts for 128.2 KTAS and increased about $\Delta C_D = 0.027$ counts at 85.7 KTAS, for powered cases with $C_T = 0.14$ as compared to the unpowered case.

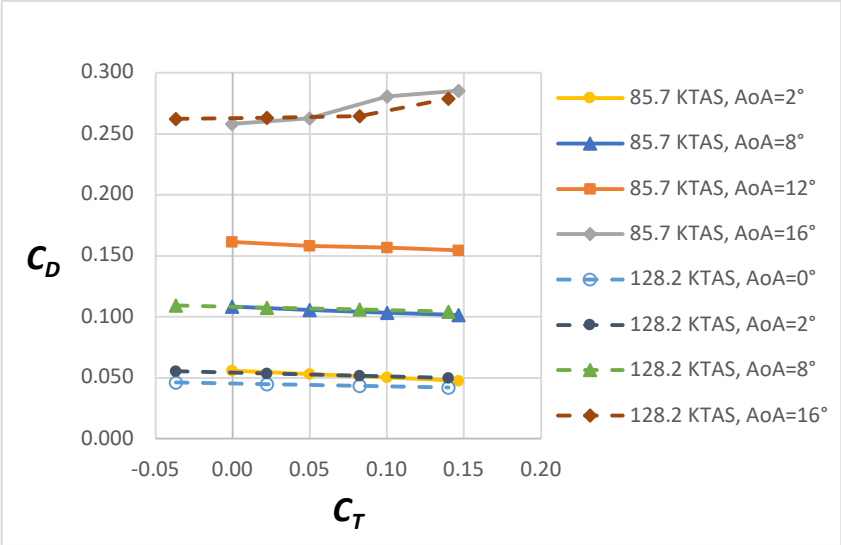

Figure 29. The effect of cruise thrust, angle of attack, and airspeed on drag for 85.7 KTAS ($M = 0.136$, 2500 feet, 2250 RPM, $J = 0.8$) and for 128.2 KTAS ($M = 0.225$, 8000 feet, 2250 RPM, $J = 1.3$).

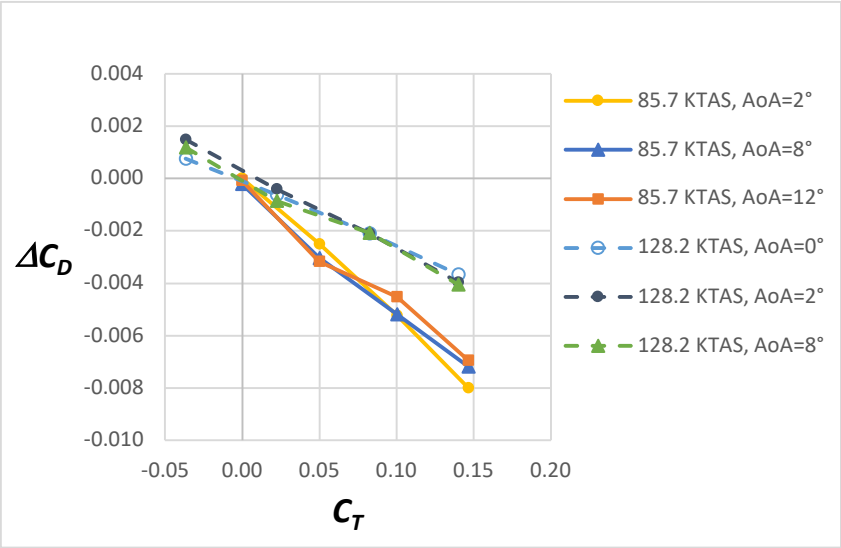

(a) ΔC_D vs C_T for $\alpha < 16°$

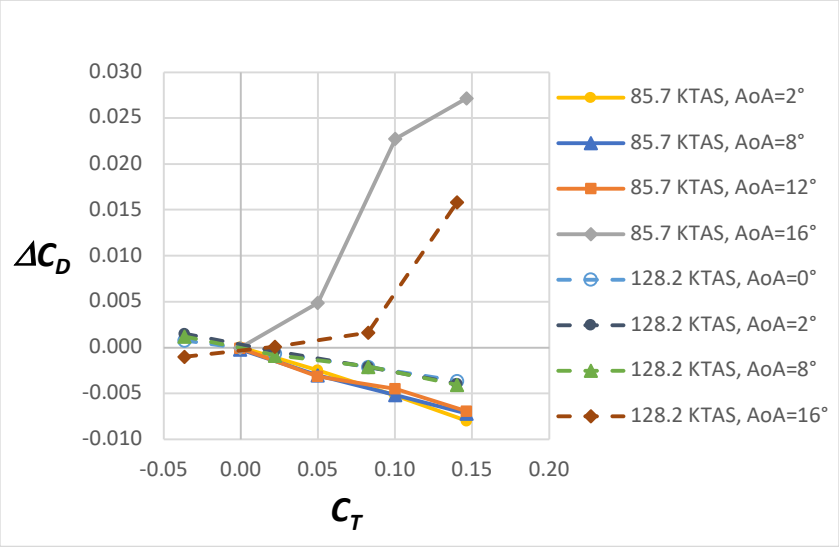

(b) ΔC_D vs C_T for all α

Figure 30. The difference in drag between cruise power and unpowered for 85.7 KTAS ($M = 0.136$, 2500 feet, 2250 RPM, $J = 0.8$) and for 128.2 KTAS ($M = 0.225$, 8000 feet, 2250 RPM, $J = 1.3$).

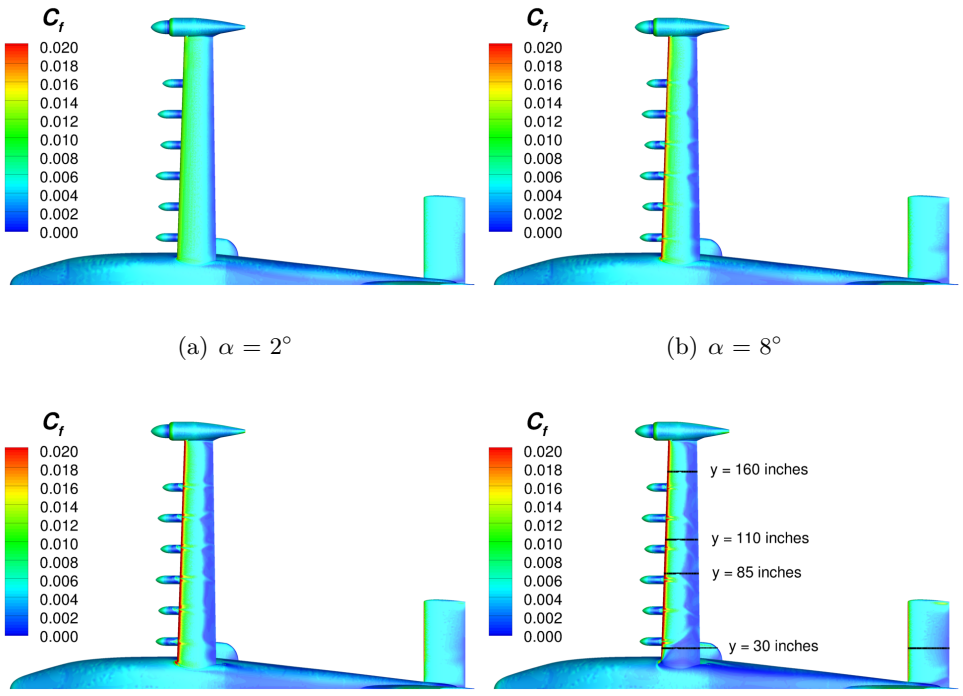

(a) $\alpha = 2°$ (b) $\alpha = 8°$

(c) $\alpha = 12°$ (d) $\alpha = 16°$

Figure 31. The effect of angle of attack on the magnitude of the skin friction coefficient contours for unpowered cruise solutions at 85.7 KTAS ($M = 0.136$) and an altitude of 2500 feet.

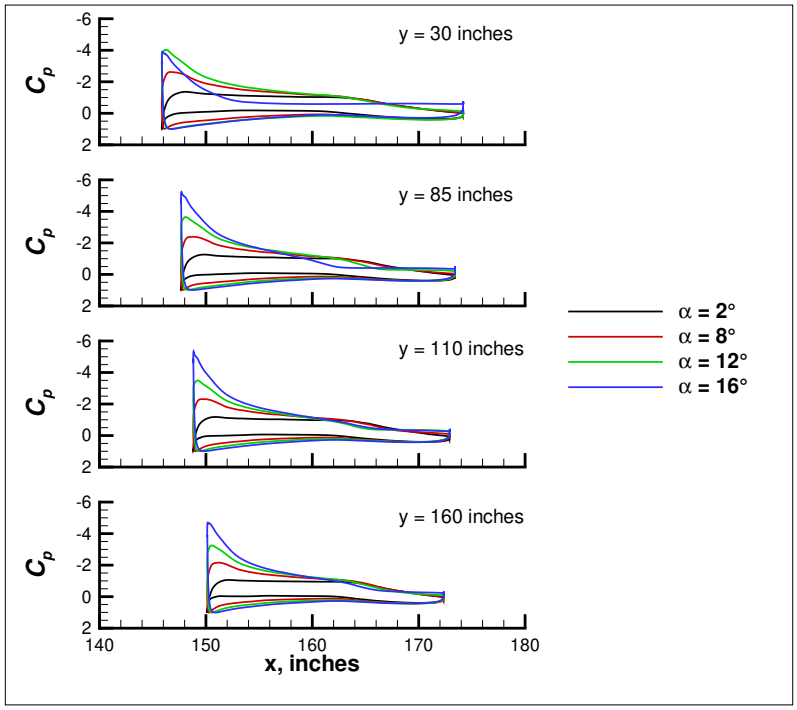

(a) C_p on the upper and lower wing surfaces

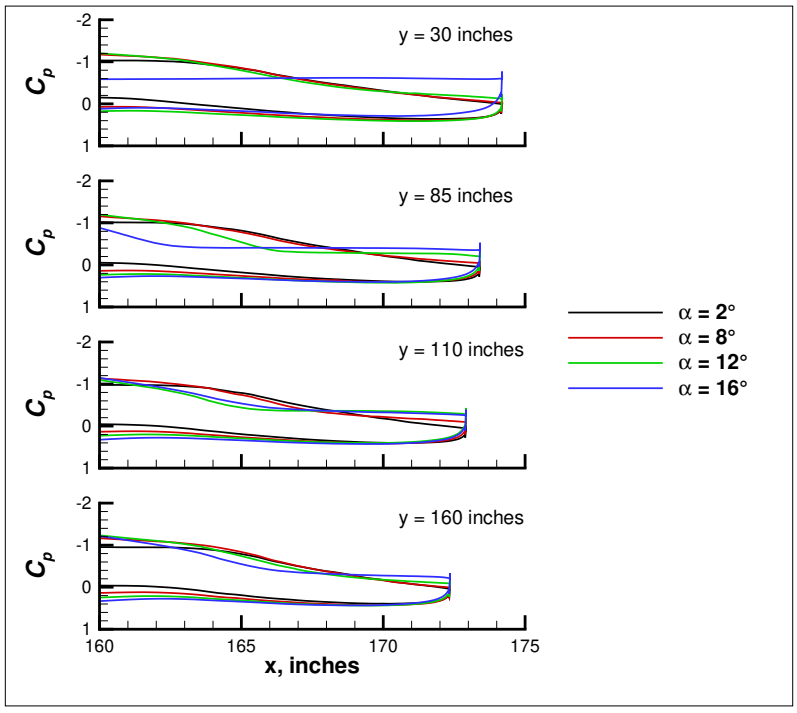

(b) C_p on the aft wing section

Figure 32. The effect of angle of attack on pressure coefficient at four spanwise locations for unpowered cruise solutions at 85.7 KTAS ($M = 0.136$) and an altitude of 2500 feet.

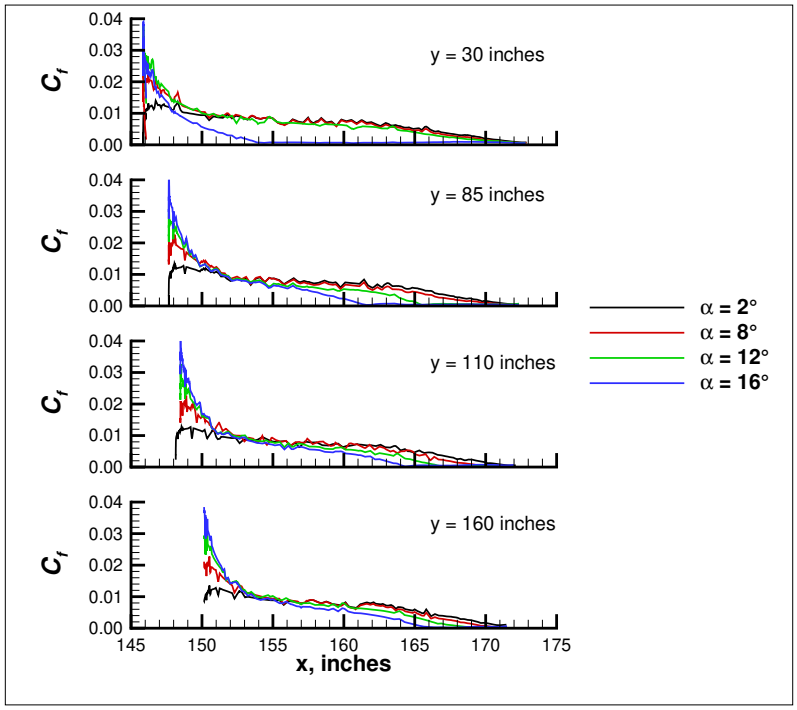

(a) C_f on the upper wing surface

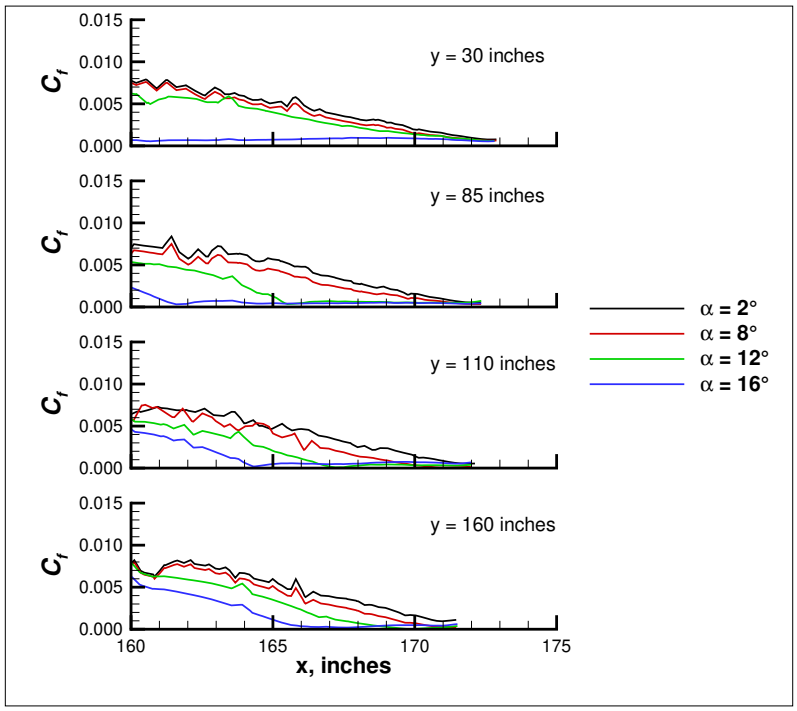

(b) C_f on the upper aft wing surface

Figure 33. The effect of angle of attack on the magnitude of the skin friction coefficient at four spanwise locations for unpowered cruise solutions at 85.7 KTAS ($M = 0.136$) and an altitude of 2500 feet.

Figures 34 to 36 show the comparison of powered to unpowered C_f contours at $\alpha = 2°$, $\alpha = 8°$, and $\alpha = 12°$, respectively. The contours are similar between powered and unpowered conditions, except in the region outboard of the last high-lift nacelle where there is a larger region of higher C_f towards the leading edge. Further comparisons between powered and unpowered results are shown for $\alpha = 2°$ at the highest thrust coefficient ($C_T = 0.15$) in Figure 37. The comparison of pressure coefficient between powered and unpowered solutions was similar for spanwise locations of $y < 140$ inches. The edge of the propeller disc was located at approximately $y = 160$ inches and the extent of the power impacted pressures at spanwise locations beyond that to approximately $y = 140$ inches (Figure 37(a)), albeit with the largest impact occurring behind the propeller disc (Figure 37(b)).

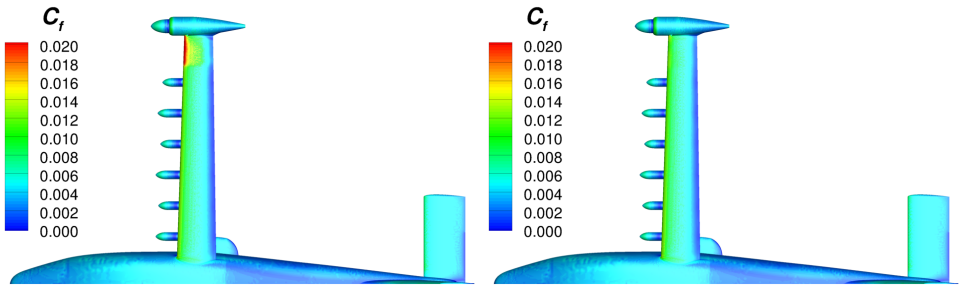

(a) Cruise Powered (b) Unpowered

Figure 34. The effect of $C_T = 0.15$ on the magnitude of the skin friction coefficient for 85.7 KTAS ($M = 0.136$), 2500 feet, 2250 RPM, $J = 0.8$, and $\alpha = 2°$.

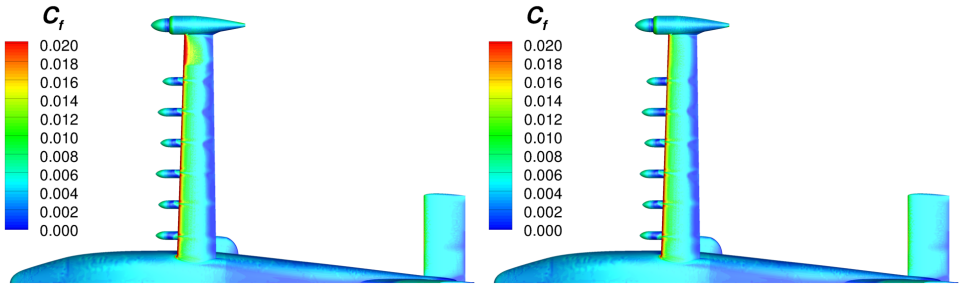

(a) Cruise Powered (b) Unpowered

Figure 35. The effect of $C_T = 0.15$ on the magnitude of the skin friction coefficient for 85.7 KTAS ($M = 0.136$), 2500 feet, 2250 RPM, $J = 0.8$, and $\alpha = 8°$.

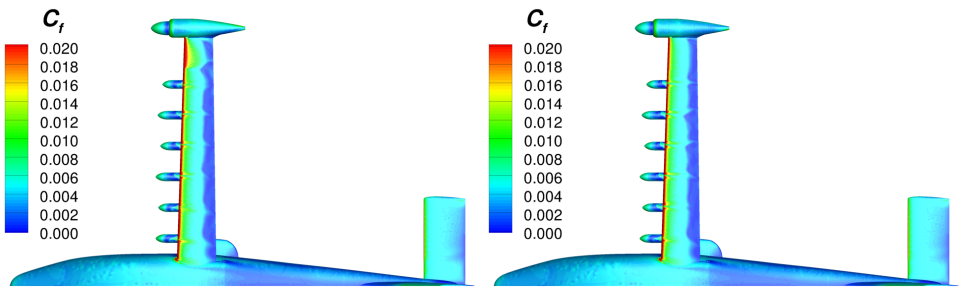

(a) Cruise Powered (b) Unpowered

Figure 36. The effect of $C_T = 0.15$ on the magnitude of the skin friction coefficient for 85.7 KTAS ($M = 0.136$), 2500 feet, 2250 RPM, $J = 0.8$, and $\alpha = 12°$.

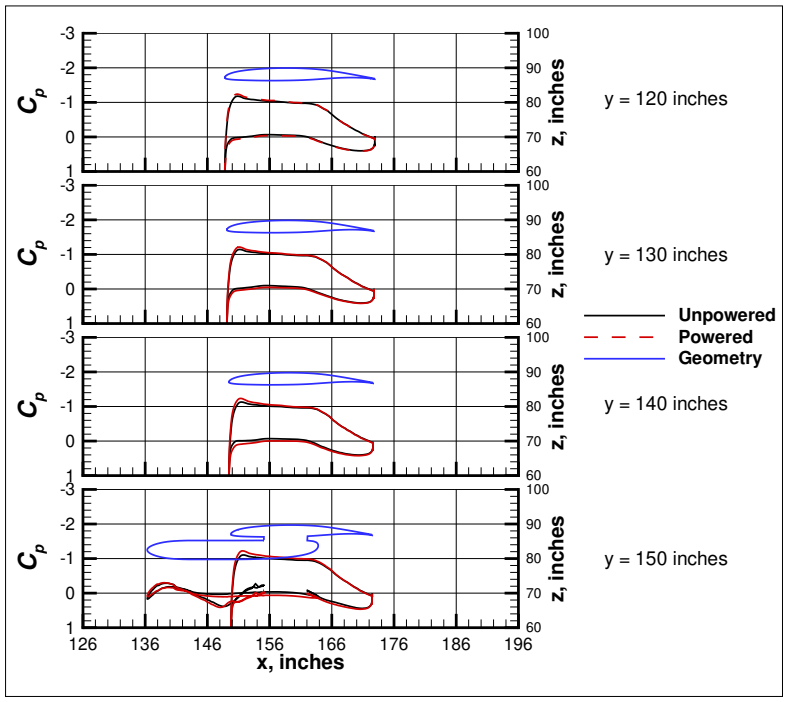

(a) y = 120 inches to y = 150 inches

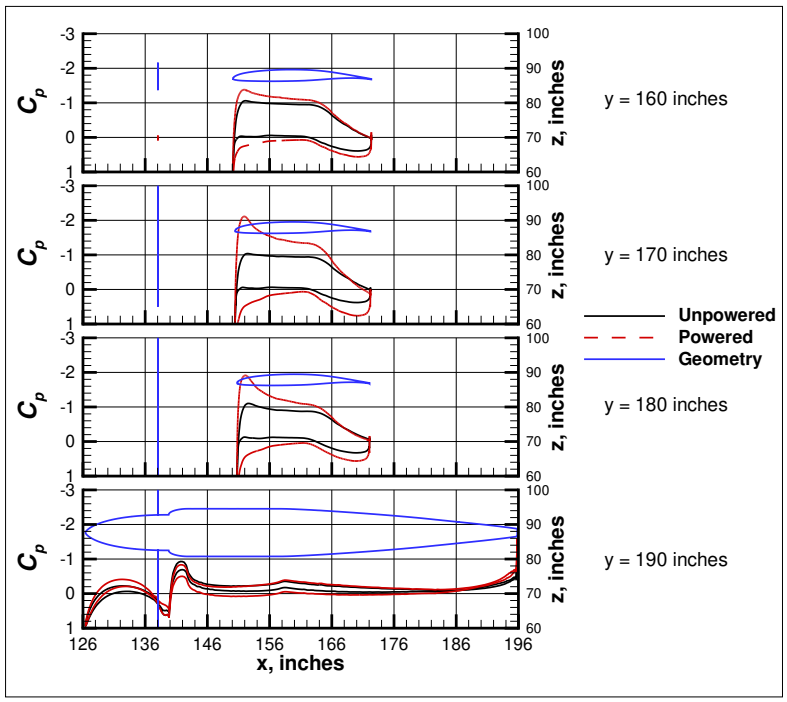

(b) y = 160 inches to y = 190 inches

Figure 37. Cases 19 and 20 $\alpha = 2°$, the effect of $C_T = 0.15$ on pressure coefficient at various spanwise locations for 85.7 KTAS ($M = 0.136$), 2500 feet, 2250 RPM, $J = 0.8$.

The increased drag with increased thrust coefficient at $\alpha = 16^\circ$ for an airspeed of 85.7 KTAS (Figure 30(b)) can be explained with the contours of the magnitude of the skin friction coefficient on the top of the airplane that are displayed in Figure 38. First, as mentioned, the USM3D code predicted significant flow separation at the wingroot and chordwise flow separation along the span at unpowered conditions, Figure 38(a). Next, there was a moderate increase in powered versus unpowered drag of approximately 50 counts ($\Delta C_D = 0.0050$) at $C_T = 0.05$, potentially from the larger region of low C_f that indicates flow separation between the outboard high-lift nacelle and the wingtip nacelle (Figure 38(b)) than at unpowered conditions (Figure 38(a)). Finally, the drag increased significantly to 227 drag counts ($\Delta C_D = 0.0227$) and 272 drag counts ($\Delta C_D = 0.0272$) as the outboard flow separation moved forward to the wing leading edge for $C_T = 0.10$ (Figure 38(c)) and $C_T = 0.15$ (Figure 38(d)), respectively.

The increased drag with increased thrust coefficient at $\alpha = 16^\circ$ for an airspeed of 128.2 KTAS was significant, but not as severe as the increased drag at 85.7 KTAS (Figure 30(b)). The C_f contours on the top of the airplane for 128.2 KTAS are shown in Figure 39. There was significant flow separation at the wingroot and chordwise flow separation along the span at all conditions. The flow contours were similar between $C_T = 0$ and $C_T = 0.02$ and the change in drag was only $\Delta C_D = 0.0001$ for $C_T = 0.02$. There was a small increase in powered versus unpowered drag of approximately 16 counts ($\Delta C_D = 0.0016$) at $C_T = 0.08$, as the region of low C_f between the outboard high-lift nacelle and the wingtip nacelle increased (Figure 39(c)) compared to unpowered conditions (Figure 39(a)). Finally, the drag increased 159 drag counts ($\Delta C_D = 0.0159$) compared to unpowered, as the flow separation outboard of the high-lift nacelles moved forward to the wing leading edge for $C_T = 0.14$ (Figure 39(d)).

The propeller flow outboard of the last high-lift nacelle caused local upwash on the wing. For both the 85.7 KTAS and 128.2 KTAS airspeeds at $\alpha = 16^\circ$ and $C_T > 0.05$, the propeller upwash put the outboard wing locally above the stall angle of attack and the flow separated from the wing upper surface. At $\alpha < 16^\circ$, the propeller flow caused local upwash on the wing and decreased the induced drag, but the flow did not separate as the local angle of attack remained below the stall angle of attack.

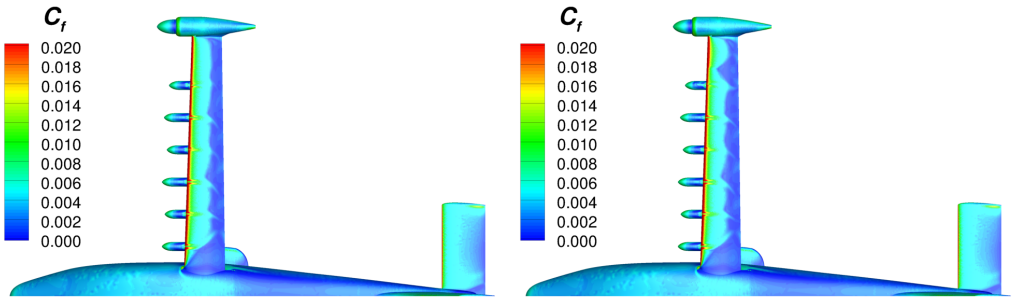

(a) T=0 lbf/prop $C_T = 0.00$

(b) T=96.8 lbf/prop $C_T = 0.05$

(c) T=194.6 lbf/prop $C_T = 0.10$

(d) T=284.5 lbf/prop $C_T = 0.15$

Figure 38. The effect of C_T on C_f for 85.7 KTAS ($M = 0.136$), 2500 feet, 2250 RPM, $J = 0.8$, and at $\alpha = 16°$.

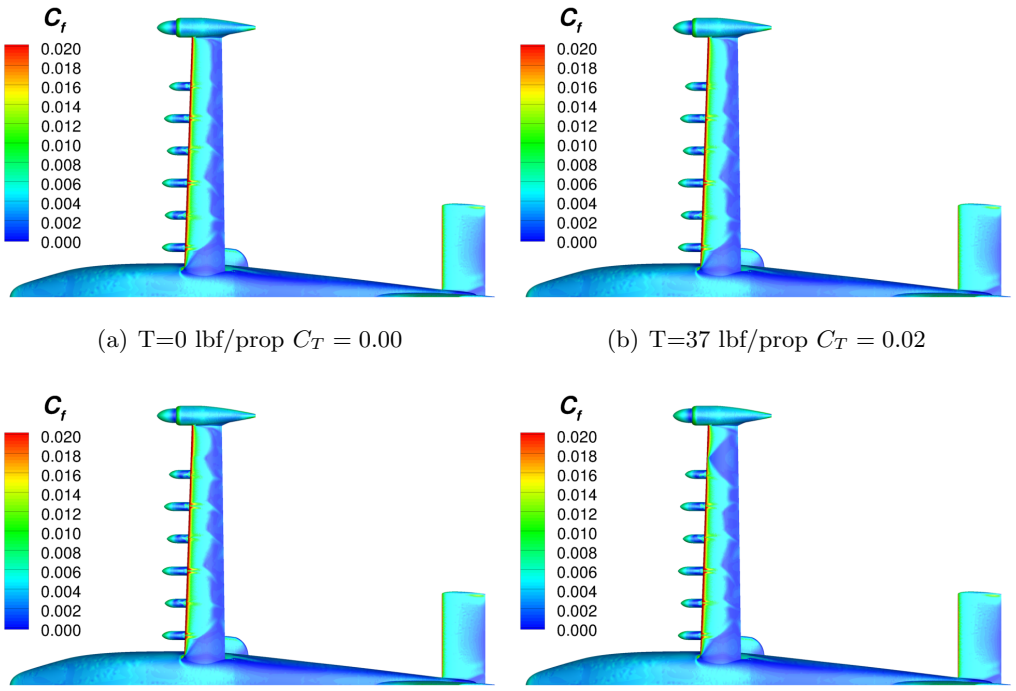

(a) T=0 lbf/prop $C_T = 0.00$

(b) T=37 lbf/prop $C_T = 0.02$

(c) T=135 lbf/prop $C_T = 0.08$

(d) T=230 lbf/prop $C_T = 0.14$

Figure 39. The effect of C_T on C_f for 128.2 KTAS ($M = 0.225$), 8000 feet, 2250 RPM, $J = 1.3$, and at $\alpha = 16°$.

The comparison of the effect of cruise power on C_D between the two lowest airspeeds, 64.3 KTAS and 85.7 KTAS, is shown in Figure 40. The drag reduction with cruise power compared to unpowered (ΔC_D) increased with increased thrust coefficient (Figure 40(b)). Additionally, there was a larger drag reduction at an airspeed of 64.3 KTAS, than for an airspeed of 85.7 KTAS. Figures 41 to 44 show comparisons of C_f contours on the outboard wing, and C_f and C_p distributions at two spanwise locations for various thrust coefficients. See Figure 28 for a diagram of the span locations. At unpowered conditions ($C_T = 0$), there was only a difference in drag of 3 counts, between the two airspeeds, with $C_D = 0.0560$ for 64.3 KTAS and $C_D = 0.0557$ for 85.7 KTAS. For the data plotted in Figure 41, there were little to no effect of airspeed on C_f or C_p.

At powered conditions of $C_T = 0.05$, there was a drag reduction of 32 counts for an airspeed of 64.3 KTAS and 25 counts for an airspeed of 85.7 KTAS (Figure 40(b)). The data plotted in Figure 42 show differences in C_f and C_p between the two airspeeds occurred outboard of the last high-lift nacelle with a slight increase in C_f (Figure 42(e)) and pressure coefficient (Figure 42(f)) for 64.3 KTAS, compared to 85.7 KTAS. Notice inboard of the last high-lift nacelle there was no difference in C_f contours between the two airspeeds, which was confirmed by comparing the C_f distribution (Figure 42(c)) and the C_p distribution (Figure 42(d)) at y = 140 inches.

At powered conditions of $C_T = 0.10$, there was a drag reduction of 66 counts for an airspeed of 64.3 KTAS and 52 counts for an airspeed of 85.7 KTAS (Figure 40(b)). Figure 43 shows larger differences in C_f and C_p between the two airspeeds for $C_T = 0.10$, than for $C_T = 0.05$. There was a larger region of elevated C_f outboard of the high-lift nacelle for 64.3 KTAS (Figure 43(a)), than for 85.74 KTAS (Figure 43(b)). The distributions at y = 170 inches confirmed higher values of C_f (Figure 43(e)) and more suction on the upper surface of the wing with lower values of C_p (Figure 43(f)) for an airspeed of 64.3 KTAS, than for 85.7 KTAS.

At powered conditions of $C_T = 0.14$, there was a drag reduction of 100 counts for an airspeed of 64.3 KTAS and 80 counts for an airspeed of 85.7 KTAS (Figure 40(b)). The data plotted in Figure 44 for $C_T = 0.14$ show even larger differences in C_f and C_p between the two airspeeds, when compared to $C_T = 0.10$. The differences occurred outboard of the last high-lift nacelle with increased C_f (Figure 44(e)) and reduced C_p (Figure 44(f)) for an airspeed of 64.3 KTAS, compared to 85.7 KTAS.

Finally, Figures 45 and 46 show the C_p and C_f distributions at y = 170 inches for both airspeeds and all thrust coefficients to demonstrate the impact of increased thrust on pressure coefficient and magnitude of the skin friction coefficient, respectively. There was a significant increased pressure differential from unpowered to maximum thrust coefficient for both airspeeds, but with larger increased pressure differentials for each thrust level for 64.3 KTAS (Figure 45(a)), than for 85.7 KTAS (Figure 45(b)). Additionally, there were significant increased C_f with increased thrust coefficient for both airspeeds, again with larger C_f values at 64.3 KTAS for each thrust level (Figure 46(a)), than at an airspeed of 85.7 KTAS (Figure 46(b)). There was increased skin friction drag from the increased velocity over the wing downstream of the propeller. However, the induced drag reduction from the propeller spun in the opposite direction as the wingtip vortex was more significant and

resulted in overall drag reduction compared to unpowered conditions. Additionally, the drag reduction was more significant at the lowest airspeed.

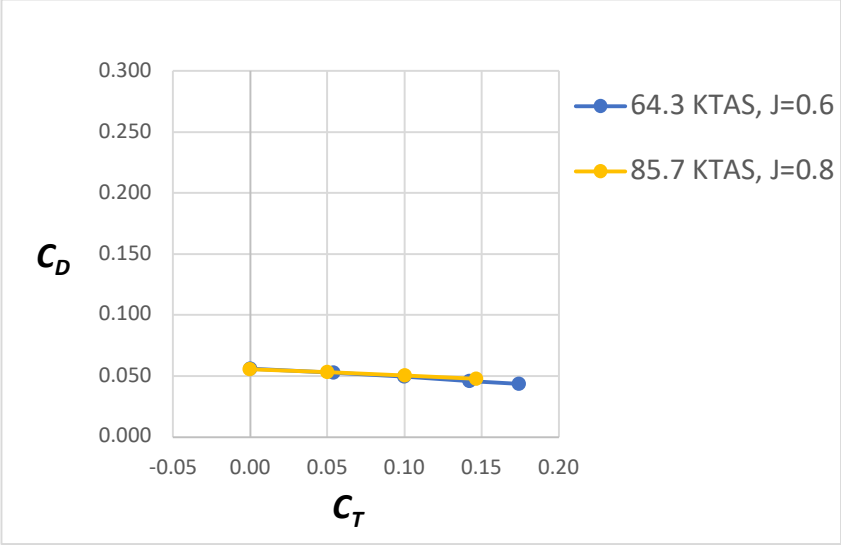

(a) C_D vs C_T

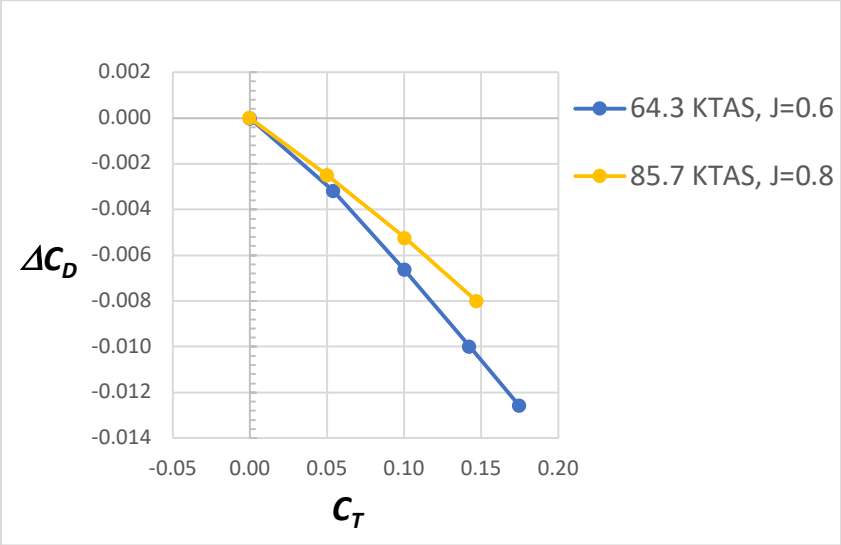

(b) ΔC_D vs C_T

Figure 40. The effect of C_T and airspeed on C_D and ΔC_D at $\alpha = 2°$, an altitude of 2500 feet, and cruise thrust at 2250 RPM.

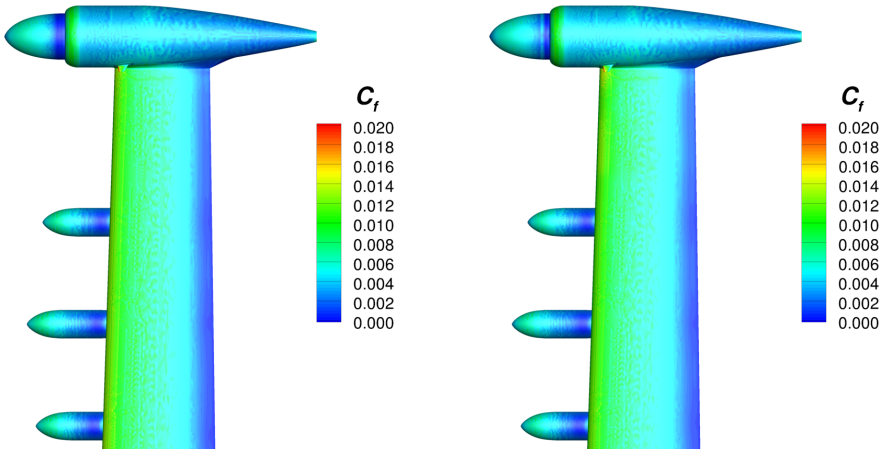

(a) 64.3 KTAS ($M = 0.102$)

(b) 85.7 KTAS ($M = 0.135$)

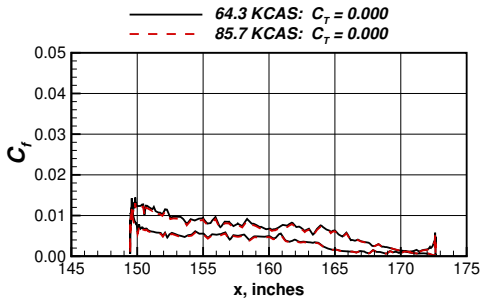

(c) C_f vs x at y = 140 inches

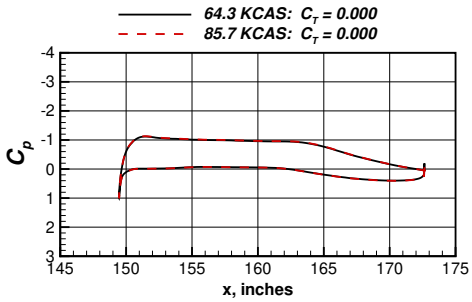

(d) C_p vs x at y = 140 inches

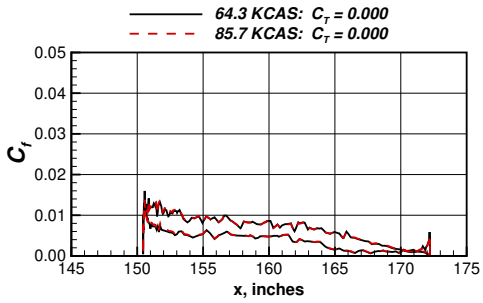

(e) C_f vs x at y = 170 inches

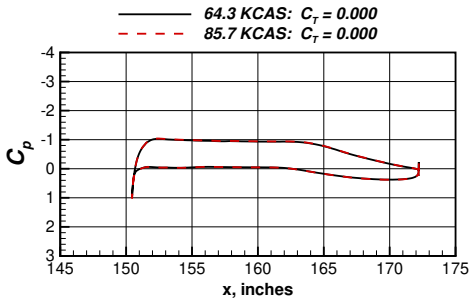

(f) C_p vs x at y = 170 inches

Figure 41. The effect of airspeed on C_f and C_p for $\alpha = 2°$ at 2500 feet and unpowered conditions (C_T=0.00).

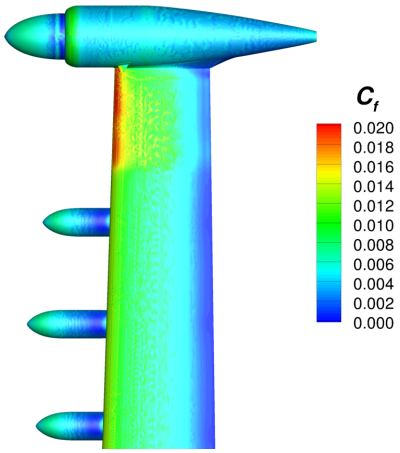

(a) 64.3 KTAS ($M = 0.102$)

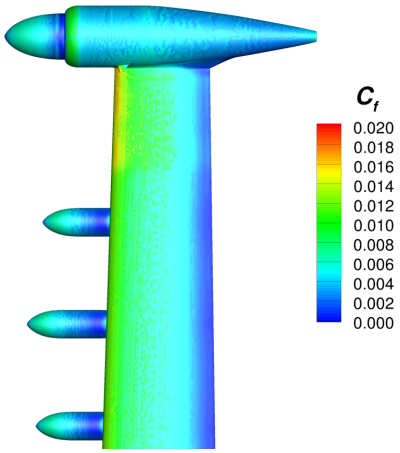

(b) 85.7 KTAS ($M = 0.135$)

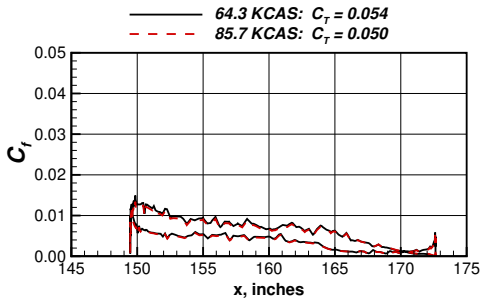

(c) C_f vs x at y = 140 inches

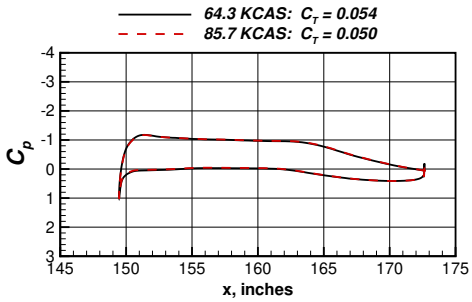

(d) C_p vs x at y = 140 inches

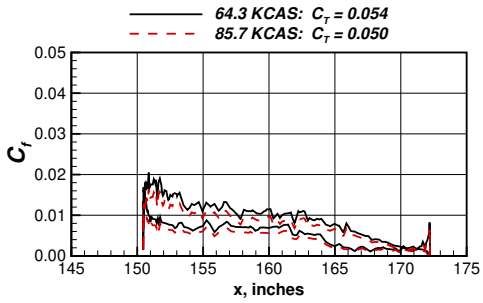

(e) C_f vs x at y = 170 inches

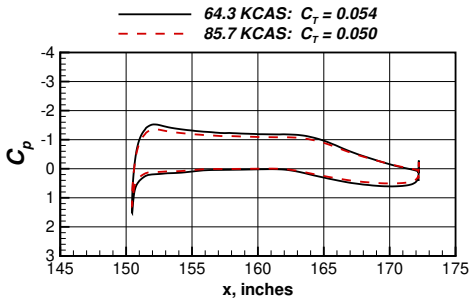

(f) C_p vs x at y = 170 inches

Figure 42. The effect of airspeed on C_f and C_p for $\alpha = 2°$ at 2500 feet with C_T=0.05.

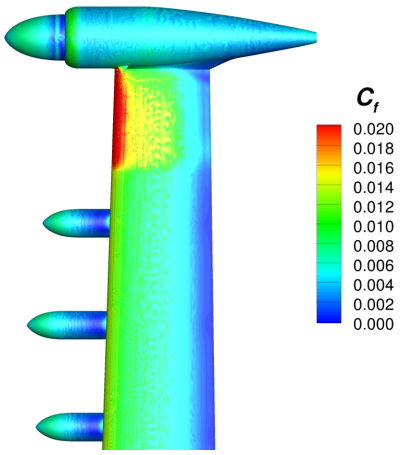

(a) 64.3 KTAS ($M = 0.102$)

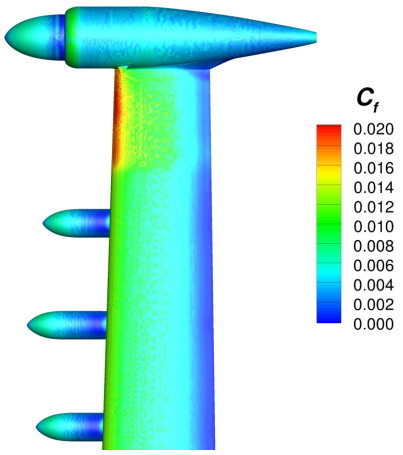

(b) 85.7 KTAS ($M = 0.135$)

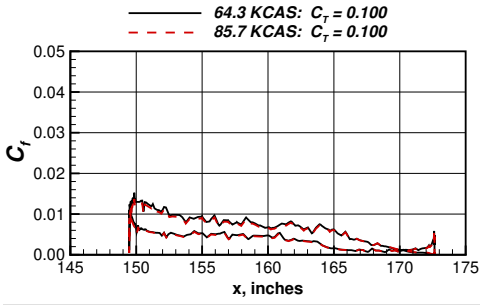

(c) C_f vs x at y = 140 inches

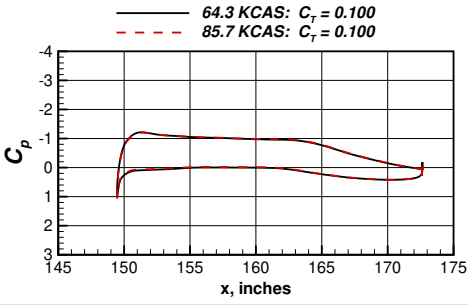

(d) C_p vs x at y = 140 inches

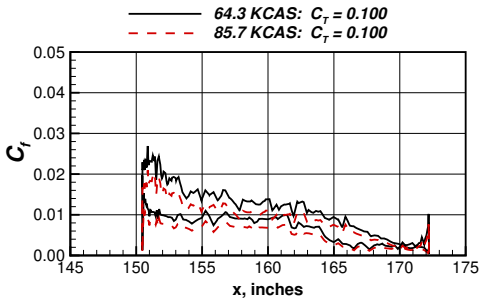

(e) C_f vs x at y = 170 inches

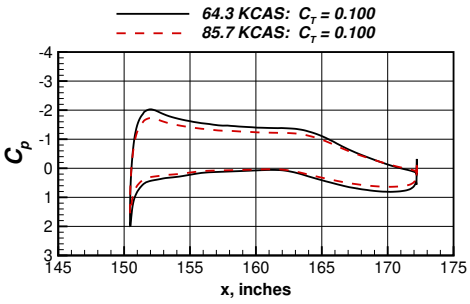

(f) C_p vs x at y = 170 inches

Figure 43. The effect of airspeed on C_f and C_p for $\alpha = 2°$ at 2500 feet with C_T=0.10.

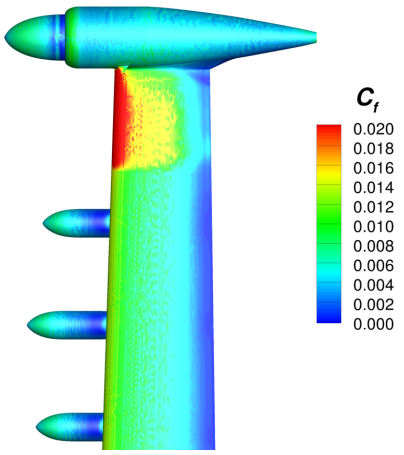

(a) 64.3 KTAS ($M = 0.102$)

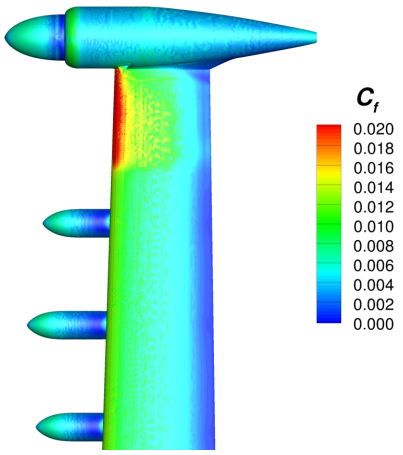

(b) 85.7 KTAS ($M = 0.135$)

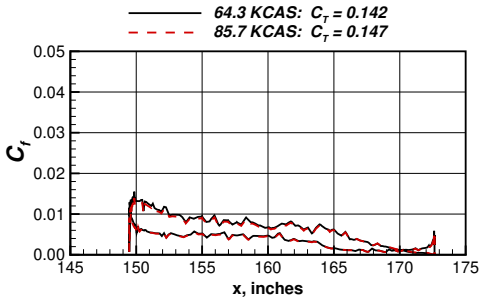

(c) C_f vs x at y = 140 inches

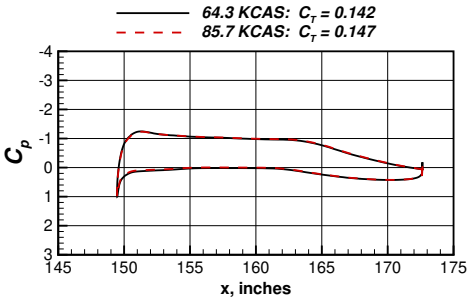

(d) C_p vs x at y = 140 inches

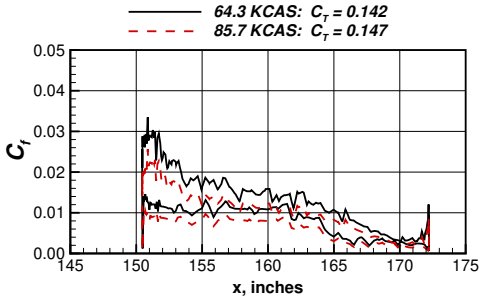

(e) C_f vs x at y = 170 inches

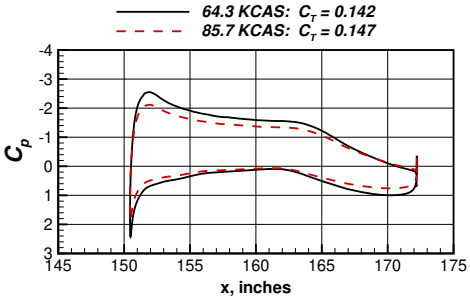

(f) C_p vs x at y = 170 inches

Figure 44. The effect of airspeed on C_f and C_p for $\alpha = 2°$ at 2500 feet with C_T=0.14.

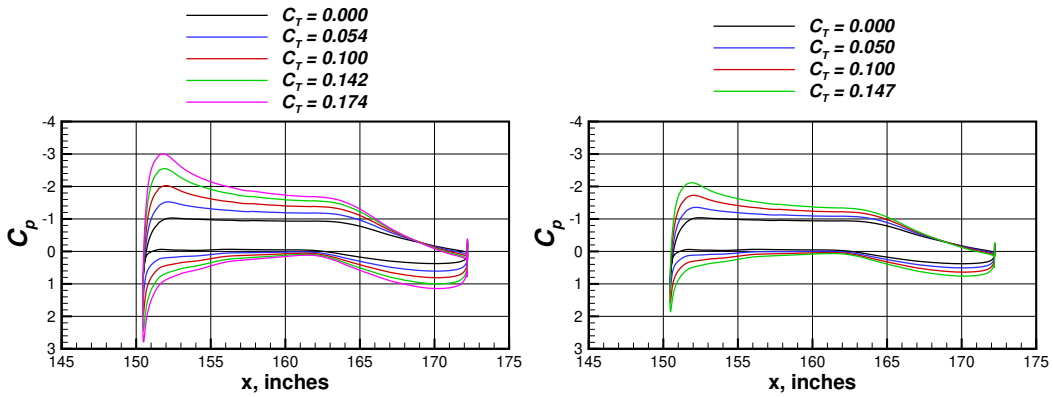

(a) 64.3 KTAS (b) 85.7 KTAS

Figure 45. The effect of C_T on C_p distributions at a span location of y = 170 inches for $\alpha = 2°$, an altitude of 2500 feet, and cruise thrust at 2250 RPM.

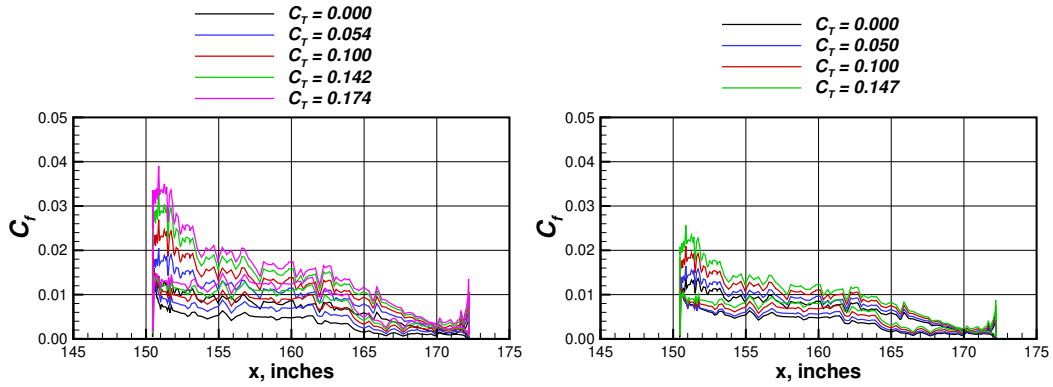

(a) 64.3 KTAS (b) 85.7 KTAS

Figure 46. The effect of C_T on C_f distributions at a span location of y = 170 inches for $\alpha = 2°$, an altitude of 2500 feet, and cruise thrust at 2250 RPM.

3.2 Effect of Cruise Power on Lift, USM3D

The data reported in this section are for the full airplane lift coefficient. Figure 47 presents the lift coefficient as a function of thrust coefficient for two airspeeds, 85.7 KTAS and 128.2 KTAS, and for several angles of attack. The two significant results were the large increases in lift coefficient with increased angle of attack, and the modest increases in lift coefficient with increased thrust coefficient. The effect of angle of attack on sectional lift coefficient (c_l) on the wing for 85.7 KTAS is shown in Figure 48.

First, at unpowered conditions shown in Figure 48(a), the sectional lift coefficient across the wing span increased by approximately 0.5 from $\alpha = 2^\circ$ to $\alpha = 8^\circ$. The smaller increment in angle of attack from $\alpha = 8^\circ$ to $\alpha = 12^\circ$ resulted in a smaller increment of increased sectional lift coefficient, with a smaller increment for $y >$ 100 inches, than for $y < 100$ inches. For $\alpha = 16^\circ$ compared to $\alpha = 12^\circ$, there was a reduction in sectional lift coefficient for $y \leq 40$ inches where the C_f contours shown in Figure 38(a) indicated flow separation that extended to the wing leading edge, but there was a slight increase in sectional lift coefficient for $y > 40$ inches. At powered conditions with $C_T = 0.15$ (Figure 48(b)), the sectional lift coefficient across the wing span is similar to the unpowered wing for $\alpha < 16^\circ$, however, there was an additional increment of increased sectional lift coefficient from the propeller wake increasing the velocity over the wing for $y > 150$ inches. At powered conditions of $C_T = 0.15$ for $\alpha = 16^\circ$, the same inboard separation and reduced sectional lift coefficient was present like the unpowered condition. However, in addition, the upwash from the propeller wake increased the local angle of attack which resulted in local stall (Figure 38(d)) and loss of sectional lift coefficient for $y > 150$ inches.

Second, the lift increased with increased thrust for both airspeeds at $\alpha < 16^\circ$ (Figure 47), but remained approximately constant for $\alpha = 16^\circ$ due to flow separation on the outboard wing that was previously discussed in Section 3.1. The increased lift with increased thrust will be discussed further with the next figure.

The change in lift (ΔC_L) between the cruise-powered condition and the unpowered condition ($\Delta C_L = C_{L,powered}$ - $C_{L,unpowered}$) is shown in Figure 49. First note that cruise power increased lift ($\Delta C_L > 0$) for all $\alpha < 16^\circ$. There was a maximum increase of $\Delta C_L = 0.157$ in lift due to cruise power at 85.7 KTAS and an angle of attack of 12°, and $\Delta C_L = 0.123$ for angles of attack of 2° and 8°. At 128.2 KTAS the impact on lift was $\Delta C_L = 0.055$ for all angles of attack less than 16°. The wingtip cruise power added an increment to lift by increasing the velocity above the wing in the region downstream of the propeller plane, which reduced the pressure on the upper surface of the wing between the outboard nacelle and the wingtip nacelle. An example of the reduction in pressure (increased suction) on the wing upper surface with cruise power, as compared to unpowered cruise, was shown in Figure 37 for 85.7 KTAS at $\alpha = 2^\circ$ with $C_T = 0.15$, which had an increase in lift of $\Delta C_L = 0.11$ due to cruise power. Figure 50 shows another example of increased lift from cruise power in the spanwise loading (sectional lift coefficient) for an airspeed of 85.7 KTAS at α = 8° with $C_T = 0.15$. This figure also shows no effect of power on the sectional lift coefficient on the stabilator and fuselage, but displays that the increased lift from power was mostly localized outboard of the last high-lift nacelle, or y > 150 inches.

Figure 51 shows a comparison of C_p at various span locations on the outboard region of the wing for 85.7 KTAS and $\alpha = 8°$ for $C_T = 0.15$, where the increased lift from cruise power was $\Delta C_L = 0.12$. Each subfigure shows the wing airfoil at the span location, while Figure 51(f) also shows the VG location between 151 inches < x < 153 inches on the wingtip nacelle. The pressure is reduced significantly on the upper surface of the wing directly behind the propeller, compared to the unpowered pressures.

The second point for the lift data shown in Figure 49 was that the increased lift from cruise power was larger at 85.7 KTAS, than at an airspeed of 128.2 KTAS. One might consider the increased lift as a result of the incremental increase in propeller-wake velocity above the freestream flow velocity. However, at a specific thrust level, there was a larger difference in velocity between the propeller-wake airstream and the freestream flow for 85.7 KTAS, and thus a larger increase in lift was realized than at 128.2 KTAS.

The final note of interest for the lift data shown in Figure 49 was the increased lift coefficient with increased thrust coefficient. At a particular angle of attack, the ΔC_L increased with increased thrust coefficient due to the increased velocity of the flow behind the propeller, which reduced the pressures on the wing. Figure 52 shows the increased sectional lift coefficient with increased thrust coefficient for angles of attack $\alpha = 2°$, $8°$ and $12°$. The largest increase in sectional lift coefficient due to power was at $\alpha = 12°$ (Figure 52(c)), as would be expected from the data shown in Figure 49.

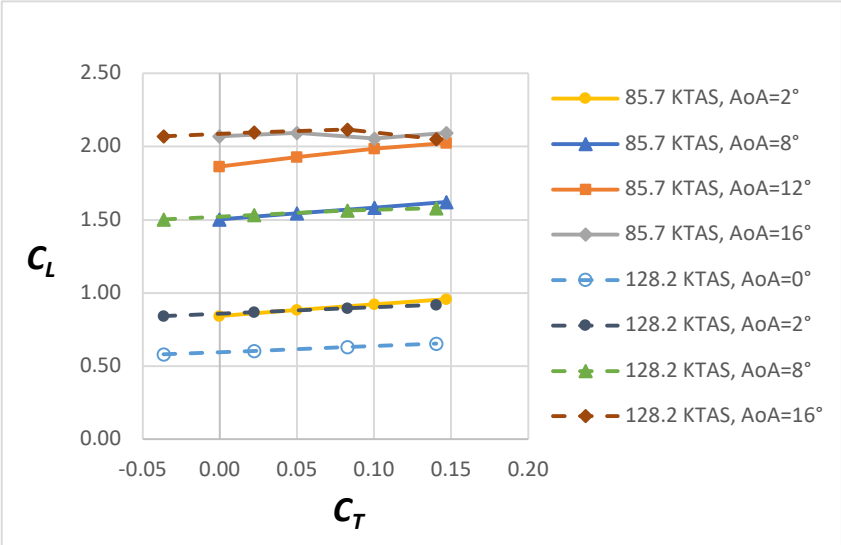

Figure 47. The effect of thrust, angle of attack, and airspeed on lift for 85.7 KTAS ($M = 0.136$, 2500 feet, 2250 RPM, $J = 0.8$) and for 128.2 KTAS ($M = 0.225$, 8000 feet, 2250 RPM, $J = 1.3$).

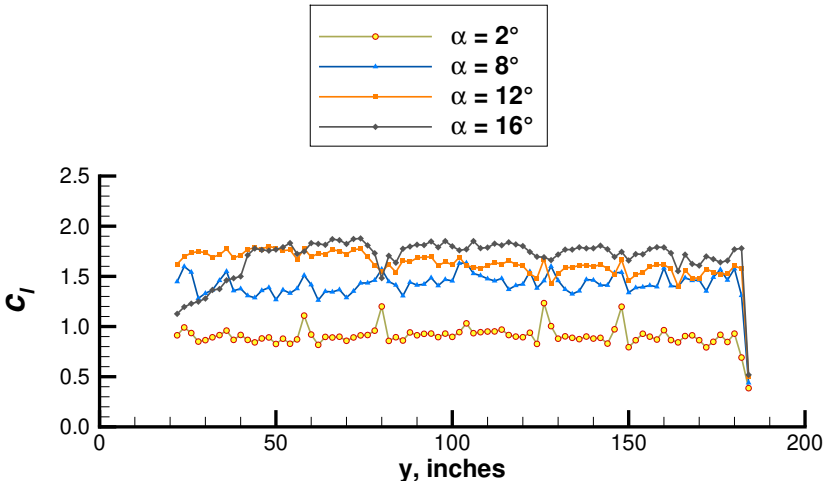

(a) $C_T = 0.00$

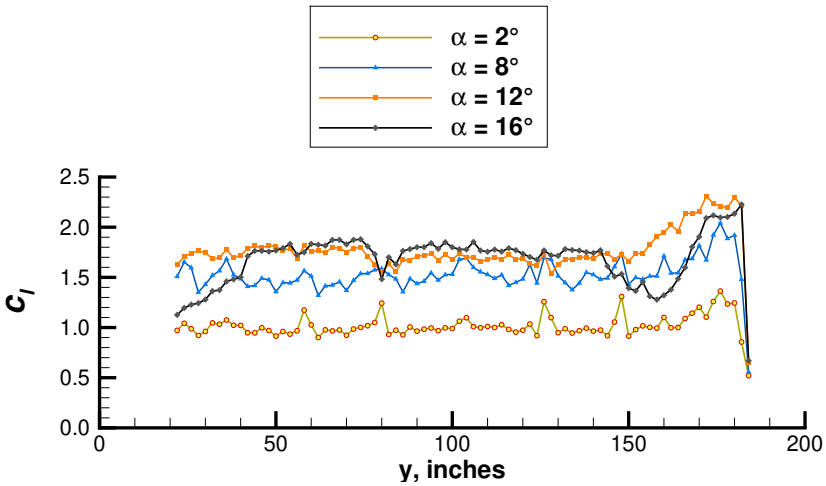

(b) $C_T = 0.15$

Figure 48. The effect of angle of attack on sectional lift coefficient for 85.7 KTAS ($M = 0.136$, 2500 feet, 2250 RPM, $J = 0.8$).

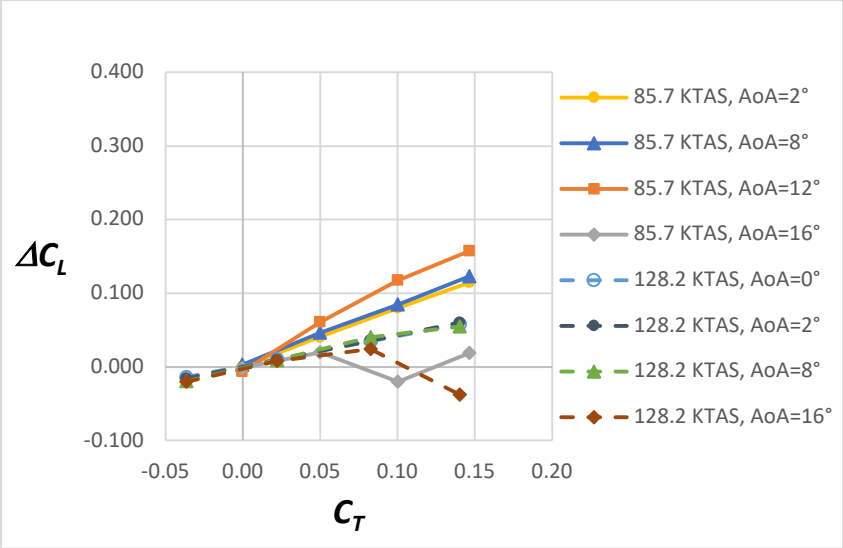

Figure 49. The effect of thrust, angle of attack, and airspeed on change in lift from unpowered to cruise powered, for 85.7 KTAS (M = 0.136, 2500 feet, 2250 RPM, J = 0.8) and for 128.2 KTAS (M = 0.225, 8000 feet, 2250 RPM, J = 1.3).

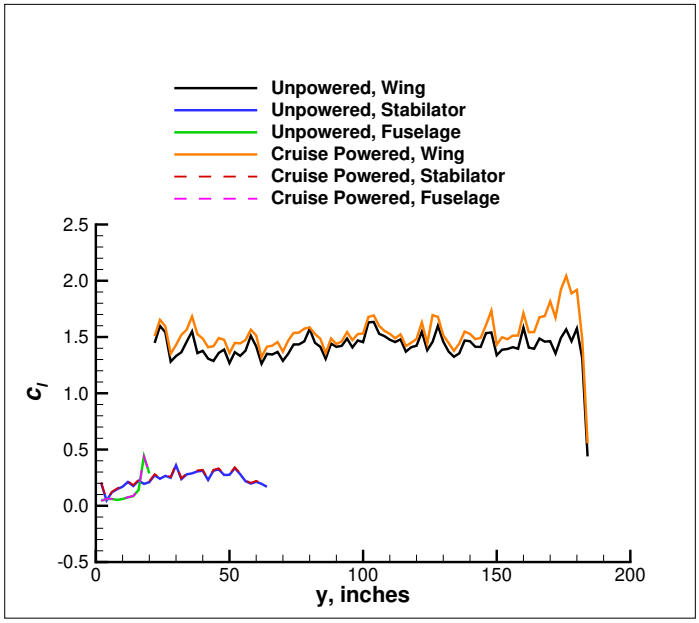

Figure 50. The sectional lift coefficient for cruise powered conditions (C_T = 0.15, 2250 RPM, J = 0.8) and unpowered conditions for an airspeed of 85.7 KTAS (M = 0.136, 2500 feet) at $\alpha = 8°$.

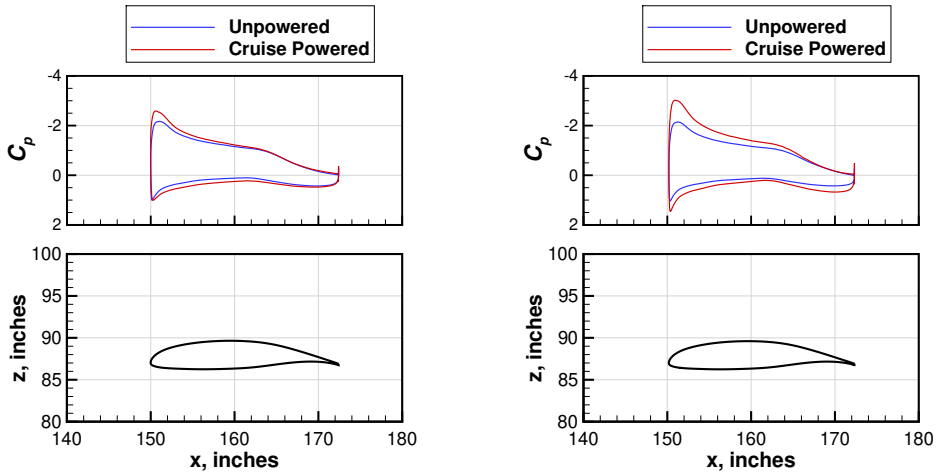

(a) y = 156 inches

(b) y = 162 inches

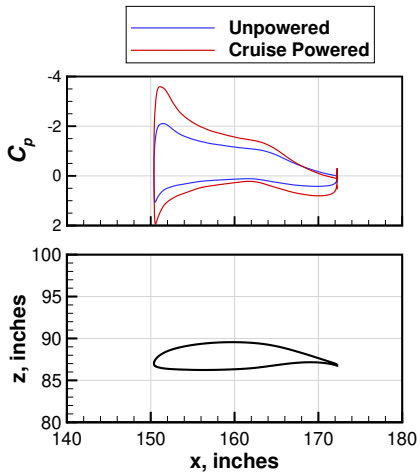

(c) y = 168 inches

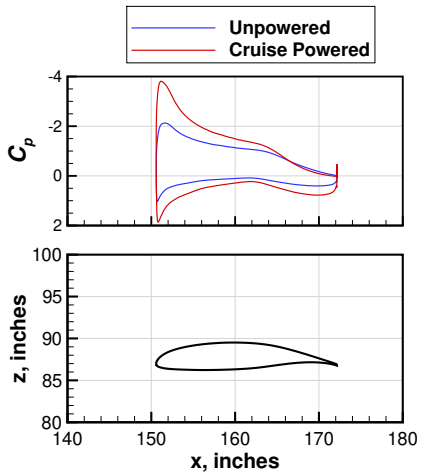

(d) y = 174 inches

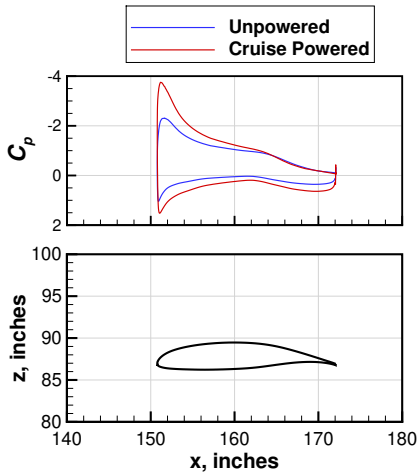

(e) y = 180 inches

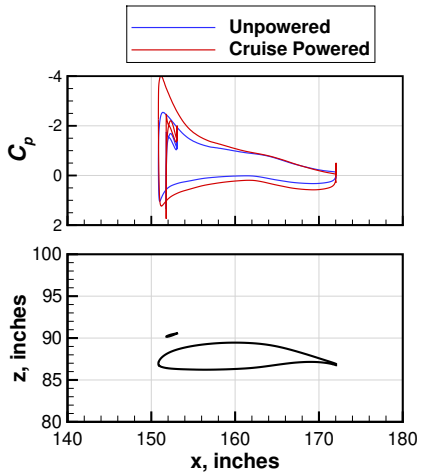

(f) y = 182 inches

Figure 51. Comparisons of C_p at various span locations for 85.7 KTAS at an altitude of 2500 feet, $\alpha = 8°$, and a cruise thrust at $C_T = 0.15$, 2250 RPM, and $J = 0.8$.

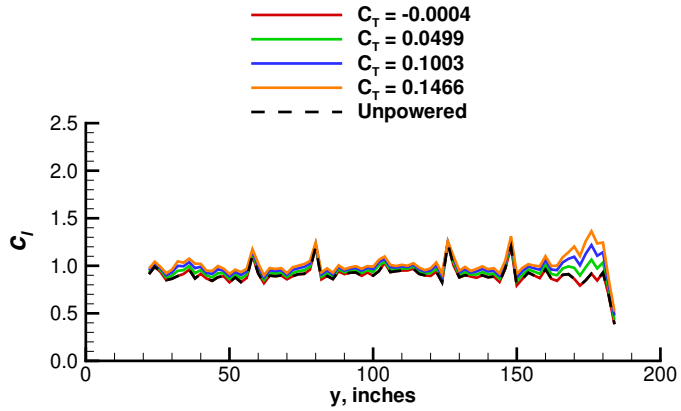

(a) $\alpha = 2^\circ$

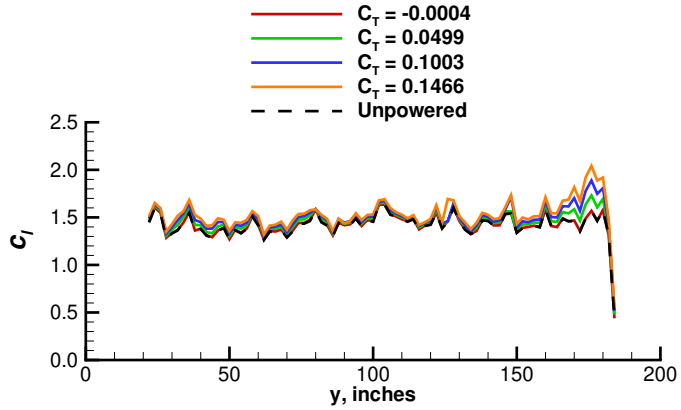

(b) $\alpha = 8^\circ$

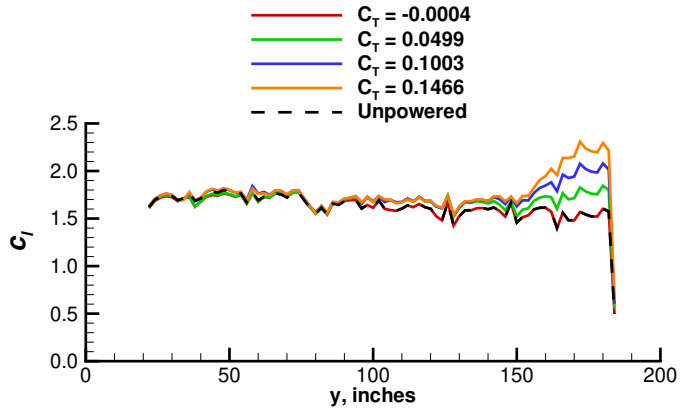

(c) $\alpha = 12^\circ$

Figure 52. The effect of thrust coefficient on sectional lift coefficient for various angles of attack for 85.7 KTAS at an altitude of 2500 feet, and cruise thrust at 2250 RPM and $J = 0.8$.

3.3 Effect of Cruise Power on Rolling Moment, USM3D

The effects of cruise power on rolling moment coefficient (C_l) and delta rolling moment coefficient (ΔC_l) for two airspeeds, 85.7 KTAS and 128.2 KTAS, and for several angles of attack are shown in Figure 53. It is important to point out that the USM3D data were computed on a semispan mesh and the data reported in this section are semispan rolling moment coefficient. The delta rolling moment was not computed on a full span configuration with one cruise propeller operating and one unpowered, but was computed as the difference between power and unpowered cases using a semispan mesh. Therefore, the unpowered rolling moment coefficients in Figure 53(a) are not zero because the starboard forces and moments were not balanced by the port side.

The increased negative semispan rolling moment with increased thrust for $\alpha < 16^\circ$ was due to the increased lift from cruise thrust that was discussed in Section 3.2. It was shown that at $\alpha = 16^\circ$ there was flow separation between the last high-lift nacelle and the wingtip nacelle and that was the reason for the increased positive rolling moment for $C_T = 0.10$ at 85.7 KTAS and for $C_T = 0.14$ at 128.2 KTAS. The effect of cruise thrust on rolling moment was larger at 85.7 KTAS than at 128.2 KTAS, Figure 53(b). The rolling moment was most impacted by cruise thrust at $\alpha = 12^\circ$ at the lower airspeed (85.7 KTAS). These data were important to understand the effect of differential cruise thrust on rolling moment to add the effects in the X-57 Maxwell flight simulator.

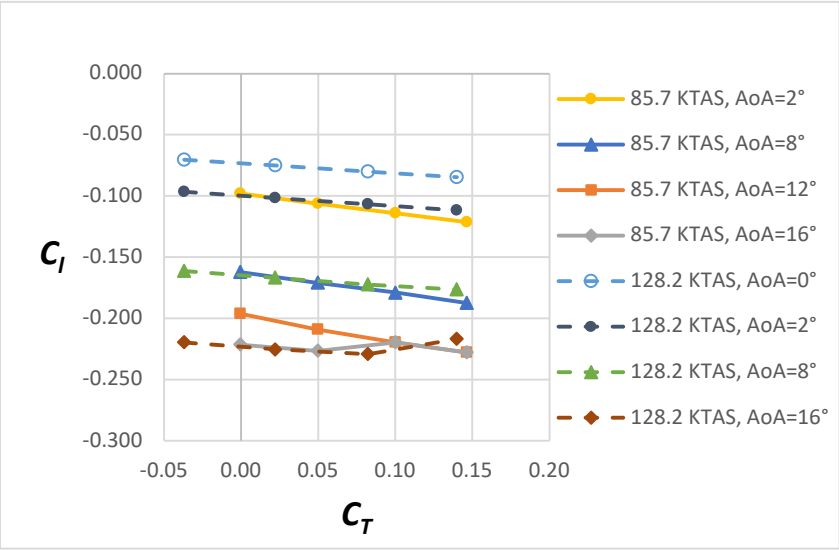

(a) Semispan Rolling Moment Coefficient

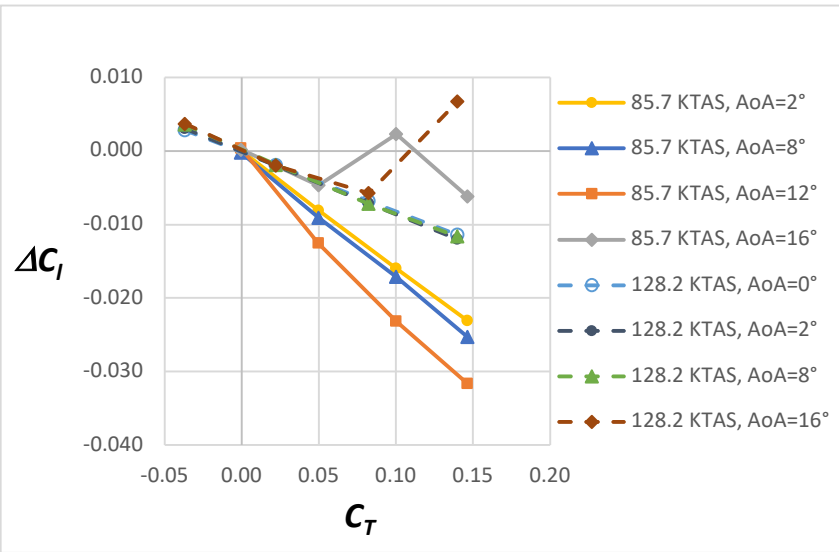

(b) ΔC_l vs C_T

Figure 53. The effect of cruise power on rolling moment for 85.7 KTAS ($M = 0.136$, 2500 feet, 2250 RPM, $J = 0.8$) and for 128.2 KTAS ($M = 0.225$, 8000 feet, 2250 RPM, $J = 1.3$) at angles of attack from $\alpha = 0°$ to $\alpha = 16°$.

3.4 Effect of Cruise Power on Pitching Moment, USM3D

The effects of cruise power on pitching moment coefficient (C_m) and delta pitching moment coefficient (ΔC_m) for two airspeeds, 85.7 KTAS and 128.2 KTAS, and for several angles of attack are shown in Figure 54. Similar to Section 3.3, the data reported in this section are semispan pitching moment coefficients.

There was a slight increase in negative pitching moment coefficient with increased thrust coefficient for both airspeeds at angles of attack less than 16° (Figure 54(a)). The maximum increase in negative pitching moment due to cruise thrust was only ΔC_m = -0.036 at 85.7 KTAS and $\alpha = 12°$. The change in slope of ΔC_m versus C_T occurred at $\alpha = 16°$ for 85.7 KTAS at $C_T = 0.10$, and for 128.2 KTAS at $C_T = 0.14$ due to flow separation on the wing between the outboard most high-lift nacelle and the wingtip nacelle that was not present in the unpowered case. The positive ΔC_m for 128.2 KTAS at $\alpha = 16°$ and $C_T = 0.14$ occurred from flow separation, but it was only a 0.2% increase in pitching moment coefficient compared to the unpowered C_m.

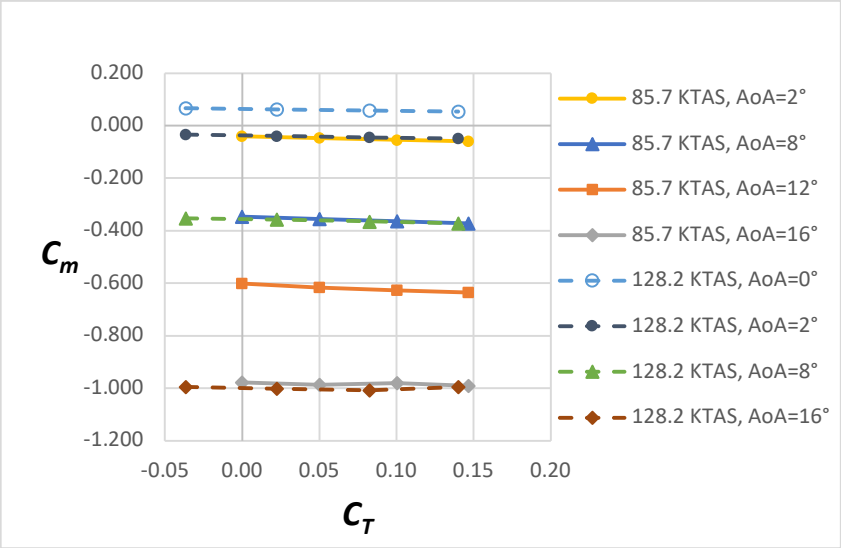

(a) Semispan Pitching Moment Coefficient

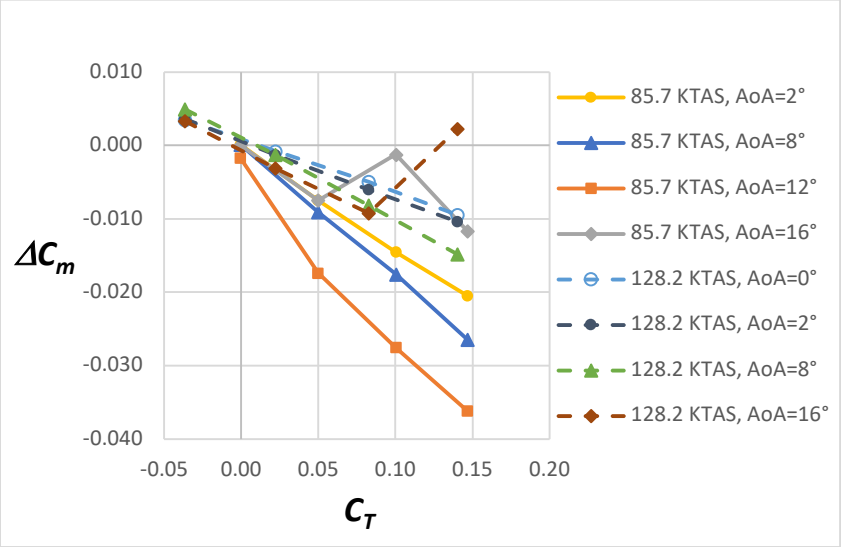

(b) ΔC_m vs C_T

Figure 54. The effect of cruise power on pitching moment for 85.7 KTAS ($M = 0.136$, 2500 feet, 2250 RPM, $J = 0.8$) and for 128.2 KTAS ($M = 0.225$, 8000 feet, 2250 RPM, $J = 1.3$) at angles of attack from $\alpha = 0°$ to $\alpha = 16°$.

3.5 Effect of Cruise Power on Yawing Moment, USM3D

The effects of cruise power on yawing moment coefficient (C_n) and delta yawing moment coefficient (ΔC_n) for two airspeeds, 85.7 KTAS and 128.2 KTAS, and for several angles of attack are shown in Figure 55. Similar to Sections 3.3–3.4, the data reported in this section were semispan yawing moment coefficient. Therefore, the semispan yawing moment was not balanced by the port side and had a very small and slightly positive yawing moment (Figure 55(a)).

The delta computed for semispan yawing moment coefficients between powered and unpowered solutions indicated no effect of cruise power on the yawing moment for $\alpha < 16^\circ$ (Figure 55(b)). The main affect for $\Delta C_n \neq 0$ was flow separation. For $\alpha = 16^\circ$, the positive ΔC_n for $C_T \geq 0.05$ at 85.7 KTAS resulted from flow separation on the wing between the outboard most high-lift nacelle and the wingtip nacelle, that was unbalanced in these semispan solutions and that did not occur for the unpowered cases, see Figure 38. This was also the situation for 128.2 KTAS at $\alpha = 16^\circ$ and $C_T = 0.14$ (230 lbf/prop), see Figure 39.

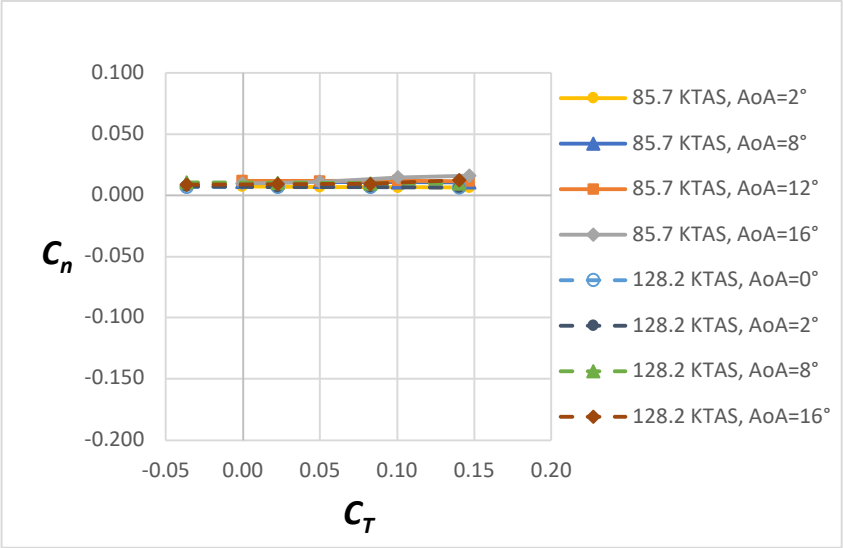

(a) Semispan Yawing Moment Coefficient

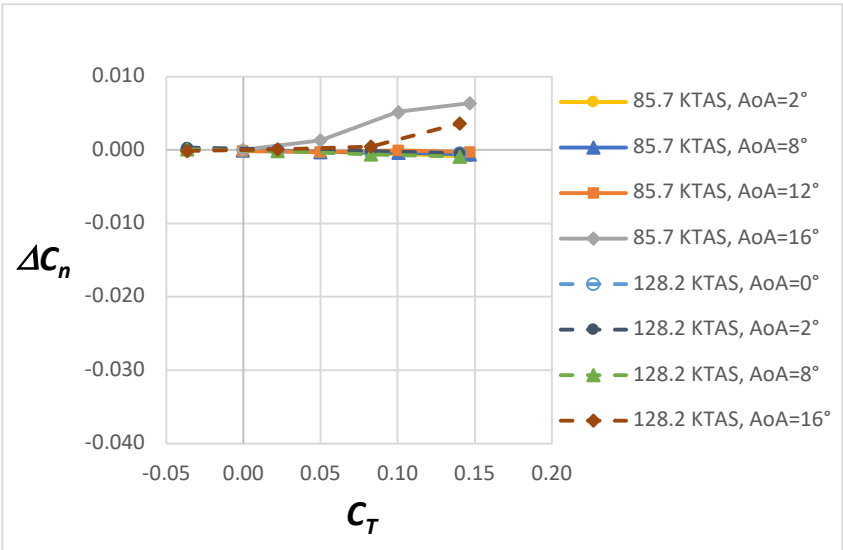

(b) ΔC_n vs C_T

Figure 55. The effect of cruise power on yawing moment for 85.7 KTAS ($M = 0.136$, 2500 feet, 2250 RPM, $J = 0.8$) and for 128.2 KTAS ($M = 0.225$, 8000 feet, 2250 RPM, $J = 1.3$) at angles of attack from $\alpha = 0°$ to $\alpha = 16°$.

3.6 Code Comparisons between USM3D, STAR-CCM+ and LAVA of the Effect of Cruise Power on Delta Rolling Moment (Body-Axis)

The rolling moment coefficients reported in this section were computed in the body-axis system around the x-axis ($C_{m,X}$). The delta rolling moment coefficients ($\Delta C_{m,X}$) predicted by the three codes (USM3D, STAR-CCM+, LAVA) from three NASA centers (Langley, Armstrong, Ames) are shown in Figures 56–69. These data were important for gaining some confidence in the data when little to no experimental data were available for establishing the aerodynamic database of the X-57 Maxwell prior to flight testing.

The three codes compared very well for low angles of attack ($\alpha < 8°$), see Figures 56, 57, 61, 62, and 65–69. There were slight differences in the results for $\alpha = 8°$ (see Figures 58 and 63) and $\alpha = 12°$ (see Figure 59). Potential causes for the differences may include a different fuselage closeout at the wingroot and different turbulence models. The same variants of the SA turbulence model were not available for the three CFD codes and at the time of this work. The Armstrong Flight Research Center (AFRC) used the SA turbulence model with a rotation curvature (RC) correction [36] with STAR-CCM+. The Ames Research Center (ARC) used SA RC QCR with LAVA. The Langley Research Center (LaRC) used SA QCR with USM3D.

The largest differences in delta rolling moment occurred at $\alpha = 16°$ (see Figures 60 and 64). Note that since the USM3D solutions had wingroot flow separation at all unpowered and powered conditions for $\alpha = 16°$ (Figures 38–39), it was appropriate to compute a delta between unpowered and powered conditions to determine the effect of cruise power on rolling moment coefficient. A second note of interest is when the cruise power was on and the propeller was rotated counter to the wingtip vortex, there was additional upwash outboard of the high-lift nacelles that increased the local angle of attack in the region downstream of the cruise propeller.

First, to explain the nonlinear USM3D data at an airspeed of 85.7 KTAS and an altitude of 2500 feet in Figure 60, refer back to Figure 38. With the lowest thrust computed of 96.8 lbf at $C_T = 0.05$, the increased local angle of attack downstream of the propeller resulted in a triangular-shaped flow separation pattern, between the most outboard high-lift nacelle and the wingtip nacelle, that was further forward than the mid chord location in the unpowered case (Figure 38(b)). The added power increased lift (Figure 49) and increased the negative rolling moment (Figure 60), but not as much as negative rolling moment would have increased without the outboard flow separation that appeared at $C_T = 0.05$. The $\Delta C_{m,X}$ at $C_T = 0.05$ and $\alpha = 16°$ was less than the $\Delta C_{m,X}$ values for $\alpha < 16°$ due to the introduction of the outboard flow separation region. With an increased thrust to 194.6 lbf at $C_T = 0.10$, the outboard flow separation moved forward to the wing leading edge (Figure 38(c)), which reduced the lift gained from the thrust and resulted in ΔC_L = -0.02 (Figure 49). Therefore, the delta rolling moment was near $\Delta C_{m,X} = 0.0008$ for $C_T = 0.10$. Finally, with increased thrust to 284.5 lbf for $C_T = 0.15$, the flow separation did not change (Figure 38(d)) but the increased power compared to $C_T = 0.10$ resulted in increased lift (Figure 49) and increased negative $\Delta C_{m,X}$ (Figure 60).

Next to explain the nonlinear USM3D data at an airspeed of 128.2 KTAS and an altitude of 8000 feet in Figure 64, refer back to Figure 39. At 128.2 KTAS, the flow separation outboard of the high-lift nacelles moved to the leading edge only at the highest power setting of $C_T = 0.14$. At $C_T = 0.14$, the effect of the flow separation dominated the effect of the increased power and the negative rolling moment was reduced. The increased local angle of attack downstream of the cruise propeller was most likely reduced due to the increased airspeed of 128.2 KTAS compared to 85.7 KTAS. Therefore, the triangular-shaped flow separation pattern outboard of the high-lift nacelles was not present for $C_T < 0.14$, as it was in the lower thrust levels for an airspeed of 85.7 KTAS.

Finally, to summarize the USM3D results, when the flow separation outboard of the high-lift nacelles occurred or moved inboard, the negative rolling moment was reduced and when power was added and there was no change in flow separation, the negative rolling moment was increased.

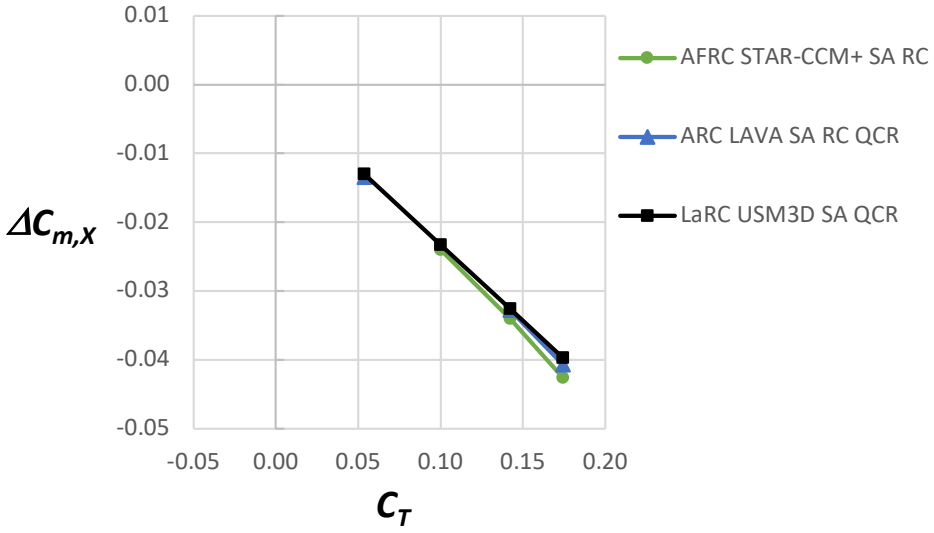

Figure 56. The effect of cruise thrust on delta rolling moment for 64.3 KTAS ($M = 0.1016$) at an altitude of 2500 feet, at $\alpha = 2°$, and with cruise power at 2250 RPM and $J = 0.6$.

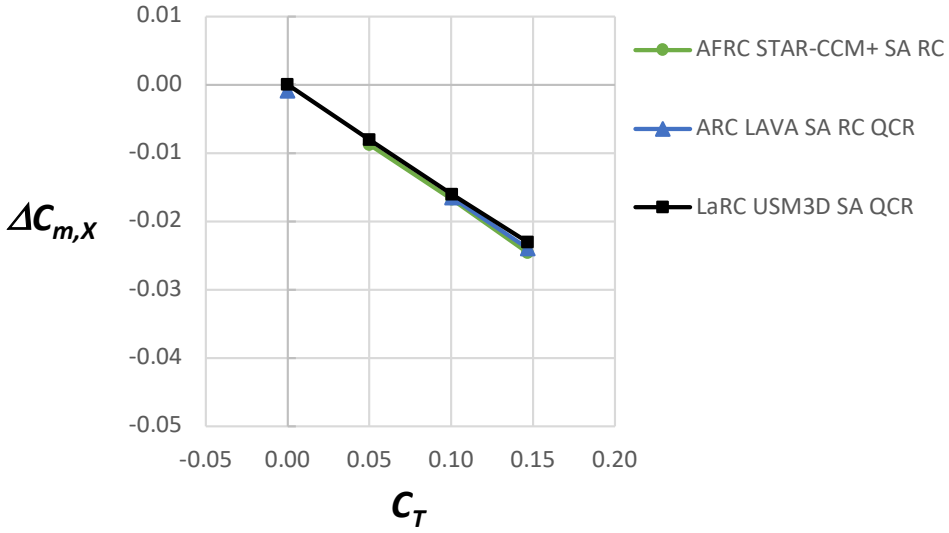

Figure 57. The effect of cruise thrust on delta rolling moment for 85.7 KTAS ($M = 0.1355$) at an altitude of 2500 feet, at $\alpha = 2°$, and with cruise power at 2250 RPM and $J = 0.8$.

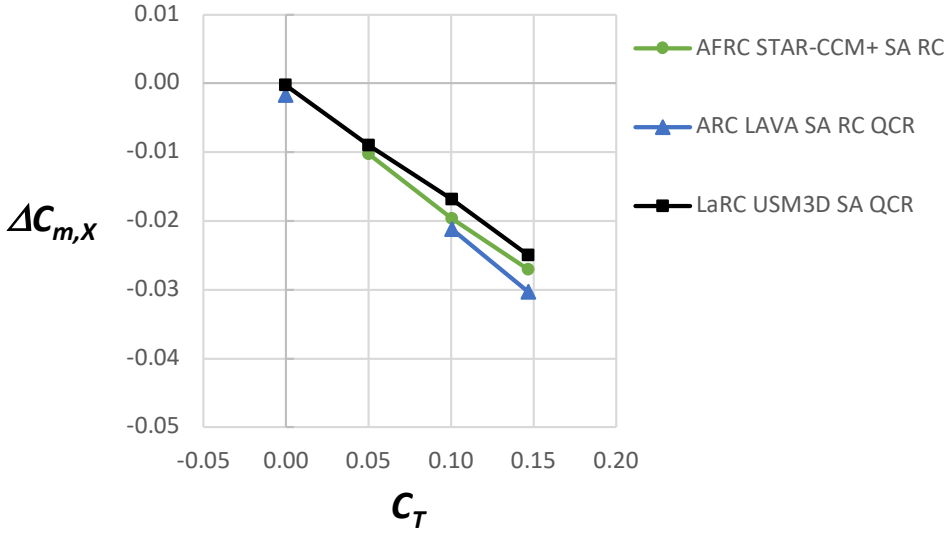

Figure 58. The effect of cruise thrust on delta rolling moment for 85.7 KTAS ($M = 0.1355$) at an altitude of 2500 feet, at $\alpha = 8°$, and with cruise power at 2250 RPM and $J = 0.8$.

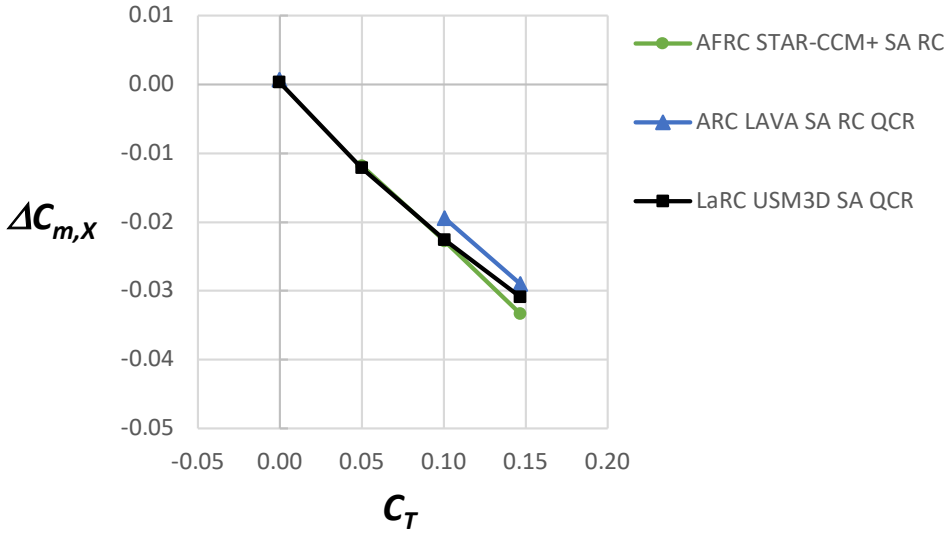

Figure 59. The effect of cruise thrust on delta rolling moment for 85.7 KTAS ($M = 0.1355$) at an altitude of 2500 feet, at $\alpha = 12°$, and with cruise power at 2250 RPM and $J = 0.8$.

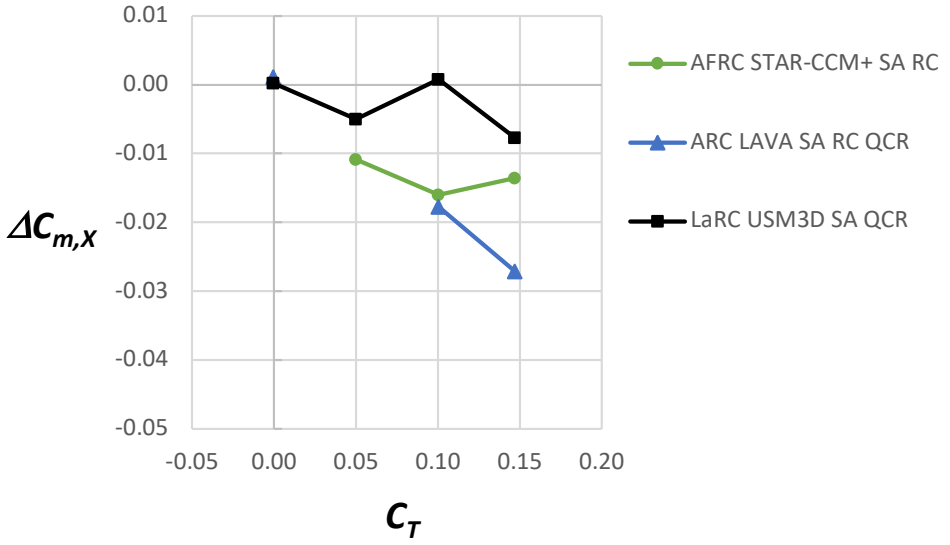

Figure 60. The effect of cruise thrust on delta rolling moment for 85.7 KTAS ($M = 0.1355$) at an altitude of 2500 feet, at $\alpha = 16°$, and with cruise power at 2250 RPM and $J = 0.8$.

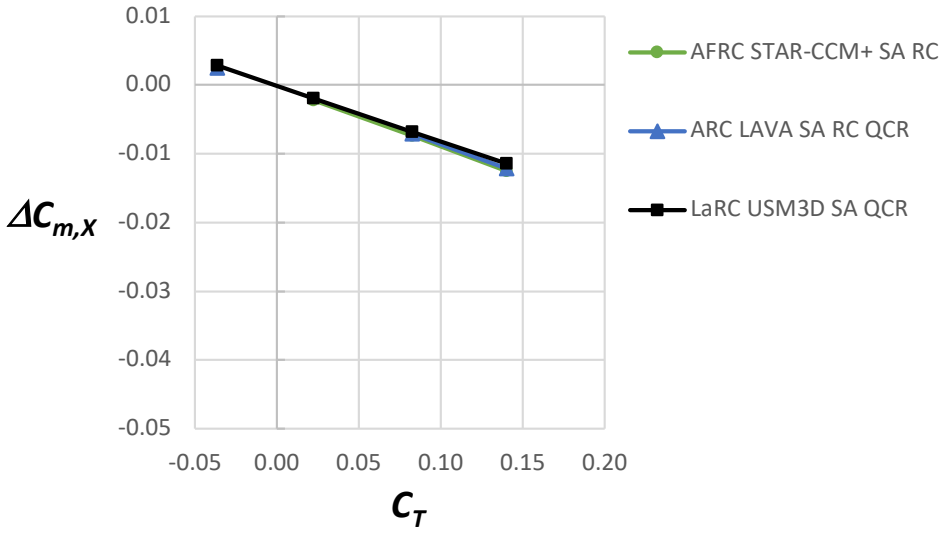

Figure 61. The effect of cruise thrust on delta rolling moment for 128.2 KTAS ($M = 0.2246$) at an altitude of 8000 feet, at $\alpha = 0°$, and with cruise power at 2250 RPM and $J = 1.3$.

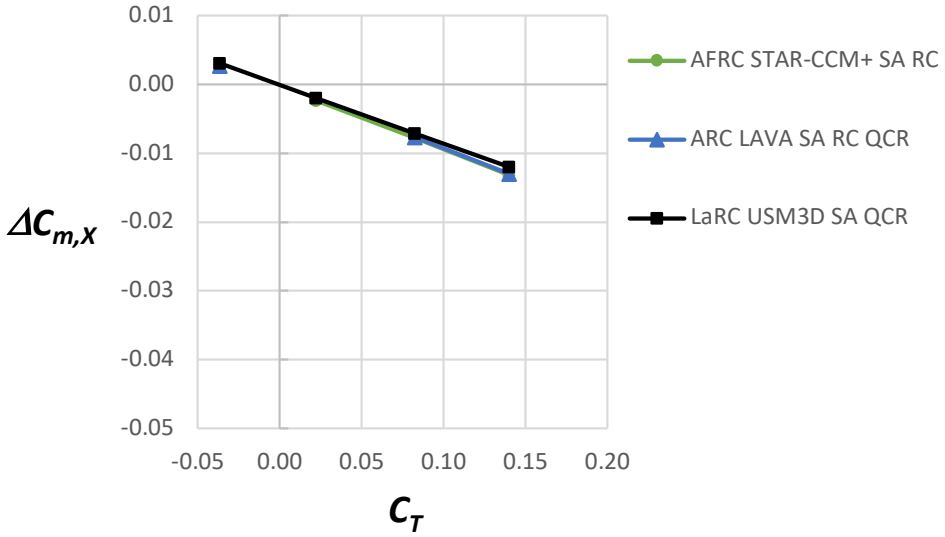

Figure 62. The effect of cruise thrust on delta rolling moment for 128.2 KTAS ($M = 0.2246$) at an altitude of 8000 feet, at $\alpha = 2°$, and with cruise power at 2250 RPM and $J = 1.3$.

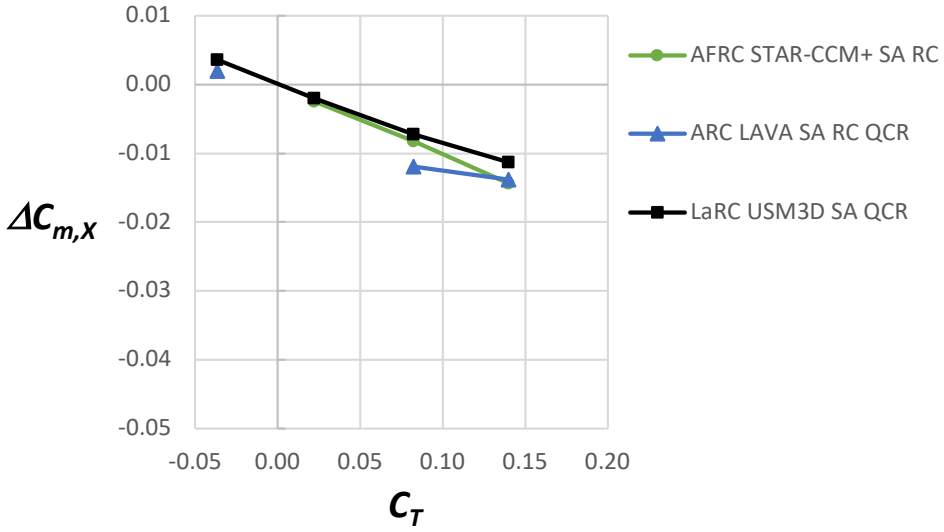

Figure 63. The effect of cruise thrust on delta rolling moment for 128.2 KTAS ($M = 0.2246$) at an altitude of 8000 feet, at $\alpha = 8°$, and with cruise power at 2250 RPM and $J = 1.3$.

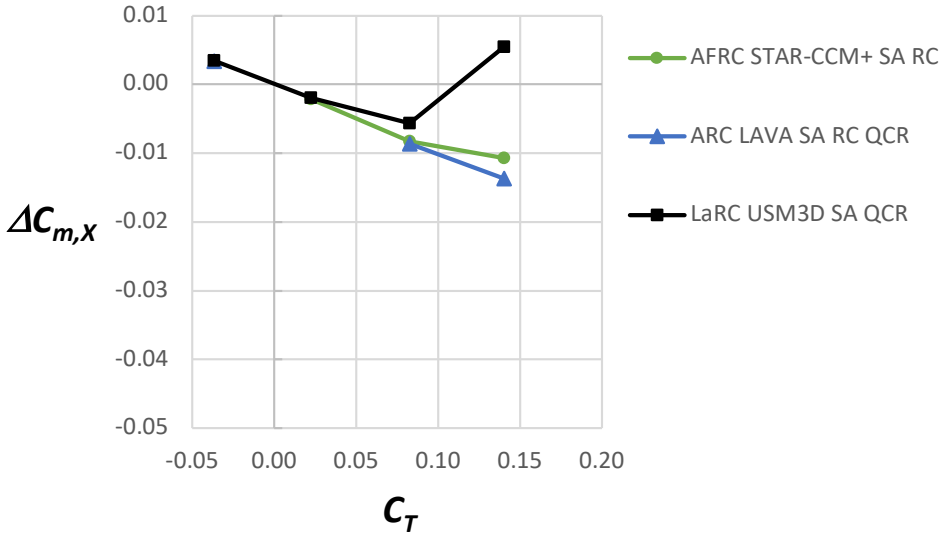

Figure 64. The effect of cruise thrust on delta rolling moment for 128.2 KTAS ($M = 0.2246$) at an altitude of 8000 feet, at $\alpha = 16°$, and with cruise power at 2250 RPM and $J = 1.3$.

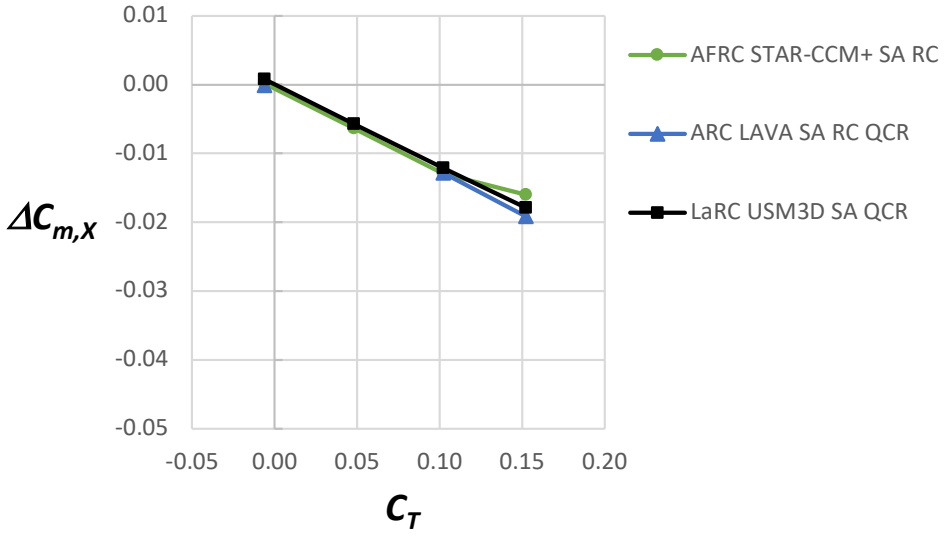

Figure 65. The effect of cruise thrust on delta rolling moment for 98.6 KTAS ($M = 0.1731$) at an altitude of 8000 feet, at $\alpha = 2°$, and with cruise power at 2250 RPM and $J = 1.0$.

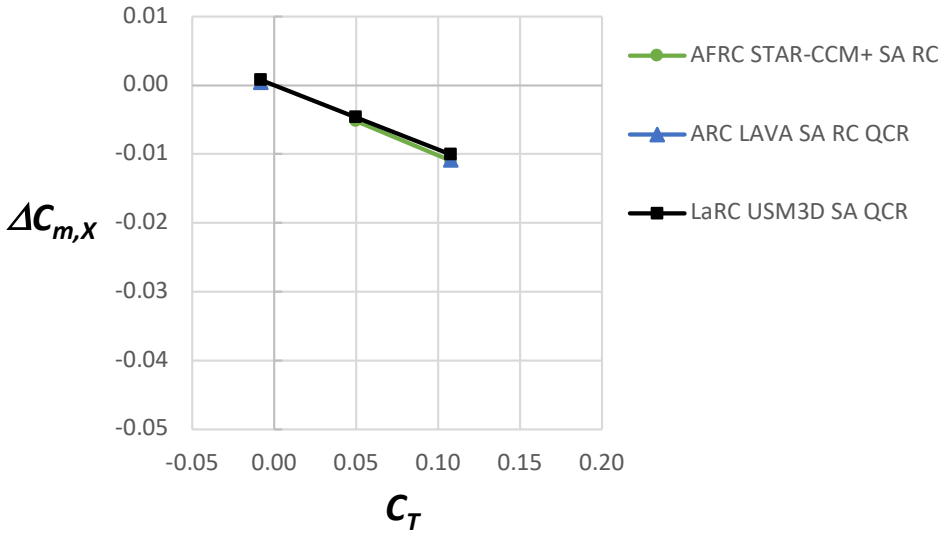

Figure 66. The effect of cruise thrust on delta rolling moment for 118.4 KTAS ($M = 0.2078$) at an altitude of 8000 feet, at $\alpha = 2°$, and with cruise power at 2250 RPM and $J = 1.2$.

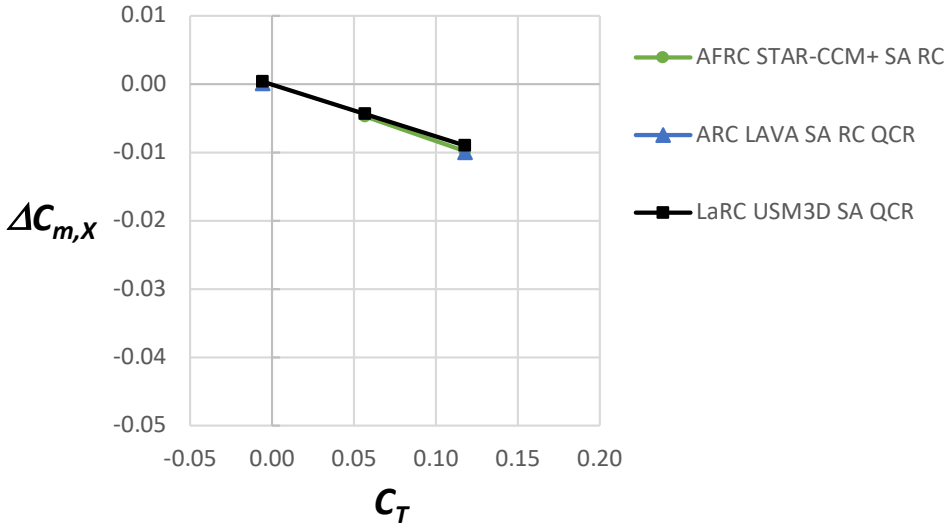

Figure 67. The effect of cruise thrust on delta rolling moment for 123.8 KTAS ($M = 0.2493$) at an altitude of 15000 feet, at $\alpha = 2°$, and with cruise power at 2250 RPM and $J = 1.4$.

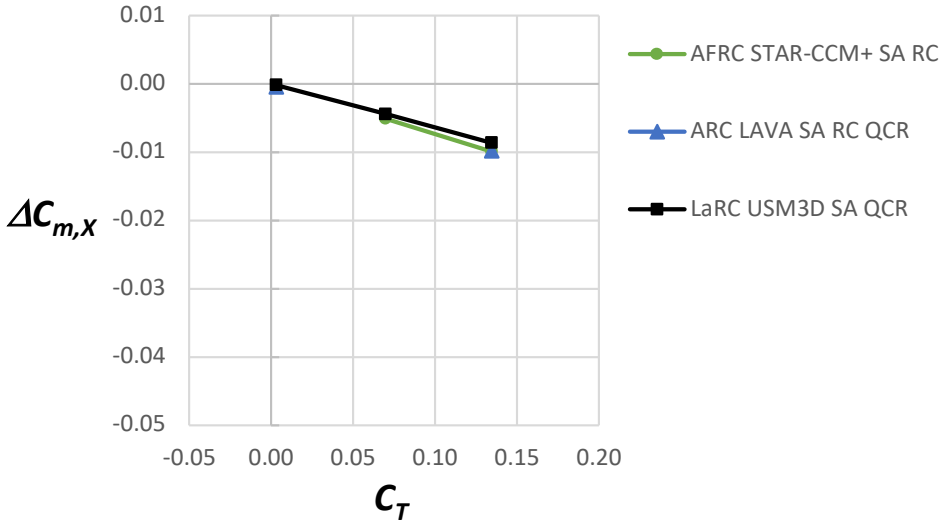

Figure 68. The effect of cruise thrust on delta rolling moment for 125.8 KTAS ($M = 0.2533$) at an altitude of 15000 feet, at $\alpha = 2°$, and with cruise power at 2000 RPM and $J = 1.6$.

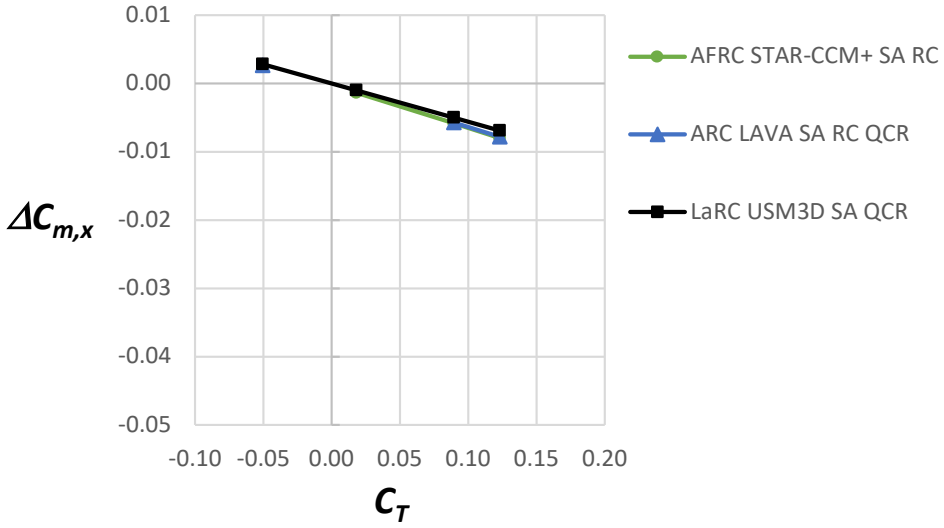

Figure 69. The effect of cruise thrust on delta rolling moment for 141.6 KTAS ($M = 0.2851$) at an altitude of 15000 feet, at $\alpha = 2°$, and with cruise power at 2000 RPM and $J = 1.8$.

4 Conclusions

The X-57 Maxwell was an all-electric airplane with a distributed electric propulsion system used for a high-lift system at takeoff and landing conditions. The focus of this paper was investigating the effects of cruise power on aerodynamic force and moment coefficients, as determined by comparing the cruise configuration with the wingtip propellers operating with the fully unpowered configuration. The computational fluid dynamics flow solver, USM3D, was used to investigate the performance of the X-57 Maxwell at flight Reynolds numbers from 1.4 million to 2.8 million, based on mean aerodynamic chord. Numerical solutions were computed at 2° angle of attack for Mach numbers from 0.1 to 0.3 (64.3 KTAS to 141.6 KTAS), at altitudes of 2500 feet, 8000 feet, and 15000 feet, and cruise power at 1150 RPM, 2000 RPM, and 2250 RPM, and no high-lift blowing. Data were also computed at angles of attack of 8°, 12°, and 16° for a Mach number of 0.1355 (85.7 KTAS), at an altitude of 2500 feet for no high-lift blowing and cruise power at 2250 RPM. An actuator disk was used to model the cruise propellers. This paper does not include results for the high-lift blown wing with the DEP system operational.

The X-57 Maxwell airplane had an increase in induced drag from decreasing the wing span and increased weight from the batteries, compared to the baseline airplane. The motivation for rotating the X-57 Maxwell wingtip propellers in a direction opposite to that of the wingtip vortex was to reduce the penalty of induced drag. The results did show a reduction in drag compared to unpowered, when operating the cruise propellers for angles of attack less than 16°. The drag reduction increased with increasing thrust. The drag reduction was greater at the lower airspeed (85.7 KTAS) with a 70 to 80 drag count reduction at $C_T = 0.15$, than the 40 drag count reduction at 128.2 KTAS for $C_T = 0.14$. For angles of attack less than 16°, the variation in drag reduction with angle of attack, at a given thrust level was less than 10 drag counts at 85.7 KTAS, and less than 4 drag counts at 128.2 KTAS.

The cruise power increased lift for all $\alpha < 16°$. There was a maximum increase in lift coefficient of $\Delta C_L = 0.157$ due to cruise power at 85.7 KTAS and an angle of attack of 12°, and an increase in lift coefficient of $\Delta C_L = 0.123$ for angles of attack of 2° and 8°. At 128.2 KTAS, the maximum increase in lift coefficient was $\Delta C_L = 0.055$ for all angles of attack less than 16°. The wingtip cruise power added an increment to lift by increasing the velocity above the wing in the region downstream of the propeller plane, which reduced the pressure on the upper surface of the wing between the outboard nacelle and the wingtip nacelle. The sectional lift coefficients indicated the increment of additional lift was limited to the wing mostly located downstream of the propeller plane, with slight influence inboard of the propeller tip at the wing leading edge. The increased lift from cruise power was larger at 85.7 KTAS, than at an airspeed of 128.2 KTAS because the ΔV created by the propeller is a larger percentage of the freestream velocity at the lower airspeed. The largest increases in sectional lift coefficient due to power were at $\alpha = 12°$.

The effect of cruise thrust on rolling moment was larger at 85.7 KTAS than at 128.2 KTAS 53(b). The change in rolling moment between powered and unpowered conditions was significantly larger at 85.7 KTAS, than at 128.2 KTAS. These data were important to understand the effect of differential cruise thrust on rolling

moment to add the effects in the X-57 Maxwell flight simulator.

The effect of cruise thrust on pitching moment was a slight increase in nose-down pitching moment coefficient with increasing thrust coefficient for both airspeeds and angles of attack less than 16°. However, the maximum increase in negative pitching moment due to cruise thrust was only ΔC_m = -0.036 at 85.7 KTAS and $\alpha = 12°$.

There was no effect of cruise thrust on yawing moment coefficient for $\alpha < 16°$. At $\alpha = 16°$, the maximum increase in yawing moment was only 0.006 due to flow separation on the wing between the most outboard high-lift nacelle and the wingtip nacelle.

The effect of cruise power on rolling moment predicted from three computational fluid dynamics codes, from three NASA centers, compared very well for low angles of attack of 0° and 2°, and moderately well for angles of attack of 8° and 12°. These data comparisons were important for gaining some confidence in the data when no experimental data were available prior to flight testing.

References

1. Borer, N. K.; Patterson, M. D.; Viken, J. K.; Moore, M. D.; Clarke, S.; Redifer, M. E.; Christie, R. J.; Stoll, A., Dubois, A.; Bevirt, J.; and Gibson, A. R., Foster, T. J.; and Osterkamp, P. G.: Multidimensional Design and Performance of the NASA SCEPTOR Distributed Electric Propulsion Flight Demonstrator. AIAA 2016-3920, June 2016.

2. Patterson, M. D.; Derlaga, J. M.; and Borer, N. K.: High-Lift Propeller System Configuration Selection for NASA's SCEPTOR Distributed Electric Propulsion Flight Demonstrator. 16th AIAA Aviation Technology, Integration, and Operations Conference. AIAA 2016-3922, June 2016.

3. Borer, N. K.; Patterson, M. D.; Derlaga, J. M.; Litherland, B. L.; Deere, K. A.; and Stoll, A.: Flight Performance Maneuver Planning for NASA's X-57 "Maxwell" Flight Demonstrator- Part 1: Power-off Glides. AIAA Aviation 2019 Forum. AIAA 2019-2855, June 2019.

4. Borer, N. K.; Patterson, M. D.; Derlaga, J. M.; Litherland, B. L.; Deere, K. A.; and Stoll, A.: Comparison of Mixed-Order Aero-Propulsive Performance Predictions for Distributed Electric Propulsion Configurations. Invited paper for AIAA Transformational Flight Program Committee. AIAA 2016-3981, June 2016.

5. Borer, N. K.; Derlaga, J. M.; Deere, K. A.; Carter, M. B.; Viken, S. A.; Patterson, M. D.; Litherland, B. L.; and Stoll, A.: Comparison of Aero-Propulsive Performance Predictions for Distributed Electric Propulsion Configurations. Invited paper for AIAA Transformational Flight Program Committee. AIAA 2017-0209, January 2017.

6. Viken, J. K.; Viken, S. A.; Deere, K. A.; and Carter, M. B.; Design of the Cruise and Flap Airfoil for the X-57 Maxwell Distributed Electric Propulsion Aircraft. Aviation Forum 2017, 35th AIAA Applied Aerodynamics Conference, AIAA 2017-3922, June 2017.

7. Deere, K. A.; Viken, J. K.; Viken, S. A.; Carter, M. B.; Wiese, M. R.; and Farr, N. L.: Computational Analysis of a Wing Designed for the X-57 Distributed Electric Propulsion Aircraft. Aviation Forum 2017, 35th AIAA Applied Aerodynamics Conference, AIAA 2017-3923, June 2017.

8. Deere, K. A.; Viken, S. A.; Carter, M. B.; Viken, J. K.; Derlaga, J. M.; and Stoll, A.: Comparison of High-Fidelity Computational Tools for Wing Design of a Distributed Electric Propulsion Aircraft. Aviation Forum 2017, 35th AIAA Applied Aerodynamics Conference, AIAA 2017-3925, June 2017.

9. Deere, K. A.; Viken, S. A.; Carter, M. B.; Viken, J. K.; Wiese, M. R.; and Farr, N. L.: Computational Analysis of Powered Lift Augmentation for the LEAPTech Distributed Electric Propulsion Wing. Aviation Forum 2017, 35th AIAA Applied Aerodynamics Conference, AIAA 2017-3921, June 2017.

10. Deere, K. A.; Viken, J. K.; Viken, S. A.; Carter, M. B.; Cox, D.; Wiese, M. R.; and Farr, N. L.: Computational Component Build-up for the X-57 Distributed Electric Propulsion Aircraft. SciTech AIAA 2018-1275, January 2018.

11. van der Meer, S.; and Veldhuis, L.: Numerical Assessment of Directional Stability and Control with Tip-mounted Propellers. Master's Thesis at the Delft University of Technology, January 24, 2020.

12. Frink, N. T.; Pirzadeh, S. Z.; Parikh, P. C.; Pandya, M. J.; and Bhat, M. K.: The NASA Tetrahedral Unstructured Software System. The Aeronautical Journal, Vol. 104, No. 1040, October 2000, pp. 491–499.

13. Abdol-Hamid, K. S., Frink, N. T., Deere, K. A., and Pandya, M. J.: Propulsion Simulations Using Advanced Turbulence Models with the Unstructured-Grid CFD Tool, TetrUSS. AIAA 2004-0714, January 2004.

14. McDaniel, D. R., and Tuckey, T.R.: HPCMP CREATE-AV Kestrel New Capabilities and Future Directions. AIAA SciTech Forum, AIAA 2019-0840, 7-11 January 2019.

15. Shafer, T. C., Green, B. E., Hallissy, B. P., and Hine, D. H.: Advanced Navy Applications Using CREATE-AV Kestrel. AIAA SciTech Forum, AIAA 2014-0418, 13-17 January 2014.

16. Siemens Digital Industries Software, "Simcenter STAR-CCM+ Software," Costa Mesa, CA, Version 13.04.10, retrieved 30 June 2023. `https://www.plm.automation.siemens.com/global/en/products/simcenter/STAR-CCM.html`

17. Kiris, C. C., Housman, J. A., Barad, M. F., Brehm, C., Sozer, E., and Moini-Yeta, S.; Computational Framework for Launch, Ascent, and Vehicle Aerodynamics (LAVA). Aerospace Science and Technology, Vol. 55, 2016, pp. 189-219.

18. Yoo, S. Y.; Duensing, J. C.; Deere, K. A.; Viken, J. K., and Frederick, M. A.: Computational Analysis on the Effects of High-lift Propellers and Wingtip Cruise Propellers on the X-57 Airplane. AIAA-2023-3382, June 2023.

19. Duensing, J. C.; Yoo, S. Y.; Maldonado, D.; Housman, J. A.; Jensen, J. C.; and Kiris, C. C..: Establishing Best Practices for X-57 Maxwell CFD Database Generation. AIAA-2019-0274, January 2019.

20. Yoo, S., and Duensing, J.: Computational Analysis of the External Aerodynamics of the Unpowered X-57 Mod-III Aircraft. AIAA-2019-3698, June 2019.

21. Deere, K. A.; Viken, J. K.; Viken, S. A.; Carter, M. B.; Cox, D.; Wiese, M. R.; and Farr, N. L.: Computational Analysis of the X-57 Maxwell Airplane at Unpowered Conditions (Preliminary Fuselage). NASA TM-20210011034, April 2022.

22. Deere, K. A.; Viken, J. K.; Wiese, M. R.; and Farr, N. L.: Computational Analysis of the X-57 Maxwell Airplane, the Landing Configuration with

High-Lift Blowing and Aileron Deflections (Preliminary Fuselage). NASA TM-20230010662, January 2024.

23. Spalart, P. R.; and Allmaras, S. R.: A One-Equation Turbulence Model for Aerodynamic Flows. Recherché, No. 1, 1994, pp. 5-21.

24. Spalart, P. R.: Strategies for Turbulence Modeling and Simulation. International Journal of Heat and Fluid Flow, Vol. 21, 2000, pp. 252-263.

25. Menter, F. R.: Two-Equation Eddy-Viscosity Turbulence Models for Engineering Applications. AIAA Journal, vol. 32, no. 8, Aug. 1994, pp. 1598– 1605.

26. Pandya, M. J.; Abdol-Hamid, K. S.; and Parlette, E. B.: CFD Computations for a Generic High-Lift Configuration Using TetrUSS. The 29th AIAA Applied Aerodynamics Conference, AIAA 2011-3008, 27-30 June 2011.

27. Dandois, J.: Improvement of Corner Flow Prediction Using the Quadratic Constitutive Relation. AIJAAJ Volume 52, Number 12, December 2014. https://doi.org/10.2514/1.J052976

28. Goldstein, S.: On the Vortex Theory of Screw Propellers. Proceeding of the Royal Society of London A: Mathematical, Physical and Engineering Sciences, vol. 792, no. 123, Apr. 1929, pp. 440–465.

29. Adkins, C. N.; and Liebeck, R. H.: Design of Optimum Propellers. AIAA Journal of Propulsion and Power, Vol. 10, No. 5, September-October 1994.

30. Hahn, A.: Open Vehicle Sketch Pad Aircraft Modeling Strategies. 51st AIAA Aerospace Sciences Meeting including the New Horizons Forum and Aerospace Exposition. 2013.

31. Belben, J. B.; McDonald, R. A..: Enabling Rapid Conceptual Design Using Geometry-Based Multi-Fidelity Models in VSP. 51st AIAA Aerospace Sciences Meeting, AIAA2013-0328, January 2013.

32. Samareh, J.: GridTool: A Surface Modeling and Grid Generation Tool. Proceedings of the Workshop on Surface Modeling, Grid Generation, and Related Issues in CFD Solutions, NASA CP–3291, May 9–11, 1995.

33. Helden Aerospace Inc.: https://heldenaero.com/heldenmesh/ [retrieved 30 June 2023]

34. Pirzadeh, S.: Unstructured Viscous Grid Generation by Advancing-Layers Method. AIAA Journal, Vol. 32, No. 8, pp. 1735–1737, August 1994.

35. Pirzadeh, S.: Structured Background Grids for Generation of Unstructured Grids by Advancing Front Method. AIAA Journal, Vol. 31, No. 2, pp. 257–265, February 1993.

36. Shur, M. L., Strelets, M. K., Travin, A. K., and Spalart, P. R. 2000. "Turbulence Modeling in Rotating and Curved Channels: Assessing the Spalart-Shur Correction", AIAA Journal, 38(5), pp. 784-792.